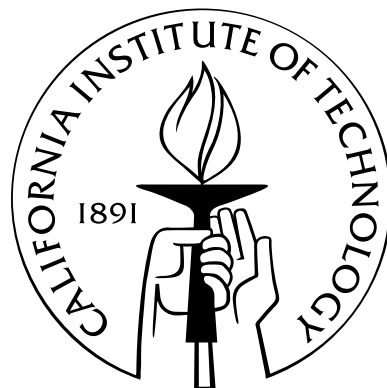


# **Measurement and Control of Individual Quanta in Cavity QED**

Thesis by  
Theresa W. Lynn

In Partial Fulfillment of the Requirements  
for the Degree of  
Doctor of Philosophy



California Institute of Technology  
Pasadena, California

2003  
(Defended May 16, 2003)

© 2003  
Theresa W. Lynn  
All Rights Reserved

Because we know it, we are not an accident:  
chance, redeemed returns to order.  
Tied to the earth and to time,  
a light and weightless ether,  
thought supports the worlds and their weight.

– *Response and Reconciliation*, Octavio Paz

# Acknowledgements

Thanks first and foremost to my advisor, Jeff Kimble, and to the members of the Caltech quantum optics group over my entire time here as a graduate student. The things I have learned from all of you range from plumbing to philosophy, and from the absurd to the truly profound. Jeff's fund of scientific knowledge and his continuing thirst for new understanding never cease to amaze me; his perspective and patience stand out as well in his role as an advisor. I have been privileged to work directly on experiments with Kevin Birnbaum, Joseph Buck, Michael Chapman, Christina Hood, Tracy Northup, and Dominik Schrader; in addition, I would like to thank Andrew Doherty for close collaboration on theoretical issues. Special acknowledgement goes to three close co-workers over the years: Christina Hood, who taught me to be an experimentalist, Jun Ye, who sets an example of dedication and wide-ranging scientific enthusiasm, and Kevin Birnbaum, whose inveterate skepticism is beyond price.

Thanks of another sort to my husband, Jon Moore; I could not have asked for a better partner in the delights and woes of the last seven years. To my parents, thanks for the wonderful two years you gave us, helping to make graduate school and young twins not only compatible but enjoyable. And finally, thanks to the many others who have helped maintain my sanity throughout graduate school, particularly the Chamber Singers in early years, the quartet (now quintet) this past academic year, and the many and varied members of the reading group throughout my time at Caltech.

# Abstract

Cavity quantum electrodynamics (QED) in the strong-coupling regime provides the opportunity to monitor and control the dynamics of a simple quantum system. A single Cesium atom interacts strongly with single-photon fields in the mode of a high-finesse optical cavity. When the resulting coherent coupling rate dominates dissipation in the system, strong coupling is realized and the system displays distinctively quantum behavior. The coupling between atomic internal states and the quantized cavity field allows for diverse protocols in quantum state preparation, quantum communication, and quantum logic. However, the atom's external or motional state must also be taken into account. My research develops cavity QED in the limit where the coherent atom-field coupling dominates the atomic kinetic energy and thus significantly affects the atomic center-of-mass motion. In this regime, the interaction of the atom with the cavity field provides both a means of controlling atomic motion and a signal for detecting that motion in real time with high signal-to-noise. The sensing capability of the “atom-cavity microscope” is exploited to trap single atoms with single-photon fields and to monitor their orbits in real time as they are bound in the cavity. Such real-time position sensing is the basis for a detailed strategy and ongoing experiment to actively stabilize select aspects of an atom’s motion within the cavity. As the cavity-enabled position measurement approaches the standard quantum limit, this work begins to realize a quantum servo for atomic position and to address questions of optimal state estimation and state preparation. In combination with other progress in cavity QED, it furthers the goal of controlled atom-field interactions for quantum information science.

# Contents

<b>Acknowledgements</b>	<b>iv</b>
<b>Abstract</b>	<b>v</b>
<b>1 Introduction and Motivation</b>	<b>1</b>
1.1 Introduction . . . . .	1
1.2 Motivations . . . . .	2
1.3 Introduction to the Cavity QED System . . . . .	3
1.4 History of Us . . . . .	5
1.5 Overview and Outline . . . . .	7
<b>2 Cavity QED and the Road to Strong Coupling</b>	<b>10</b>
2.1 “I Am Quantum. Hear Me Roar.” . . . . .	10
2.2 Quantitative Description of the Atom-Cavity System . . . . .	13
2.2.1 Master Equation in the Presence of Dissipation . . . . .	15
2.3 Semiclassical Approximation: Optical Bistability . . . . .	16
2.4 Interacting Single Quanta: The 1-D Atom . . . . .	18
2.5 Strong Coupling: Vacuum Rabi Splitting, Trapping, and Sensing . . .	19
2.5.1 Real-Time Detection and Trapping with Single Photons . . .	22
2.6 Broader Application of Real-Time Sensing Capabilities . . . . .	24
2.6.1 More Intuitive Arguments for Optical Information and Critical Parameters . . . . .	25
2.6.2 What is the Information Good For? . . . . .	27

<b>3 Experimental Tools and Technical Challenges</b>	<b>29</b>
3.1 Principal Components of the Experiment . . . . .	29
3.2 Magneto-Optical Trap and Sub-Doppler Polarization Gradient Cooling	30
3.3 Probe Beam and Local Oscillator Generation and Stabilization . . . . .	32
3.4 The Physics Cavity . . . . .	34
3.5 Vacuum Chamber . . . . .	35
3.6 Locking of Laser Frequency and Cavity Length . . . . .	38
3.7 Heterodyne Detection and Calibration . . . . .	39
3.8 Data Acquisition . . . . .	43
<b>4 Strong Coupling for Trapping and Sensing: The Atom-Cavity Microscope</b>	<b>44</b>
4.1 Summary of Experimental Results . . . . .	44
4.2 Reconstruction Algorithms and Validation . . . . .	49
4.2.1 Note on Conservative Motion in Gaussian Potentials . . . . .	58
4.3 Position Sensitivity Estimates . . . . .	58
4.4 Why Do Reconstructions Work in <i>This</i> Parameter Regime? . . . . .	61
4.4.1 Quasi-classical Model for Atomic Motion in the Cavity . . . . .	63
4.4.2 Potentials and Heating Rates for Atomic Motion . . . . .	65
<b>5 Active Feedback on Atomic Position: Towards a Quantum Servo</b>	<b>71</b>
5.1 The Atom and Cavity as a Control System: Basic Feedback Strategy	72
5.1.1 General Feedback Strategy . . . . .	74
5.2 Simulations of Feedback Algorithms in Operation . . . . .	76
5.2.1 Actual Dynamics But No Measurement Noise . . . . .	77
5.2.2 Adding Measurement Noise Adds Delays . . . . .	79
5.2.3 Account for Delays by Waiting a Cycle . . . . .	80
5.2.4 Comparisons with Open Loop Strategies . . . . .	82
5.2.5 Performance with Axial Motion Suppressed . . . . .	85
5.3 Outlook for Experimental Implementation . . . . .	86
5.4 Current Limits and Future Directions . . . . .	88

<b>6 Farther Up and Farther In</b>	<b>91</b>
6.1 Vacuum and MOTs . . . . .	93
6.1.1 Chamber Design and Construction . . . . .	93
6.1.2 Cesium Reservoir and Vapor Cell Loading . . . . .	96
6.1.3 Differential Pumping . . . . .	98
6.1.4 Getting Atoms to the Cavity: Upper and Lower MOT's . . . . .	102
6.2 Probe Beam Generation and Locking Scheme . . . . .	105
6.3 New Physics Cavity: Improvements and Difficulties . . . . .	109
6.3.1 Controlling Birefringence . . . . .	110
6.3.2 Specifically Chosen Cavity Length . . . . .	112
6.3.3 The Shear Mode PZT's . . . . .	114
6.3.4 Length Variation with Magnetic Field . . . . .	116
6.4 Into the Digital Era . . . . .	119
<b>7 Fabry-Perot Cavities for Fun and Profit</b>	<b>121</b>
7.1 REO/ATF Mirrors at the Current State of the Art . . . . .	121
7.2 Birefringence Issues . . . . .	122
7.3 What Cavities Are Good for What? . . . . .	131
7.3.1 Basic Cavity Geometry and Mode Structure . . . . .	131
7.3.2 Atoms in the Cavity . . . . .	132
7.3.3 Light in the Cavity . . . . .	134
7.3.4 Usefulness for Cavity QED . . . . .	137
7.4 Signal-to-Noise for Atom Orbits . . . . .	139
7.4.1 Connection to Position Sensitivity in the ACM . . . . .	143
7.5 Measuring Lengths of Very Short Cavities . . . . .	144
<b>8 Outlook and Extensions for Feedback and Short Cavities</b>	<b>146</b>
8.1 Cooling to the Axis by Breaking Cylindrical Symmetry . . . . .	146
8.2 Axial Motion: Sensing and Cooling . . . . .	148
8.3 Far-Flung Applications of Very Short Cavities . . . . .	150
8.4 Comment on Quantum State Estimation and Control . . . . .	151

<b>A Computer-Experiment Interfacing in the Active Feedback Experiment</b>	<b>153</b>
A.1 Overall Experiment Timing . . . . .	153
A.1.1 Framegrabber Operation . . . . .	154
A.2 Data Acquisition . . . . .	155
A.3 Triggering and Feedback . . . . .	155
<b>Bibliography</b>	<b>157</b>

# List of Figures

1.1	Basic rates in the cavity QED system . . . . .	4
2.1	Jaynes-Cummings ladder of atom-cavity eigenstates . . . . .	14
2.2	Semiclassical vs. quantum saturation behavior. . . . .	17
2.3	Vacuum Rabi splitting for $(g_0, \kappa, \gamma_{\perp}) = 2\pi(120, 40, 2.6)$ MHz. . . . .	20
2.4	Schematic experiment with cold atoms in cavity QED. . . . .	21
2.5	Atomic-position-dependent eigenstates and vacuum Rabi splitting for triggered trapping experiments. . . . .	23
3.1	Core of experimental setup: cavity, probe, detection, and MOT . . .	30
3.2	Cesium level structure for cooling, trapping, and cavity QED. . . .	32
3.3	Cavity mirrors, spacing, and field mode depicted to scale. . . . .	36
3.4	Oxidized Cesium on the surface of a mirror removed from a well-used physics cavity. . . . .	38
3.5	Heterodyne operation and factors contributing to detection efficiency. .	40
4.1	Schematic triggered-trapping protocol for the atom-cavity microscope.	45
4.2	Cavity transmission record for a trapped atom moving within the cavity mode. . . . .	46
4.3	Period vs. amplitude of transmission oscillations for trapped atoms. .	48
4.4	Experimental transmission trace and reconstructed trajectory for a trapped atom. . . . .	49
4.5	Principle of 2-D trajectory reconstructions . . . . .	51
4.6	Basic ambiguities of reconstructed trajectories . . . . .	53
4.7	Example trajectory reconstructions from simulated transits. . . . .	55

4.8	Example failed trajectory reconstruction for a linear trajectory. . . . .	56
4.9	Example reconstructions of nearly circular trajectories. . . . .	57
4.10	Sketch of vacuum Rabi splitting as the basis for position sensitivity estimates. . . . .	59
4.11	Effective potentials and heating rates for the ACM parameters. . . . .	66
4.12	Effecive potentials and heating rates in a less conservative parameter regime. . . . .	68
4.13	Heating per motional cycle measures conservative character of the motion.	70
5.1	Block diagram for the atomic position feedback loop, illustrating sources of noise and system nonlinearities. . . . .	74
5.2	General feedback strategy for atomic radial coordinate . . . . .	75
5.3	Simulated feedback example with perfect sensing of $\rho(t)$ . . . . .	78
5.4	Measurement noise leads to filtering and unacceptable loop delay. . . .	80
5.5	Delay is dealt with by tracking $\rho$ turning points and using this information from each cycle to switch the potential at the predicted <i>next</i> turning point. . . . .	81
5.6	Figure of merit for feedback in closed- and open-loop cases (full dynamics).	83
5.7	Feedback performance and lifetime enhancement in simulations with no axial motion. . . . .	87
6.1	Schematic drawings of the differentially pumped vacuum chamber. . .	94
6.2	Actual upper and lower chambers with MOT coils and optics in place.	95
6.3	Cesium reservoir and loading procedure . . . . .	97
6.4	Pressure-ratio and MOT-dropping constraints on differential pumping hole length and diameter. . . . .	100
6.5	Design and mounting of the differential pumping hole. . . . .	101
6.6	Timing diagram for experiment with double MOT. . . . .	103
6.7	Schematic of laser and cavity stabilization . . . . .	106
6.8	Cavity mount piece: detailed design . . . . .	109

7.1	Setup for measurements of cavity birefringence . . . . .	125
7.2	Calculated transmission of off-axis linear input light ( $\theta_{in} = \pi/4$ , or $\frac{1}{\sqrt{2}}(\hat{a} + \hat{b})$ ) through cavity and output linear polarizer for five different values of cavity birefringence . . . . .	128
7.3	Calculated transmission of circular input light ( $\sigma_+$ , or $\frac{1}{\sqrt{2}}(\hat{a} + i\hat{b})$ ) through cavity and output linear polarizer for five different values of cavity birefringence. . . . .	129
7.4	Preservation of input linear or circular polarization through birefringent cavity. . . . .	130
7.5	High reflectivity, low-loss mirrors for cavity QED; side view of cylinder-plus-cone substrate shape. . . . .	132
7.6	Sensitivity for an atom in the cavity as a function of optical information rate (detunings of Table 7.3). . . . .	143

# List of Tables

5.1	Exact conditions used for data of the full-simulation histograms. . . . .	84
6.1	Upper and lower MOT parameters . . . . .	104
6.2	Resonant wavelengths for short physics cavities (T95 mirrors). . . . .	113
7.1	Geometrical properties of cavities as length and mirror curvature are varied. . . . .	134
7.2	Sensitivity for atomic motion in different cavities (detunings chosen for ACM-like trapping). . . . .	141
7.3	Sensitivity for atomic motion in different cavities (detunings compatible with trapping but chosen for sensing). . . . .	142

# Chapter 1

## Introduction and Motivation

### 1.1 Introduction

Detecting and directing the evolution of simple quantum systems is a growing field of study which addresses fundamental aspects of quantum theory as well as emerging technological goals in quantum information science. A handful of physical systems possess the characteristics that allow experiments in this field: coherent interaction between simple quantum systems, comparably weak dissipative couplings to the environment, and accessible input and output channels for control and detection of the dynamics. One such system is cavity quantum electrodynamics, in which a single atom interacts strongly with the quantized field of a high-finesse optical cavity.

The coherent exchange of excitation between atomic dipole and cavity field defines the quantum system under consideration. This system couples to the environment via atomic spontaneous emission and also through the decay of the cavity field. A large part of this cavity decay is associated with transmission of light through the cavity mirrors, which leads to a well-defined output channel where information can in fact be “rescued” through appropriate detection or use of the cavity output light. Likewise, the opportunity to couple light *into* the cavity mode with arbitrary power and frequency provides a convenient input channel for real-time manipulation of the atom-cavity state. When the coherent coupling dominates the decay rates, we have a system in the *strong coupling* regime which has distinctly nonclassical behavior despite its interactions with the environment.

## 1.2 Motivations

Cavity QED in the strong coupling regime offers the possibility for efficient measurement and control of single quanta, and for rapid and controlled coherent interactions between these single quanta. In the language of quantum information theory, cavity QED is one of several viable platforms for quantum logic and quantum communication. Ongoing technical progress brings the field closer to achieving atomic position control that is fine enough and stable enough to perform a series of atom-field logic gates at high fidelity; position control is required for this purpose because it means a precise knowledge of the coherent coupling rate  $g(\vec{r})$ . This ability in turn will allow for on-demand atom-cavity interactions to prepare and coherently couple novel quantum states of the atom and field.

For purposes of quantum information science, atomic physics in optical cavities has the advantage of offering clock rates that are fast in absolute terms, with coherent coupling rates for current experiments in the range  $g_0/2\pi \approx 100 - 200$  MHz. Its chief strength, however, may lie in the marriage of atomic internal states, easily accessible for preparation and robust enough for storage, with states of the light field which can be easily and rapidly transported across large distances. In other words, optical cavity QED provides an attractive setting for the implementation of diverse protocols in quantum communication, quantum teleportation and entanglement distribution, and thus eventually extended quantum networking.

Precise position measurement and control are important to allow high-fidelity quantum gates but also in their own right for what these attempts can teach us about how to measure and steer a quantum system with the handles we are given. Quantum state estimation and control, as well as the implementation of “designer” evolution schemes using active feedback, form an exciting area of quantum information science today.

### 1.3 Introduction to the Cavity QED System

Optical elements in general present boundary conditions that alter the free-space quantization structure of the electromagnetic field. This modified electromagnetic mode structure in turn affects the interactions of an atomic dipole with light, including decay into the now-altered vacuum. Diverse observations have demonstrated changes in atomic radiative processes caused by the presence of a boundary; for example, boundary-induced atomic level shifts form the basis of the Casimir effect and numerous other phenomena [1, 2, 3, 4, 5, 6, 7, 8, 9, 10, 11, 12, 13, 14, 15, 16]. For a review of these effects and their development into the field of cavity QED, see for example Ref. [17].

The boundary conditions imposed by an optical cavity in particular create a set of electromagnetic field modes confined between the cavity mirrors. These resonant cavity modes are well defined in frequency and in spatial structure. The modes of an optical cavity typically subtend a small fraction of  $4\pi$  in solid angle, and thus do not significantly suppress free-space atomic spontaneous emission. However, the presence of the cavity introduces a new rate, the rate of coherent exchange of excitation between atom and cavity field. Through this coherent coupling the atom and cavity decay linewidths do in fact alter one another, at first perturbatively and then strongly as the coherent coupling becomes large relative to both decays. Finally, when the physical size of a cavity is reduced until the cavity mode volume is near the atomic “radiative” volume, a whole new set of quantum dynamics associated with the full quantum susceptibility can be explored within the setting of cavity QED.

Figure 1.1 depicts the components and rates essential for understanding optical cavity QED. A Fabry-Perot resonator is created by aligning two highly reflective spherical mirrors at separation  $l$  measured along the cavity axis. Modes of the cavity possess a standing-wave structure along the axis, so the cavity supports a set of longitudinal modes separated in frequency by a free spectral range (FSR) of  $c/2l$  where  $c$  is the speed of light. (Mirror coatings cause the FSR to deviate very slightly from this simple formula, as discussed in [18] and briefly in Chapters 6 and 7.) At

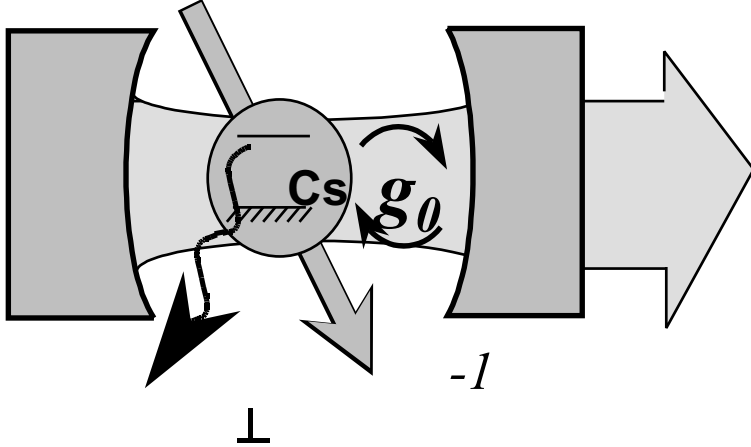


Figure 1.1: Basic rates in the cavity QED system

each longitudinal mode the cavity supports a complete set of transverse modes of different transverse spatial profiles. The  $TEM_{00}$  mode has a cylindrically symmetric Gaussian profile, characterized by a beam waist  $w_0$  for the cavity field.

If the two mirrors are assumed to be identical, the cavity is characterized by the per-mirror power transmission  $T$  and loss  $A$ . The total empty cavity round-trip loss is  $L_{cav} = 2(T + A)$ . The cavity finesse ( $F$ ) is given by

$$F = \frac{2\pi}{L_{cav}} = \frac{\pi}{T + A}. \quad (1.1)$$

The finesse can also be expressed as the ratio of free spectral range to cavity linewidth. It is closely related to another commonly used quantity, the resonator quality factor  $Q$ , which is the ratio of the resonant optical frequency to the cavity decay linewidth. The use of finesse is attractive as it depends only on the mirror properties and not strongly on the cavity dimension. When the cavity length changes, both the FSR and linewidth of the cavity vary as the inverse of the cavity length, and hence the finesse remains a constant.  $Q$  and  $F$  are related by the ratio of the optical frequency to the FSR.

When a single atom is present in the cavity mode volume, the atomic dipole interacts with the electric field built up in the cavity mode to provide a coherent coupling between atom and cavity field. That coherent interaction is characterized

by the rate  $g_0$ , which is one half the Rabi frequency for a ground state atom to couple to a single photon in the cavity field. Other important rates in the system are those which characterize decay. These include the atomic spontaneous emission,  $\gamma_{\perp}$ , and the cavity decay rate  $\kappa$ . To correspond with the use of  $g_0$  for the coherent interaction rate, cavity QED literature typically quotes both atomic and cavity decay in field decay rates, i.e., half the full “power” decay rates. Thus  $\kappa/2\pi = \frac{1}{2} \frac{FSR}{Finesse}$ , and  $\gamma_{\perp} = 1/2\tau_0$  where  $\tau_0$  is the atomic radiative lifetime. A final important quantity is the rate for a single atom to traverse the cavity field and thus to move from zero to optimal coupling. If the relevant motional timescale is given by a transit or orbit time  $\tau$ , then  $1/\tau$  can be considered a third decay rate characterizing the atom-cavity interaction. Strong coupling for both internal and external degrees of freedom is ensured when  $g_0 \gg (\gamma_{\perp}, \kappa, 1/\tau)$ . The cavity QED experiments I have been involved in all take place in this limit, where the atom and cavity jointly form a quantum system open to the environment through decay rates small compared to their coherent exchange of excitation.

## 1.4 History of Us

My involvement in cavity QED research as a student has encompassed three experimental setups for cold-atom cavity QED with very short cavities. When I joined the lab in fall of 1996, Christina Hood and Mike Chapman were just building up the second cold atoms experiment in the group, and the first to use very short ( $l \approx 10 \mu m$ ) cavities. I was privileged to be involved in the completion of that setup and in the experiment which followed. That experiment is presented in Christina Hood’s thesis [19] and in Ref. [20], but I mention here two principal results from that work: first, the demonstration of quantum rather than semiclassical saturation behavior for the atom-cavity system, and second, the mapping out of the vacuum Rabi splitting – measured atom by atom – which clearly demonstrated mechanical effects of the cavity QED probe on single atoms transiting the mode.

At the conclusion of the vacuum Rabi splitting experiment, inspired partially by

the degradation of our physics cavity finesse, Christina and I embarked on a rebuilding of the experiment with an improved cavity. This cavity, which became the heart of the “atom-cavity microscope” experiment, had a finesse of 480,000 as opposed to the 180,000 of the old cavity. At the same time we redesigned the cavity mount to achieve better mechanical stability of the cavity, and thus better length stabilization and quieter transmission measurements during an experiment. With this cavity we implemented a triggered-trapping strategy first proposed some years previously by Scott Parkins and others – namely, the use of strong coupling to trap a single atom with a single-photon-strength field in the cavity [21, 22, 23, 24]. Atomic lifetimes in the cavity were enhanced by a factor of about 4.5 over the free-fall transit time ( $\sim 75 \mu\text{s}$  to cross the mode waist), with some rare events lasting longer than 2 milliseconds. During these transits we were able to resolve transmission oscillations associated with atomic motion toward and away from the cavity axis. These transmission signals provided a real-time measurement of atomic position in the cavity. The explicit position information is one-dimensional, but in fact I was able to use it to reconstruct two-dimensional trajectories by exploiting some knowledge of the effective potentials involved. This experiment and the trajectory reconstruction constituted the “atom-cavity microscope,” as presented in [25].

At the end of this experiment Christina and I spent a fair amount of time understanding the potentials and heating rates in our system, and how they translated to the qualitative character of trapped atom trajectories and our ability to observe them [26]. In this effort we were aided greatly by Andrew Doherty, and also by Kevin Birnbaum who was a brand-new graduate student at the time. Our immediate thoughts on the experimental front were twofold. One, extend our measurement bandwidth and try to see some signatures of axial motion (along the standing-wave direction of the cavity field, i.e., along the cavity axis). Two, use our real-time position tracking to turn on some feedback and actively cool the motion of each trapped atom during its stay in the cavity. Neither naive attempt worked out very nicely, either in my first attempts with Christina or in those I continued with Kevin after her departure. There were good reasons for this, but before we had a chance to become more educated, the

cavity and vacuum system began to exhibit diverse sicknesses.

Once again, then, the experiment was rebuilt, this time more drastically than in the previous cycle. Improvements to the vacuum system, the laser/cavity stabilization scheme, and the data processing system accompanied the replacement of the physics cavity itself. Various technical demons plagued this redesigning effort, such that the experiment is just coming on line at the time of this writing, in April 2003.

Meanwhile, I have investigated the proposed active feedback in experimental conditions and from a more control-theoretic point of view. This work has led to a more carefully reasoned radial feedback algorithm, which has been developed for experimentally realistic conditions and extensively simulated for those same conditions. It has led at the same time to a better understanding of the figure of merit associated with our proposed feedback technique, the limits that apply to it, and directions for future work that should extend our active cooling capability and lead atomic position control to the land of the quantum at long last.

## 1.5 Overview and Outline

In the preceding sections I have begun with some broad comments on cavity QED as a scientific tool and on the motivations for atomic position control in this setting, as well as a summary of my involvement in research furthering this goal. In this final section of Chapter 1, I will outline the structure and contents of the remainder of this thesis.

In Chapter 2, I develop a basic picture of cavity QED both intuitively and quantitatively. My goal in this discussion is to elucidate the important critical parameters for “quantum” behavior in cavity QED and to show how they appear in the formalism, in historical progression to strong coupling, and in intuitive arguments.

Chapter 3 presents an overview of experimental techniques and ongoing technical issues involved in our single-atom, single-photon experiments. While some experimental details are thoroughly dealt with elsewhere [27, 19], the basic techniques are laid out here in enough detail to define the experimental procedure and address some

common points of confusion.

I next move on to results from the atom-cavity microscope experiment in Chapter 4. Again, experimental results and some analysis were provided in [19], but I present a more complete discussion of the reconstruction algorithm for two-dimensional trajectories. The treatment here addresses validation of the algorithm, physical conditions and dynamical regimes that make it possible, and signal-to-noise and sensitivity limits governing the position measurement. Attention is given to benchmarks denoting the degree to which these measurements were truly in a classical regime for the atomic center-of-mass motion.

From the real-time position tracking of Chapter 4 I move on to algorithms for active feedback in Chapter 5. Here I discuss the challenges of active cooling from a control systems point of view, and present simulations building up a viable technique for circularizing atomic motion at a constant distance from the cavity axis. Simulations not only explore highly realistic experimental conditions, but also extend into more hypothetical dynamics in order to clarify the feedback performance and limits more fully.

Chapter 6 describes the feedback experiment currently in progress to implement the strategies derived in Chapter 5. In this chapter the current setup is treated in considerably more detail than the general discussion of Chapter 3. Main new features of this experiment include a new physics cavity, new differentially pumped chamber with a double MOT setup, use of a separate “locking laser” to stabilize the cavity length, and introduction of digital (FPGA) techniques for data acquisition and feedback control.

Chapter 7 is devoted to design and characterization of Fabry-Perot cavities for strong-coupling cavity QED applications. This material is intended both as a technical resource for future design and as a more concrete complement to critical parameter and signal-to-noise considerations developed in Chapters 2 and 4.

Finally, Chapter 8 presents some ideas and calculations for extensions of the active position control work in several directions. I dwell briefly on two or three main avenues for extension: the breaking of cylindrical symmetry to remove atomic angular

momentum, the detection and cooling of axial as well as radial motion, and the separation of trapping and sensing to facilitate long lifetimes and effective feedback. The thesis concludes with these discussions of future prospects.

## Chapter 2

# Cavity QED and the Road to Strong Coupling

### 2.1 “I Am Quantum. Hear Me Roar.”

Crucial to the realization of manifestly quantum effects in cavity QED is *strong coupling*, a condition in which the coherent coupling between atom and cavity field dominates dissipative rates in the system. For a two-level atom optimally coupled to a cavity mode (see Figure 1.1), the dipole-field coupling is given by the Jaynes-Cummings interaction Hamiltonian [28]

$$\hat{H}_{int} = \hbar g_0 (\hat{\sigma}^\dagger \hat{a} + \hat{\sigma} \hat{a}^\dagger), \quad (2.1)$$

where  $(\hat{\sigma}^\dagger, \hat{\sigma})$  are dipole raising and lowering operators,  $(\hat{a}, \hat{a}^\dagger)$  are field annihilation and creation operators for the cavity mode, and  $g_0$  is one half of the single-photon Rabi frequency. This rate describes the exchange of excitation between the atomic dipole  $\vec{\mu}$ , initially in the ground state, and the electric field  $\vec{E}_{1,cav}$  built up by a single photon of frequency  $\omega$  residing in the mode volume  $V_m$  of the optical cavity:

$$\hbar g_0 = \vec{\mu} \cdot \vec{E}_{1,cav} = \mu \sqrt{\frac{\hbar\omega}{2\epsilon_0 V_m}}. \quad (2.2)$$

Thus  $g_0$  is a rate of coherent evolution which must be compared with the dissipative rates for the system. These, in turn, are the atomic spontaneous emission rate  $\gamma_\perp$

and the cavity field decay rate  $\kappa$ . While the regime of  $(\kappa, \gamma_{\perp}) \gg g_0$  is described by classical treatments, we will see that a quantum theory is necessary to account for physics at  $g_0 \gg (\kappa, \gamma_{\perp})$ , in the strong-coupling regime [29, 30, 31].

In a classical description of spectroscopy in an optical cavity, an atomic sample acts as a dispersive medium for the coherent light field circulating in the cavity mode volume. Classical behavior gives way to quantum as single quanta, whether of the atomic sample or of the light field itself, begin to induce nonlinear response in the system. To see how this may be accomplished, we begin with the familiar case of a “bulk” sample and consider how a strong interaction can be preserved as the number of particles is scaled down towards unity. This intuitive discussion is complemented by a more quantitative development in the following sections.

Consider first the interaction of light with a “bulk” atomic sample placed inside the cavity mode. The atoms in the sample scatter the optical field, producing a wavelength-dependent refractive index in the cavity mode volume. The atomic sample affects the resonance properties of the optical cavity if the atom-field interaction strength and the number of atoms are sufficient to noticeably alter the free-space dispersion relation for the light. Thus, if a single atom placed within the mode volume is to act as a nonlinear medium, it must have a large effective cross section for scattering intracavity light. First, then, the atom should have a near-resonant dipole interaction with the optical field mode supported by the cavity. Second, scattering should be enhanced by ensuring that optical wavefronts have every opportunity to interact with the atom in the process of being transmitted through the cavity. This second requirement is accomplished by constructing cavities with high finesse and tightly confined modes, so that light traverses the distance between the mirrors many times before exiting the cavity and furthermore has a high chance of interacting with the atomic cross section on each pass. Tight mode confinement has the additional benefit that the light is thoroughly diffractively mixed and thus the interaction is truly with a single cavity mode that is well defined throughout the interaction process. Quantitatively, the importance of a single atom for the response of the intracavity field is described by the single-atom cooperativity parameter  $C_1 = g_0^2 / 2\gamma_{\perp}\kappa$ , or by its

inverse, the critical atom number,  $N_0 = 2\gamma_{\perp}\kappa/g_0^2$  [31]. The single-atom cooperativity can be re-expressed in terms of familiar properties of the cavity (mode waist  $w_0$  and finesse  $F$ ) and the atomic transition (wavelength  $\lambda$ ). One finds it scales simply as  $C_1 \sim \frac{2F}{\pi} \frac{\lambda^2}{w_0^2}$ , reflecting the requirements outlined above. Note that  $C_1$  does not scale explicitly with the length of a Fabry-Perot cavity.

On the other side of the coin, consider the circumstances necessary to make the quantized nature of the light field relevant to observations of the cavity system. In the classical regime the cavity mode volume is occupied by a large-amplitude coherent field. To fully probe the atomic response function, the electric field associated with the light must be strong enough to saturate the atomic dipole. How, then, is a single photon to accomplish this saturation? Simply put, the photon must be confined to a small volume so its electric field strength within that volume becomes large. Indeed, making use of the single-photon Rabi frequency  $g_0$ , we can define a saturation photon number  $m_0 = \gamma_{\perp}^2/2g_0^2$  [31]. As promised, this quantity is inversely proportional to the cavity mode volume through the factor  $1/g_0^2$ ; it is, however, completely independent of the cavity finesse.

The physical significance of these critical parameters will be revisited in later sections. For now, we simply observe that if single quanta are to leave their stamp on observations in an optical cavity, the critical atom number and/or saturation photon number must satisfy  $(N_0, m_0) \lesssim 1$ . Note that these requirements imply  $g_0 > \gamma_{\perp}$  but not necessarily  $g_0 > \kappa$  as well. Thus manifestly quantum effects in cavity QED span a range of parameter regimes of which true strong coupling is only the most extreme. The transition from weak to strong coupling carries us from a classical description of light fields and scatterers to a regime in which the atom and cavity field must be considered as a single entity bound by a shared quantum of excitation.

## 2.2 Quantitative Description of the Atom-Cavity System

As is often the case, the conceptually and computationally simplest starting point for describing the atom-cavity system is the purely quantum limit, where the atom and cavity evolve via their coherent coupling in the absence of dissipation. This system simply obeys the Schrödinger equation with the Jaynes-Cummings Hamiltonian [28],

$$H_{JC} = \hbar\omega\hat{a}^\dagger\hat{a} + \hbar\omega\hat{\sigma}^\dagger\hat{\sigma} + \hbar g_0(\hat{a}\hat{\sigma}^\dagger + \hat{a}^\dagger\hat{\sigma}). \quad (2.3)$$

Here we consider a two-level atom and  $\omega$  is the common resonance frequency of both atom and cavity. Diagonalizing this Hamiltonian gives rise to the well-known Jaynes-Cummings ladder of eigenstates for the coupled atom-cavity system, as illustrated in Figure 2.1. The coupled eigenstates are characterized by the equal sharing of excitation between the atomic dipole and cavity field, so that the  $n$ -excitation bare states  $|g, n\rangle$  and  $|e, n-1\rangle$  of energy  $n\hbar\omega$  are replaced by

$$|\pm_n\rangle = \frac{1}{\sqrt{2}}(|g, n\rangle \pm |e, n-1\rangle) \quad (2.4)$$

with corresponding energy eigenvalues

$$E_{\pm_n} = n\hbar\omega \pm \sqrt{n}\hbar g_0. \quad (2.5)$$

To quantitatively predict actual atom-cavity dynamics, a treatment that moves beyond this idealized picture to include dissipation and driving terms will be necessary. Two qualitative features, however, are worth noting immediately from the Jaynes-Cummings ladder itself.

First, in the most fully quantum regime, the atom and cavity field are best described in a symmetric treatment where they combine to create a single entity sharing excitation equally. Most notably, for  $n \geq 1$  excitation, there exist strong-field-seeking states  $| -_n \rangle$  that can be thought of as atom-cavity states bound together by the shar-

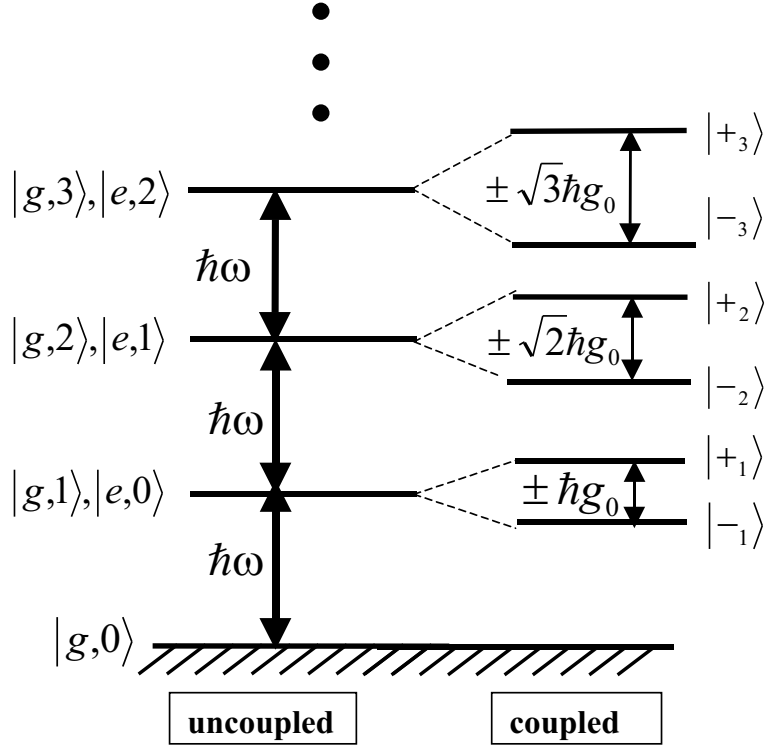


Figure 2.1: Jaynes-Cummings ladder of atom-cavity eigenstates

ing of a quantum of excitation. If we permit a detuning  $\Delta_{ca}$  between the cavity and atom resonance frequencies, the sharing of excitation in these “bound states” becomes asymmetric but the qualitative properties of the ladder remain unchanged.

Second, while a ladder of strong-field- and weak-field-seeking states recalls the dressed states of atomic interaction with a coherent light field (e.g., in free space) [32], the Jaynes-Cummings ladder reflects atomic coupling to a small number of quantized excitations in the cavity mode rather than to a strong classical field in free space. The dressed state splitting at each level of the ladder is proportional to  $\sqrt{n}$ . In the limit of large  $n$ , many photons in the field, the ratio of splittings in successive levels is  $\frac{\sqrt{n+1}}{\sqrt{n}} \rightarrow 1$ ; in this way we recover the free-space, classical-field ladder in which dressed states at each rung are split by a constant  $\pm\hbar\Omega$ .

In the cavity, on the other hand, where just a few excitations create a large response, the anharmonic nature of the level splittings with increasing  $n$  is a feature arising explicitly from the quantized nature of the cavity field. Thus, to observe effects of field quantization on the spectrum of atom-cavity response, we can expect

that experiments must probe the saturation behavior of the system and not simply rely on spectroscopy in the weak-driving limit of  $n < 1$  system excitations. One caveat to this observation, however, is that nonclassical aspects of the system *dynamics* can in fact be observed for weak driving; for example, photon statistics of the cavity output field in time are of interest even for experiments in the weak-excitation limit.

### 2.2.1 Master Equation in the Presence of Dissipation

In the presence of dissipation and driving, and allowing for detuning between the probe field and the atom and cavity resonant frequencies, the Jaynes-Cummings Hamiltonian becomes part of a master equation (see, e.g., [32, 33, 34]) for the joint atom-cavity density operator  $\rho$ . We consider a driving (and probing) field  $\epsilon$  of frequency  $\omega_p$ , a cavity resonant at  $\omega_c = \omega_p + \Delta_{cp}$ , and an atomic resonance frequency  $\omega_a = \omega_p + \Delta_{ap}$ . In the electric dipole and rotating-wave approximations, and in the interaction picture with respect to the probe frequency, the evolution is described by

$$\dot{\rho} = -\frac{i}{\hbar}[\hat{H}_0, \rho] + \gamma_\perp(2\hat{\sigma}\rho\hat{\sigma}^\dagger - \hat{\sigma}^\dagger\hat{\sigma}\rho - \rho\hat{\sigma}^\dagger\hat{\sigma}) + \kappa(2\hat{a}\rho\hat{a}^\dagger - \hat{a}^\dagger\hat{a}\rho - \rho\hat{a}^\dagger\hat{a}), \quad (2.6)$$

$$\hat{H}_0 = \hbar\Delta_{cp}\hat{a}^\dagger\hat{a} + \hbar\Delta_{ap}\hat{\sigma}^\dagger\hat{\sigma} + \hbar g(\vec{r})[\hat{a}\hat{\sigma}^\dagger + \hat{a}^\dagger\hat{\sigma}] + \hbar\epsilon(\hat{a} + \hat{a}^\dagger). \quad (2.7)$$

Here  $g(\vec{r})$  is the coupling strength which takes into account the atomic position  $\vec{r}$  within the cavity mode. For a Fabry-Perot cavity supporting a standing wave mode with Gaussian transverse profile,  $g(\vec{r}) = g_0\psi(\vec{r}) = g_0\cos(2\pi x/\lambda)\exp[-(y^2 + z^2)/w_0^2]$ . The cylindrical symmetry of  $\psi(\vec{r})$  suggests the use of cylindrical coordinates  $(\rho, \theta, x)$ , in which case we write  $g(\vec{r}) = g_0\cos(2\pi x/\lambda)\exp[-\rho^2/w_0^2]$ . In the fully quantum treatment, the atomic position  $\vec{r}$  is itself an operator; in experiments to date a quasi-classical treatment suffices, so the atom may be considered a wavepacket with  $\vec{r}$  a classical center-of-mass position variable.

This master equation provides a valid description of the atom-cavity system in any range of parameters  $(g_0, \kappa, \gamma_\perp)$ . It can in general be solved only numerically, but certain limits, either of inherent rates or of driving strengths, permit analytical

treatments of limited application. In the sections below, we discuss behavior exhibited by theory and experiment in several different parameter regimes from semiclassical to very strongly coupled.

## 2.3 Semiclassical Approximation: Optical Bistability

Certain parameter regimes are well described by an approximation in which we derive from Equations 2.6-2.7 the equations of motion for the expectation values of atom and cavity properties, i.e.,  $\langle \hat{a} \rangle$  and  $\langle \hat{\sigma} \rangle$ ; then within these equations of motion all joint atom-cavity operator moments are assumed to factor, e.g.,  $\langle \hat{a}^\dagger \hat{\sigma} \rangle = \langle \hat{a}^\dagger \rangle \langle \hat{\sigma} \rangle$ . This corresponds to a semiclassical treatment in which the field is described by its coherent amplitude  $\langle \hat{a} \rangle = \alpha$ . Such a replacement is valid in the limit of large critical parameters  $(N_0, m_0) \gg 1$ , in which case a collection of atoms acts as a classical nonlinear intracavity medium. Within this approximation, Equations 2.6-2.7 yield an analytic expression for the driving field  $\epsilon = \kappa\sqrt{m_0}Y$  as a function of the intracavity field  $\langle \hat{a} \rangle \leftrightarrow \sqrt{m_0}X$ . This relation is the well known optical bistability state equation [35]:

$$Y = X \left[ \left( 1 + \frac{2C}{1 + \delta^2 + X^2} \right) + i \left( \phi - \frac{2C\delta}{1 + \delta^2 + X^2} \right) \right]. \quad (2.8)$$

Here we have employed the standard notation for the bistability equation, related to our previous discussions by detunings  $\delta = \Delta_{ap}/\gamma_\perp$  and  $\phi = \Delta_{cp}/\kappa$ , and N-atom cooperativity parameter  $C = NC_1$ .

The system saturation behavior described by this relation is shown in the dotted curve of Figure 2.2. The figure plots  $T$ , the ratio of full-cavity to empty-cavity transmission, as a function of input driving strength expressed in units of the steady-state photon number  $\bar{n}_0$  in the empty cavity. The calculation shown is actually for a system in the strong-coupling regime, namely the cavity of Ref. [20], with  $\omega_a = \omega_c$  and  $\omega_p$  detuned 20 MHz below resonance. Here the bistability prediction is at variance with the quantum prediction and with actual system behavior, as discussed later in

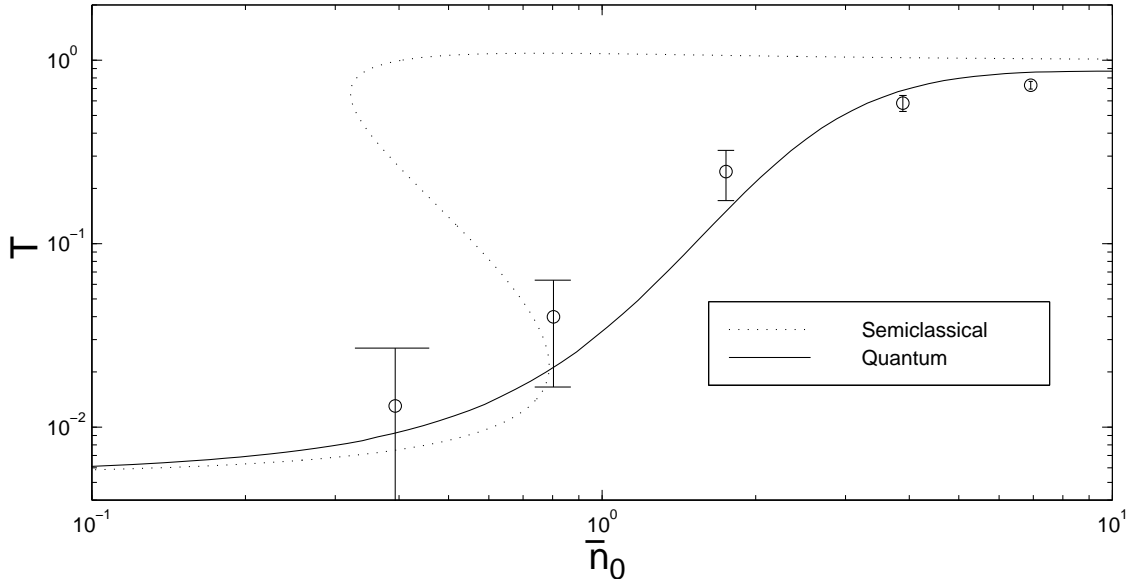


Figure 2.2: Semiclassical and quantum saturation predictions for parameters  $(g_0, \kappa, \gamma_{\perp})/2\pi = (120, 40, 2.6)$  MHz and  $(\omega_a = \omega_c = \omega_p + 2\pi(20$  MHz)).  $T$ , the ratio of full-cavity to empty-cavity transmission, is plotted as a function of input driving strength  $\bar{n}_0$  (in units of empty-cavity photon number). Experimental data is shown as circles with error bars.

this chapter. In the optical bistability state equation the correspondence between the semiclassical amplitude  $X$  and the actual operator expectation value  $\langle \hat{a} \rangle$  is only approximate; in general the intracavity state is not an exact coherent state, but the bistability equation gives an input-output relation between the driving power  $\sim Y^2$  and a transmitted photocurrent  $\sim X^2$  which is valid insofar as the underlying approximation is justified.

Optical bistability effects in general have a long history in measurements within the context of laser physics. Specific cavity QED experiments measuring optical bistability in two-level systems date from the early 1980's [36, 37] and are realizable in relatively low-finesse cavities interacting with a sample of atoms crossing the cavity mode in a thermal atomic beam. However, the bistability state equation is also valid when  $(N_0, m_0) < 1$  in the special case of very weak driving,  $n \ll 1$  excitations in the system. In this case, only the first ( $n = 1$ ) excited states of the system must be considered, and the resulting relationship of joint operator moments makes factoring

formally valid. The correspondence is reflected in the coincidence of the quantum and semiclassical curves of Figure 2.2 at very low driving strength. This fact comes as no surprise in the light of our earlier discussion of the Jaynes-Cummings ladder; the structure of the spectrum reflects the quantized field only for higher drive strengths that sample the anharmonicity of the system eigenvalues. Optical bistability also describes the steady-state behavior of an atom-cavity system where inherent strong coupling is washed out by the simultaneous interaction of many atoms with the cavity mode.

Even in the regime of the optical bistability equation, nonclassical dynamics of the atom-cavity system are accessible. Experiments measuring the photon statistics of the cavity output field have demonstrated nonclassical correlation functions of the output light, with similar work pushing from this limit to the inherently strong-coupling regime [38, 39, 40, 41].

## 2.4 Interacting Single Quanta: The 1-D Atom

By increasing cavity finesse and decreasing mode volume, we move to a regime of small critical parameters  $(N_0, m_0) < 1$ . Here single atoms and photons induce nonlinear effects in the system response. However, this condition is still consistent with overall dissipative dynamics if the cavity decay rate is fast relative to the coherent coupling  $g_0$ . This regime, known as the “bad cavity” limit, is realized for  $\kappa > g_0^2/\kappa > \gamma_{\perp}$ . In this limit, single quanta within the cavity mode interact strongly with one another, but coherence and information leak rapidly from the system into the output channel defined by cavity decay. Thus the atom-cavity coupling is essentially perturbative, and the atom and cavity each retain their distinct identities but with decay rates modified by the interaction. For instance, an atomic excitation, rather than decaying via spontaneous emission at rate  $\gamma_{\perp}$ , is much more likely to be exchanged into the cavity field and subsequently decay via the cavity; this preferential decay via the cavity mode at rate  $g_0^2/\kappa$  gives an effectively “1-D atom.”

Experiments in this parameter regime include the quantum phase gate [42] and the

use of squeezed light in cavity QED [43]. Both of these effects involve the production of nonclassical effects on the light field due to nonlinearities mediated by a “1-D atom” phenomenon. Thus single photons can interact with one another by means of their common coupling to an intracavity atom. These effects are seen with single strongly-coupled atoms; since these experiments delivered atoms to the cavity via thermal beams of atoms transiting a cavity mode, a background of weakly coupled or “spectator” atoms acted to dilute the inherent single-atom effect. Nevertheless, the essential character of the effects was accessible with strongly-coupled atoms flying across the cavity mode quickly against a background of spectators in the wings of the cavity mode.

## 2.5 Strong Coupling: Vacuum Rabi Splitting, Trapping, and Sensing

By further increasing cavity finesse, we arrive at the regime of strong coupling for the atom-cavity system. In this regime, where  $g_0 \gg (\kappa, \gamma_{\perp})$ , single quanta are significant and, furthermore, their coherent interaction dominates other rates in the system. It is in this limit that observations most closely reflect the ideal structure of the Jaynes-Cummings ladder. Exchange of excitation at rate  $g_0$  is no longer perturbative, and the system crosses over to a set of joint atom-cavity eigenstates with widths set by decay rates  $\kappa$  and  $\gamma_{\perp}$ . The coupled atom-cavity transmission spectrum reflects this eigenvalue structure via the vacuum Rabi splitting [44], in which the empty-cavity Lorentzian line profile is transformed into a double-peaked transmission function as shown in Figure 2.3 and first directly observed in [45]. The positions and widths of the vacuum Rabi sidebands depend on the strength of the driving field  $\epsilon$  as well as the parameters  $(g(\vec{r}), \kappa, \gamma_{\perp})$ , and are found via steady-state numerical solution of the master equation.

To fully realize the quantum mechanical phenomena inherent in Equations 2.6-2.7 for strong coupling, yet another rate must be made small relative to the coherent cou-

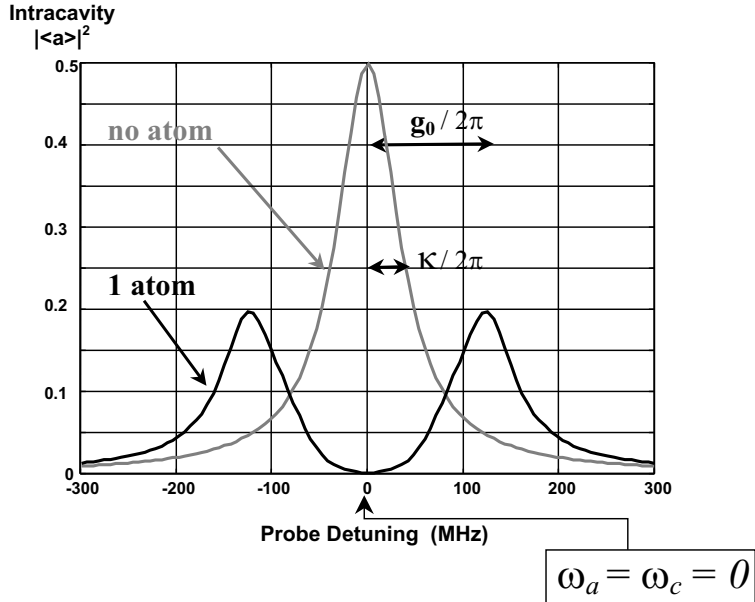


Figure 2.3: Vacuum Rabi splitting for  $(g_0, \kappa, \gamma_{\perp}) = 2\pi(120, 40, 2.6)$  MHz and 0.5 photons in the empty cavity on resonance. Intracavity  $|\langle a \rangle|^2$ , from steady-state solution of the master equation, is plotted as a function of probe detuning  $(\omega_p - \omega_a)/2\pi$ .

pling. This is the rate for decoherence as information exits the system via movement of the individual atoms contributing to the effective atom number  $N$ . If excitation is distributed among an ensemble of atoms, each poorly coupled or coupled for a short time as it flies across the cavity mode, the true structure of the single-atom Jaynes-Cummings ladder cannot be observed. Thus experiments designed to probe the strong coupling regime must be carried out with cold atoms, in a situation where atom number  $N \sim 1$  is realized through an actual single atom strongly coupled for a time  $\tau$  satisfying  $1/\tau \ll g_0$ . Experiments of this type to date have involved a cloud of atoms trapped in a magneto-optical trap (MOT), cooled via standard sub-Doppler techniques, and then dropped or launched so that single atoms arrive in the cavity mode volume with small velocities and interact one at a time with the cavity field. Such an experiment is shown schematically in Figure 2.4; single atoms fall through the cavity mode and are detected via real-time changes in the transmission of a continuously monitored cavity probe beam [46, 20, 47, 48, 49]. More recently, single atoms have also been caught within the cavity by means of the quantized field [25, 50] or trapped there using a separate far-off-resonance trap (FORT) [51, 52]. Other efforts

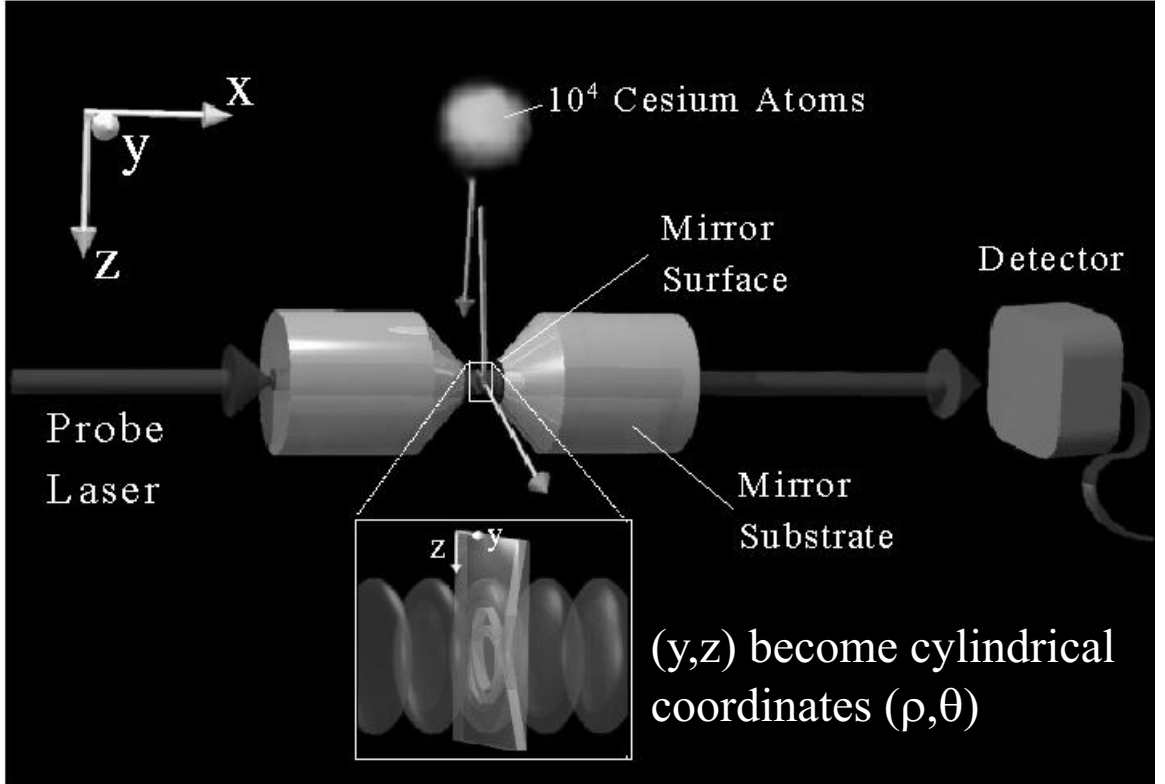


Figure 2.4: Schematic experiment with cold atoms in cavity QED.

in progress include the use of cavities with magnetic traps for atoms [53], trapped and cooled ions [54, 55], and FORTs chaining atoms through the cavity in the transverse direction [56, 57].

Cavity QED with cold atoms in the strong coupling regime has enabled observation of the vacuum Rabi splitting for single atoms in an optical cavity, and of the quantum saturation of the atom-cavity response. In Ref. [20], for example, measurements of cavity transmission vs. input driving field strength clearly deviate from the prediction of the optical bistability equation and are instead consistent with numerical solutions of the quantum master equation itself (Figure 2.2, solid line and experimental data points). This work was carried out with laser-cooled Cesium atoms dropped through an optical cavity of length  $l = 10.1 \mu m$  and finesse  $F = 180,000$ , leading to  $(g_0, \kappa, \gamma_{\perp}) = 2\pi(120, 40, 2.6) \text{ MHz}$  and critical parameters  $(N_0, m_0) = (0.014, 2 \cdot 10^{-4})$ . This and subsequent experiments [25, 50, 51] thus operate in a regime of critical atom number and saturation photon number orders of magnitude below unity. In this case

driving fields which populate the cavity mode with coherent amplitudes at or even below one photon are sufficient to induce nonlinear response in the system. Likewise, effective atom numbers well below one interact strongly with the cavity field and alter the cavity transmission spectrum. Therefore the presence of a single atom, even when poorly coupled or just entering the cavity mode volume, can be detected with high signal-to-noise via the transmission of a probe beam through the cavity.

### 2.5.1 Real-Time Detection and Trapping with Single Photons

A striking demonstration of strong coupling in optical cavity QED comes in recent experiments which actually bind an atom in the cavity by creating the “bound-state”  $|-\rangle$  of the Jaynes-Cummings ladder [25, 50]. Figure 2.5(a) shows the ladder of atom-cavity energy eigenvalues with emphasis on the continuous evolution from bare to joint eigenstates as a function of atom-cavity coupling, and therefore of atomic position within the cavity mode. As an atom falls through the Gaussian transverse profile of the cavity mode, the eigenvalues evolve as illustrated in the figure. Concentrating on the ground and first excited states of the manifold, we will see that this eigenvalue structure enables both sensing and trapping of an atom by means of the cavity field.

If the cavity is probed at its bare resonance frequency  $\omega_p \approx \omega_c$ , we see from Figure 2.5 that this probe will be moved out of resonance as the atom-cavity coupling increases, causing a drop in transmitted light as an atom moves into the cavity. If, on the other hand, the probe is tuned below the cavity resonance  $\omega_p < \omega_c$  and instead near the lower dressed state, it will move into resonance as an atom becomes more strongly coupled. In this case the cavity transmission is originally low and increases as an atom moves toward regions of strong coupling. To see these effects quantitatively, we find steady-state solutions of the master equation to obtain the vacuum Rabi spectrum in Figure 2.5(b). This spectrum has been calculated for the experimental parameters of Ref. [25]. As seen already in the data of Ref. [20], resonant probe transmission can be reduced by factors of  $10^2 - 10^3$ , providing enormous signal-to-

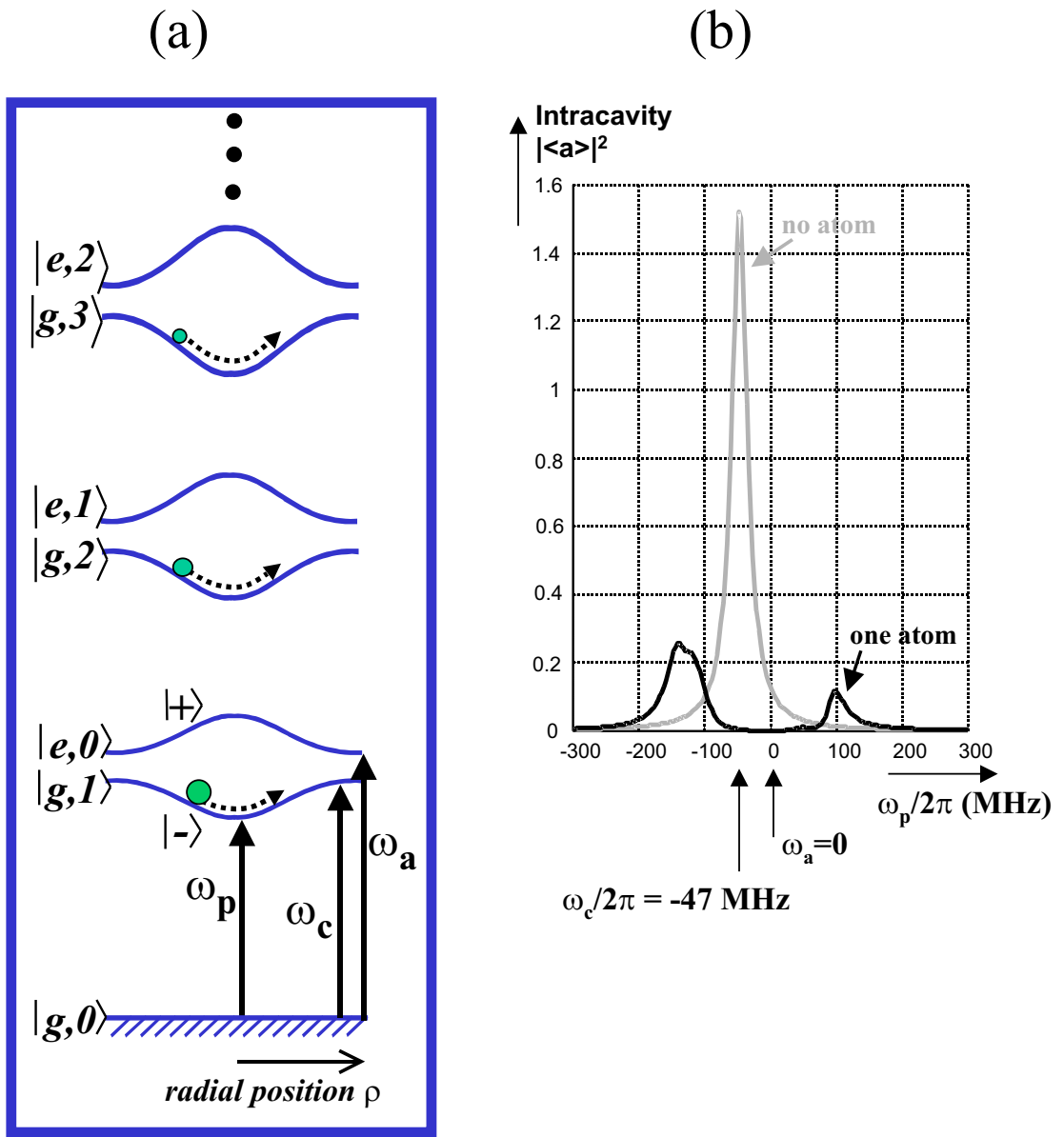


Figure 2.5: (a) Atomic-position-dependent eigenstates and (b) calculated vacuum Rabi splitting for triggered trapping experiments. Here  $(g_0, \kappa, \gamma_{\perp})/2\pi = (110, 14.2, 2.6)$  MHz,  $(\omega_c - \omega_a)/2\pi = -47$  MHz, and the drive strength corresponds to 1.56 photons in the empty cavity on resonance.

noise for detection of an intracavity atom. For a probe on the lower vacuum Rabi sideband, the transmission increase is less drastic, but probing at this frequency is nevertheless often preferable because of its effect on the atomic motion.

Thus far we have discussed strong coupling between the cavity field and atomic dipole, or internal state. We can define a further condition of strong coupling for the *external* atomic degrees of freedom, which occurs when the coherent coupling dominates the atomic kinetic energy as well. Under these circumstances the position-dependent energy eigenvalues cause an important mechanical effect on an atom interacting with the cavity mode. For instance, an attractive effective potential is felt by an atom when a probe field tuned to the lower vacuum Rabi sideband is used to populate the strong-field-seeking state  $|-\rangle$ . When this potential is large relative to the atomic kinetic energy, experimental observations range from atom-cavity scattering effects to largely conservative binding of an atom by a single-photon cavity field [20, 50, 25, 26]. The ability to both trap an atom and sense its motion in real time leads naturally to schemes to actively cool an atom in the cavity.

## 2.6 Broader Application of Real-Time Sensing Capabilities

Optical cavity QED in the strong coupling regime provides, as we have seen, a nearly closed environment for interactions between single quanta. Furthermore, it retains the chief merit of optical cavity spectroscopy in the classical regime: enhanced signal-to-noise for observation of intracavity dynamics through the well-defined output channel of cavity decay. While in the language of open quantum systems the cavity decay at rate  $\kappa$  introduces decoherence into the system, the decay is a single output mode which can be directed toward some use which actually keeps information within the broader system of interest. In the context of optimal state estimation and control, this may mean measuring the transmitted field and using that information to control the system via active feedback. In the case of quantum logic and communication, it

may mean measuring the output field or sending it efficiently to a distant cavity to be coherently interacted with a second atom there.

One measure of the capability for observation is the so-called *optical information* rate for monitoring intracavity dynamics through measurement of transmitted light. For a simple estimate of optical information, we consider the case of a resonant probe,  $\omega_p = \omega_c = \omega_a$ , whose transmission drops as an atom enters the cavity mode. The presence of an atom is thus signaled by a rate  $dI/dt$  of “missing” photons at the cavity output. This rate is given by  $dI/dt = \kappa(|\langle a \rangle|_{empty}^2 - |\langle a \rangle|_{full}^2) \approx \kappa|\langle a \rangle|_{empty}^2$  provided that  $|\langle a \rangle|_{full}^2$  is very small. This is the case for strong coupling conditions but driving strength still small enough to prevent complete saturation of the atomic response. Thus  $dI/dt$  is maximized for  $|\langle a \rangle|_{full}^2 \approx m_0$  and  $|\langle a \rangle|_{empty}^2 \approx C_1^2|\langle a \rangle|_{full}^2 \approx g_0^2/\kappa^2$ . This rough argument yields an optical information rate  $dI/dt = g_0^2/\kappa$ ; the same quantity appears in a formal treatment of the resonant-probing case as well as in calculations of probing on the lower vacuum Rabi sideband and in analytic expressions for various schemes to monitor both atomic position and atom-cavity internal states in a strong-driving limit [58].

### 2.6.1 More Intuitive Arguments for Optical Information and Critical Parameters

What can we say about the physical significance of  $g_0^2/\kappa$ ? A key question seems to be: How much does the atom prefer coupling into the cavity over coupling into the ordinary vacuum modes available? The quantity  $g_0$  can be simply understood via

$$\frac{g_0^2}{\gamma_\perp^2} \propto \frac{\text{atomic radiative volume}}{\text{cavity mode volume}}. \quad (2.9)$$

How does this relate to our previous definition (from Section 2.1) of  $\hbar g_0 = \vec{\mu} \cdot \vec{E}_{1,cav}$  where  $\vec{E}_{1,cav}$  is the electric field of a single photon in the cavity mode? The atomic decay rate  $\gamma_\perp$  is itself given by  $\vec{\mu} \cdot \vec{E}_{1,rad}$  where  $\vec{E}_{1,rad}$  is the electric field of a single photon in the atomic radiative volume; this relationship can be viewed as defining the

atomic radiative volume. Alternatively the atomic radiative volume can be roughly set as  $\sim \lambda^2 \cdot (c/\gamma_{\perp})$ , i.e., a cross-sectional area  $\sim \lambda^2$  extending over a distance  $c/\gamma_{\perp}$ . If we remember  $\gamma_{\perp} \propto \mu^2/\lambda^3$  from the Fermi golden rule, and employ  $E_{1,rad} \propto \sqrt{\hbar\omega/V_{rad}}$ , a few lines of algebra will show the internal consistency of these relations. Either way, we then recall that the electric field of a single photon confined to a given mode volume is inversely proportional to the square root of that mode volume, yielding the relationship stated above in Equation 2.9.

Since it takes half a photon per radiative volume to saturate the atom, it takes  $\gamma_{\perp}^2/2g_0^2$  photons per cavity volume for saturation, neatly providing the saturation photon number  $m_0$ .

Now consider some (saturating) excitation shared between atom and field. The atomic spontaneous emission can dump excitation at rate  $\gamma_{\perp}$ , while the cavity sheds whatever it has at rate  $2\kappa$ . But the cavity only needs to hold  $m_0$  of excitation to saturate the atom, so the cavity is dumping excitation at overall rate  $m_0(2\kappa) = \frac{\gamma_{\perp}^2}{2g_0^2}(2\kappa)$ . Thus the rate of overall system decay through the atom compares to that through the cavity as

$$\frac{\Gamma_{sys,atom}}{\Gamma_{sys,cavity}} = \frac{\gamma_{\perp}}{\frac{\gamma_{\perp}^2}{2g_0^2}2\kappa} = \frac{g_0^2}{\kappa\gamma_{\perp}} = 2C_1 = 2/N_0. \quad (2.10)$$

The critical atom number then shows up as roughly the number of atoms necessary to partner equally with the cavity in disposal of shared excitation.

Finally, suppose we are driving the cavity (on resonance) with enough power to keep the system saturated at roughly one excitation in the atom and  $m_0$  excitations in the cavity mode. The system is acting like one part empty cavity to  $2C_1$  parts excitation-eating, atom-related beast. If we take the atom away, two things will happen. First, a factor of  $2C_1$  more driving light will actually get into the system to produce excitation, since before only the empty-cavity-like part was resonant with the drive and now the whole system is. Second, all the excitation that does get in will decay through the cavity since no other channel remains. That means another factor of  $2C_1$ . Actually these are factors of  $(1 + 2C_1)/1$ , but if we assume the cooperativity

is large we need not worry about the difference. So the additional cavity output signal that tells us the atom is gone is given by the original output rate,  $m_0\kappa = \frac{\gamma_1^2}{2g_0^2}\kappa$ , multiplied by  $(2C_1)^2 = \frac{g_0^4}{\kappa^2\gamma_\perp^2}$ . This gives us (again to within the ever-present factor of two) the magical quantity  $g_0^2/\kappa$ , and we have stuck to our original resolution not to lift a pencil.

While by no means airtight, these lines of argument at least give some sense of the optical information as meaning something basic about the atom-cavity interaction.

### 2.6.2 What is the Information Good For?

The quantity  $dI/dt = g_0^2/\kappa$  corresponds to information about some aspect of the atom-cavity state accessible at a rate of over  $10^9$  per second for the current generation of strong-coupling Fabry-Perot cavities with alkali atoms. This must be compared with a rate for monitoring the same atom via light scattering in free space, where fluorescence rates do not exceed  $\approx 10^7$  per second and it is nearly impossible to imagine efficient collection of the light emitted over  $4\pi$  solid angle. This orders-of-magnitude increase in detection capability represents one of the main strengths of cavity QED in quantum state control.

This sensing ability can be brought to bear in diverse ways. In a current experiment [51, 52], an atom entering the cavity mode is detected via cavity QED and then trapped by a separate light field in a different longitudinal mode of the cavity. This far-off-resonant trap (FORT) takes advantage of the cavity buildup power to obtain intensities large enough to trap the atom even in the face of mechanical effects caused by the cavity QED probe field. The sensing ability provided by that probe field allows trapping of one and only one atom in the FORT, opening the door for schemes in quantum information science that rely on deterministic interaction of a single atom with the field.

Many such schemes fall under the general heading of quantum state synthesis, using the single-atom medium to prepare single photons and other nonclassical states of the light field. Existing methods of single-photon generation encounter difficulty in

providing true determinism of the output field, either in timing or in spatial output channel. The output channel difficulty is naturally solved in cavity QED, and efficient single-atom trapping is bringing true on-demand state generation within the realm of possibility. Proposals encompass not only single-photon generation but also numerous other state preparations, such as the photon turnstile and the single-atom laser (see, e.g., [59]), as well as schemes for entanglement generation made possible by the high detection efficiencies [60].

Another direction which relies on real-time sensing in cavity QED is quantum state estimation and quantum feedback. Real-time active feedback methods infer the system state and steer it toward some target value; as cavity-assisted state measurement approaches its fundamental quantum limit, a servo will be limited by measurement backaction effects. Performance of such a control loop will depend on minimal-disturbance measurements for the variable of interest, and the dynamics should exhibit the evolution-and-collapse patterns characteristic of quantum trajectory theory [61, 62]. Experiments on real-time feedback to atomic position explore this issue from one direction, but the concept applies equally to other aspects of the overall atom-cavity state. For instance, ongoing experiments [63] also apply real-time sensing and feedback towards the goal of designing novel states of the cavity output field itself.

## Chapter 3

# Experimental Tools and Technical Challenges

My involvement in cavity QED research as a student has encompassed three experimental setups for cold-atom cavity QED with very short cavities. All three stages share a basic experimental scheme and many technical tools and challenges. In this chapter my intent is to present a general summary of the experiments. The details of the atom-cavity microscope experiment are presented thoroughly in Christina Hood's thesis [19], while an even more in-depth discussion of several experimental issues can be found in Quentin Turchette's thesis [27]. Chapter 6 presents in detail the new or altered aspects of the active feedback experiment. Chapter 7 returns to some technical issues, particularly those related to the all-important high-finesse cavities, and expands on some aspects which may be useful for future efforts though not directly essential for understanding current work.

### 3.1 Principal Components of the Experiment

A schematic depicting the heart of the cold-atom cavity QED experiment is shown in Figure 3.1. Cesium atoms are trapped in a magneto-optical trap (MOT) [64, 65], cooled to a few microkelvin using standard sub-Doppler cooling techniques [66, 67, 68], and released to fall through the cavity mode volume. The cavity mode is continuously driven by a probe laser coupled into the cavity at one end; the light transmitted out the other end is detected with an optical balanced heterodyne setup, providing real-

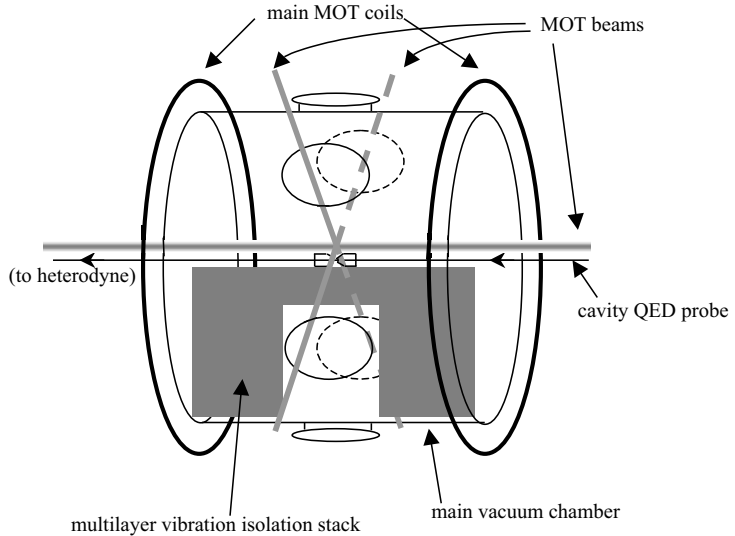


Figure 3.1: Core of experimental setup: cavity, probe, detection, and MOT

time information on the atom-cavity interaction. The detected transmission signal is acquired and digitized for storage, and the signal is also used to condition changes in the probe field for trapping or feedback. Throughout the experiment, stabilization of the lasers and in particular of the physics cavity itself are crucial to the generation of meaningful data in the lab.

## 3.2 Magneto-Optical Trap and Sub-Doppler Polarization Gradient Cooling

The magneto-optical trap [64, 65, 69, 70] has become a standard workhorse of modern optical physics with neutral atoms. Its success hinges on the elegant combination of spatial trapping with a simultaneous cooling mechanism. Counterpropagating light beams of opposite circular polarization are tuned slightly below resonance with an atomic ground to excited state transition. This red-detuning technique by itself provides Doppler cooling [71, 72], so named because the Doppler effect causes an atom to absorb light and thus momentum preferentially from the beam it is moving towards, while spontaneous emission occurs in a random spatial direction. The result is an average light force, proportional to velocity and oppositely directed, which cools the

sample. In three dimensions, energy is removed as moving atoms absorb photons from the red-detuned beams ( $\omega < \omega_a$ ) and re-emit with a frequency spread of  $\gamma_{\perp}$  centered around  $\omega_a$ . The limiting temperature of this cooling mechanism is the Doppler temperature  $k_B T_D = \hbar \gamma_{\perp}$  which for Cesium gives  $T_D = 120 \mu K$ .

The spatial restoring force relies on the introduction of a quadrupole magnetic field, produced by an anti-Helmholtz coil configuration in combination with Helmholtz bias coils to zero the magnetic field. The magnetic field along an axis is  $B_z \propto z$ , producing a Zeeman shift in the atomic transition  $m_F \rightarrow m'_F = m_F \pm 1$  which is linear in atomic distance from the trap center. When the frequency of a given transition is decreased, it becomes closer to resonant with the trapping light, and the atom absorbs preferentially from one of the circularly polarized beams. If the circular polarizations and magnetic field gradient are chosen correctly, a displaced atom absorbs more strongly from the beam which will push it back to the center, providing the restoring force for the MOT.

The relevant levels for Cesium are shown in Figure 3.2. Physics takes place on the  $6S_{1/2}, F = 4 \rightarrow 6P_{3/2}, F = 5$  transition of atomic Cesium, with a closed or “cycling” transition on  $m_F = 4 \rightarrow m'_F = 5$ . The excited state lifetime is 30 ns, corresponding to decay rate  $\gamma_{||} = 2\pi(5.2 \text{ MHz})$  or  $\gamma_{\perp} = 2\pi(2.6 \text{ MHz})$  [73, 74].

A final ingredient is the addition of a repumping laser on the  $F = 3 \rightarrow F' = 4$  transition to recycle population which otherwise slowly accumulates in the non-trapping  $F = 3$  ground state due to off-resonant transitions. The repumping laser remains on at a constant strength throughout the MOT loading and the sub-Doppler cooling described below.

After a MOT is loaded (a process of some hundreds of milliseconds to a few seconds), the magnetic field gradient is turned off and the light intensity is turned down to accomplish a short pulse of sub-Doppler cooling on the atoms [66]. Standard sub-Doppler cooling via polarization gradient effects brings Cesium fairly easily to final temperatures of a few to a few tens of microKelvin, depending largely on the degree of heroics associated with magnetic field zeroing [67, 68].

Diagnostics on the final temperature are performed via time-of-flight imaging of

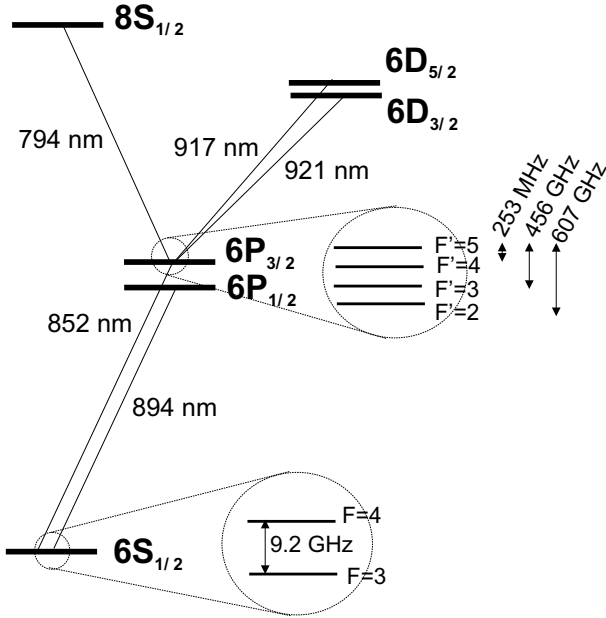


Figure 3.2: Cesium level structure for cooling, trapping, and cavity QED. The  $6S_{1/2}, F = 4 \rightarrow 6P_{3/2}, F' = 5$  transition is at 852.359 nm.

the expanding cloud after trapping and sub-Doppler cooling, using a brief pulse of the trapping light beams. Magnetic field trim coils are adjusted to ensure that the cloud falls straight down and with as little expansion as possible. A slight difficulty arises because our MOT is constructed as close as possible to the cavity, giving us little time to observe expansion before the cloud hits the mirror substrates. In practice we perform final field zeroing by raising the MOT position a few millimeters with a vertical bias coil; we then have about 30 ms of accessible fall time before the atoms leave the beam profile and hit the cavity substrates. Cooling is optimized with the trap raised in this way and we assume fields will be nearly zeroed for the lower trap position in the actual experiment.

### 3.3 Probe Beam and Local Oscillator Generation and Stabilization

The cavity QED probe beam in these experiments has a very modest requirement for optical power. Since we typically work at intracavity photon numbers of one or

smaller, the mode-matched optical power delivered to the cavity is on the order of  $(\hbar\omega)\kappa \sim 10$  pW or less. This means in practice that the probe beam is maintained at some sensible working strength on the order of a milliWatt and then severely attenuated with a stack of neutral-density filters just before being sent to the cavity. The probe laser also serves as the source for a strong local oscillator (LO) beam used in the heterodyne detection of the cavity-transmitted light, as described later in this chapter. We typically use an LO strength of 5 mW.

The probe beam in the atom-cavity microscope and previous experiments was generated by a Ti:Sapph laser pumped with 5 Watts of green light (532 nm) from a Spectra Physics Millennia V solid-state diode-pumped unit. With no water cooling of the Ti:Sapph crystal, single-mode output power at 852 nm was typically 300-350 mW. This light was split to: (1) a Cs FM saturated absorption spectroscopy [75] path to generate an error signal for locking the laser to Cesium, (2) a local oscillator path intensity stabilized using a ThorLabs liquid-crystal-based intensity stabilizer, and (3) the probe beam path including frequency shifting, intensity stabilization, rapidly switchable intensity adjustment, and mode-matching. The final probe beam in this setup consisted of a carrier  $\sim 800$  MHz blue-detuned from  $(\omega_a, \omega_c)$  which received sidebands at  $\sim \pm 800$  MHz through a traveling-wave modulator so that the lower sideband acted as the near-resonant probe. The carrier and upper sideband were ignored as too far detuned to interact significantly with the atoms. In practice, care was required to ensure negligible effect from the carrier, since it was far-detuned but typically a factor of a hundred stronger than the probe itself. While a given probe strength could be achieved by many combinations of overall optical power and RF modulation index, the optical power had to be set low enough and RF power high enough to keep the carrier from noticeably altering the atom-cavity system.

In the active-feedback experiment, the probe beam originates from a grating-stabilized diode laser at 852 nm. The shifting, switching, and stabilization of this beam are described in detail in Chapter 6.

### 3.4 The Physics Cavity

The heart of the cold-atoms cavity QED experiment is the physics cavity itself. The atom-cavity microscope and active-feedback experiments use cavities of length  $l \approx 10 \mu m$  and finesse  $F \approx 480,000$ . The mirrors have radius of curvature  $R = 10 cm$ , leading to cavity field waists  $w_0 \approx 14 \mu m$  for the  $TEM_{00}$  mode. Mirror properties and cavity mounting are described in detail in [19] and in Chapters 6 and 7; here I outline the basic construction and some important technical details related to length stability and birefringence.

The cavity is mounted on a solid OFHC copper block, which sits on a vibration-isolation stack within the vacuum chamber. Each (cylindrical) mirror substrate sits in a v-block to which it is attached by glue; the v-blocks in turn are glued atop shear mode PZTs which are glued to the copper mount piece. Cavity length is tuned and stabilized via voltage applied to the shearing PZTs. The strategy of these experiments is to use the cavity's transmission of a fixed-frequency probe beam to infer a measurement of atom-cavity interactions; thus stabilization of the cavity length (resonance frequency) is essential. In fact, cavity length excursions are the principal source of technical noise in the measurements. In particular, mechanical resonances of the mounting stack must if possible be engineered out of the frequency range where meaningful atomic motional signals are expected. This issue, which I addressed via overall mount/PZT selection and rigidity of attachment, is dealt with more thoroughly in [19] and in Chapter 6.

A second nagging concern in cavity design is birefringence, treated more fully in Chapters 6 and 7. Experience suggests that glue applied to the mirror substrates causes stress-induced birefringence in the mirror coatings, so that the cavity alters all input polarizations save the two linear cavity eigenpolarizations. This is inconvenient for experiments in which we wish to work with circularly polarized light to maintain the cycling transition  $m_F = 4 \rightarrow m'_F = 5$ . In practice we attempt to minimize cavity birefringence by applying the minimum amount of glue necessary, at the farthest possible distance from the mirror surfaces. We then use circularly polarized probe

light, but a small fraction of the opposite circular polarization in fact builds up in the cavity. This situation allows a slow drain of population from the interacting ( $F = 4$ ) ground state, motivating the use of a repumping beam on  $F = 3 \rightarrow F' = 4$ . This beam comes from the same laser as the MOT repumping light, but is overlapped with the cavity QED probe for injection into the cavity.

Finally, this discussion of cavity construction and geometry is a good place to include a note on delivery of single atoms to the cavity mode. Given a MOT with  $10^4$  or more atoms cooled and dropped directly onto the cavity, how do we obtain a situation where atoms traverse the cavity mode one at a time? Figure 3.3 provides a sense of how this occurs. The figure shows a to-scale rendering of the cavity mirror surfaces and  $TEM_{00}$  mode profile in the center of the mirrors. The cavity geometry itself clearly cuts off a large fraction of the atom flux to the interaction region, by imposing a very strict limit on atomic velocity along the cavity axis. Indeed, for an atom to enter the gap at the top of the mirror substrates and reach the cavity mode without hitting a mirror, the axial velocity must be less than about  $4\text{ mm/s}$  corresponding to an axial temperature of  $\sim 0.1\text{ }\mu K$ . Thus single atoms are easy to come by in the experiment.

### 3.5 Vacuum Chamber

The experiments are conducted under UHV conditions in a chamber where steady-state pressure is maintained by ion pumping with Varian Starcell pumps. Pressure within the chamber is measured using Bayard-Alpert ionization gauges. The atoms are supplied from a Cesium reservoir initially loaded with a one-gram ampule of atomic Cesium. The entire chamber (in the atom-cavity microscope) or just the upper chamber (in the active-feedback experiment) is operated as a Cesium vapor cell replenished periodically by opening a valve to the reservoir and/or heating it gently. The pressure in the chamber under these conditions is a few times  $10^{-8}$  torr. Pressure in the actual cavity region is difficult to accurately measure, but it could plausibly be significantly higher than the overall chamber pressure due to (1)

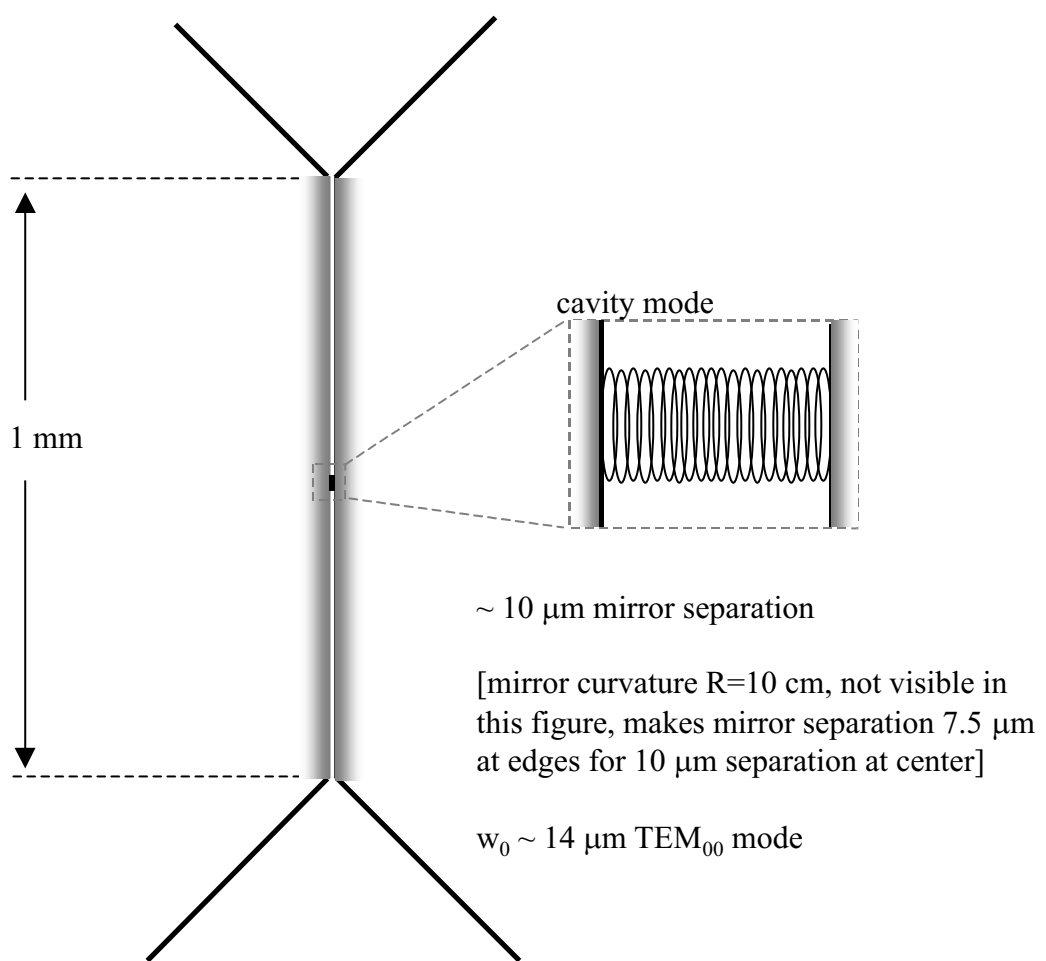


Figure 3.3: Cavity mirrors, spacing, and field mode depicted to scale.

low conductance given the geometry shown in Figure 3.3 and (2) concentration of marginal UHV materials close to the cavity because they are involved in the cavity mount itself. The most realistic prospect for an intracavity pressure measurement is trapped atom lifetime itself. This prospect is not sensible for our single-photon trapping experiments, since lifetimes are  $\lesssim 1$  ms and even a background pressure of  $10^{-8}$  torr allows a collisional lifetime of about 0.5 s. However, experiments using a far-off-resonant trap in a similar setting now reach lifetimes of  $\gtrsim 2$  s and demand more careful consideration of background limits [76]. Better understanding of other loss mechanisms in these experiments could yield some useful limits on the intracavity vacuum pressure in the near future.

As mentioned, background collisions do not limit trapped-atom lifetimes in our current single-photon trapping experiments. From this point of view, better vacuum only becomes an issue as we consider the future implementation of feedback, cooling, or auxiliary trapping schemes that will drastically enhance atom-cavity dwell times. However, one other advantage also accrues from an improved vacuum at the cavity position. This is the possible increase in cavity longevity by slow-down of the process whereby Cesium vapor atoms coat the mirror surfaces. Previous experiments have seen degradation of cavity finesse after approximately 1.5 to 2 years in an experiment; while the coating process is not known to be responsible, two pieces of circumstantial evidence suggest it is worth guarding against. First, after vacuum was broken on these past experiments and the mirrors were examined, “stars” of oxidized Cesium were prominent on the mirror surfaces (Figure 3.4). Second, the cavity of [51, 52], which is sheltered from direct contact with the Cs vapor cell region in that apparatus, has already seen an unusually long period of nearly four years of experimental usefulness. The combination of all these considerations motivated the transition to a differentially pumped chamber for the active-feedback experiment, as discussed in Chapter 6.

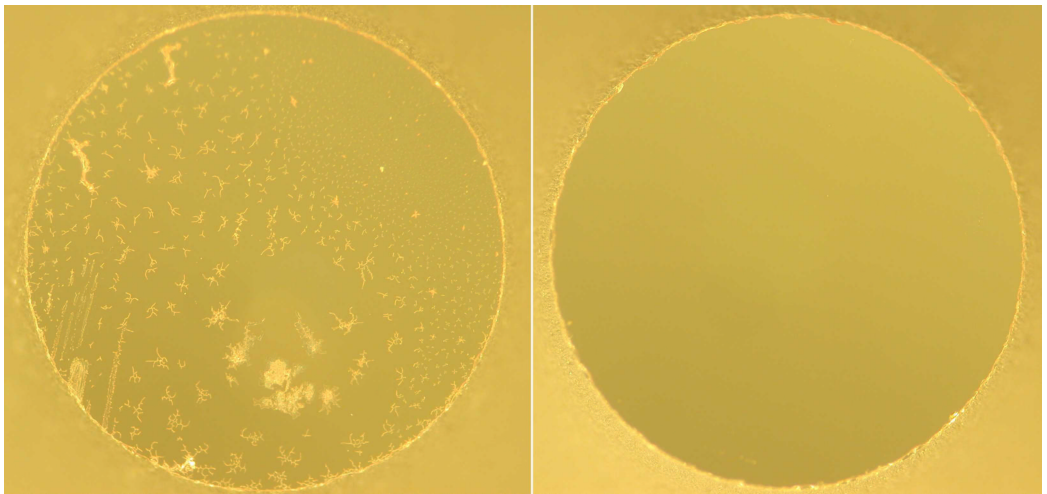


Figure 3.4: Oxidized Cesium on the surface of a mirror removed from a well-used physics cavity. A clean mirror surface is shown for comparison. Each mirror surface has a diameter of 1 mm.

### 3.6 Locking of Laser Frequency and Cavity Length

The probe beam frequency  $\omega_p$  and cavity resonance  $\omega_c$  must be stabilized to Cesium for fixed detuning from  $\omega_a$ , but need not be locked to much better than 1 MHz given the physics cavity linewidths of more than 10 MHz; this large cavity linewidth, despite the high finesse, is a result of very short cavity length. The probe frequency is referenced to Cesium via FM saturated absorption spectroscopy [77, 78, 75].

To obtain a rough length-stability requirement for the cavity, we note that while the full atom-cavity coupling  $g_0$  shifts the system resonance by  $\sim 10\kappa$ , we want to detect the effects of small fractional changes in  $g(\vec{r})$  which shift the system resonance by small fractions of  $\kappa$ . If for a cavity of width  $\kappa/2\pi \sim 14$  MHz we require  $\omega_c/2\pi$  to be stabilized to about 1 MHz, this translates to a length stability on the order of  $10 \text{ fm} = 10^{-14} \text{ m}$ . While this stability requirement on the order of atomic nuclear dimensions may initially seem nonsensical, this is of course the position averaged over the spatial cavity mode profile and over the fastest dynamical and measurement timescales of the system.

The realization of laser and cavity locks in the atom-cavity microscope experiment is treated in [19]; the Ti:Sapph frequency is locked to Cesium and the physics cavity

length is locked to the probe transmission itself, with lock blanking during an atomic transit. The rather different methods of the active-feedback experiment are presented in Chapter 6.

### 3.7 Heterodyne Detection and Calibration

Experiments with intracavity photon numbers of roughly 0.05 to 1 imply a cavity transmission signal on the order of 1 to 10 picoWatts at 852 nm. Signal powers in this range suggest the use either of photon counting or of optical homodyne/heterodyne methods for detection with reasonable signal-to-noise. While photon counting provides a measurement of  $\langle a^\dagger a \rangle$  for the output field, the balanced heterodyne detection we employ produces a photocurrent proportional to  $\langle a \rangle$ . It can be used to measure both amplitude and phase of the field [47], but in our experiments we measure only  $|\langle a \rangle|^2$  as discussed in the next section. For a coherent field  $\langle a^\dagger a \rangle = |\langle a \rangle|^2$ , but for our experimental parameters there is a small ( $\approx 20\%$ ) difference between these quantities when an atom is strongly coupled to the cavity mode [19]. This distinction is much more pronounced when detecting either  $|\langle a \rangle|^2$  or  $\langle a^\dagger a \rangle$  with a probe close to the cavity resonance frequency, rather than near the lower vacuum Rabi sideband as in our triggered-trapping experiments.

Figure 3.5 illustrates the principle of balanced heterodyne detection for a weak signal beam. The most basic idea is to encode the signal field as an RF beatnote on a much stronger local oscillator field. The signal and LO are phase-coherent, coming from the same laser, but are deliberately shifted away from one another by an RF frequency shift, in our case in the range  $\approx 10 - 100$  MHz. The signal field  $E_s$  and LO field  $E_{LO}$  are spatially overlapped and mixed on a 50/50 beamsplitter, yielding fields  $E_{LO} + E_s$  and  $E_{LO} - E_s$  at the two beamsplitter output ports. These fields are incident on balanced photodetectors whose photocurrents are then subtracted, yielding a difference photocurrent proportional to the product of the two fields:

$$i_- = i_1 - i_2 \propto (E_{LO} + E_s)^2 - (E_{LO} - E_s)^2 \propto E_{LO}E_s. \quad (3.1)$$

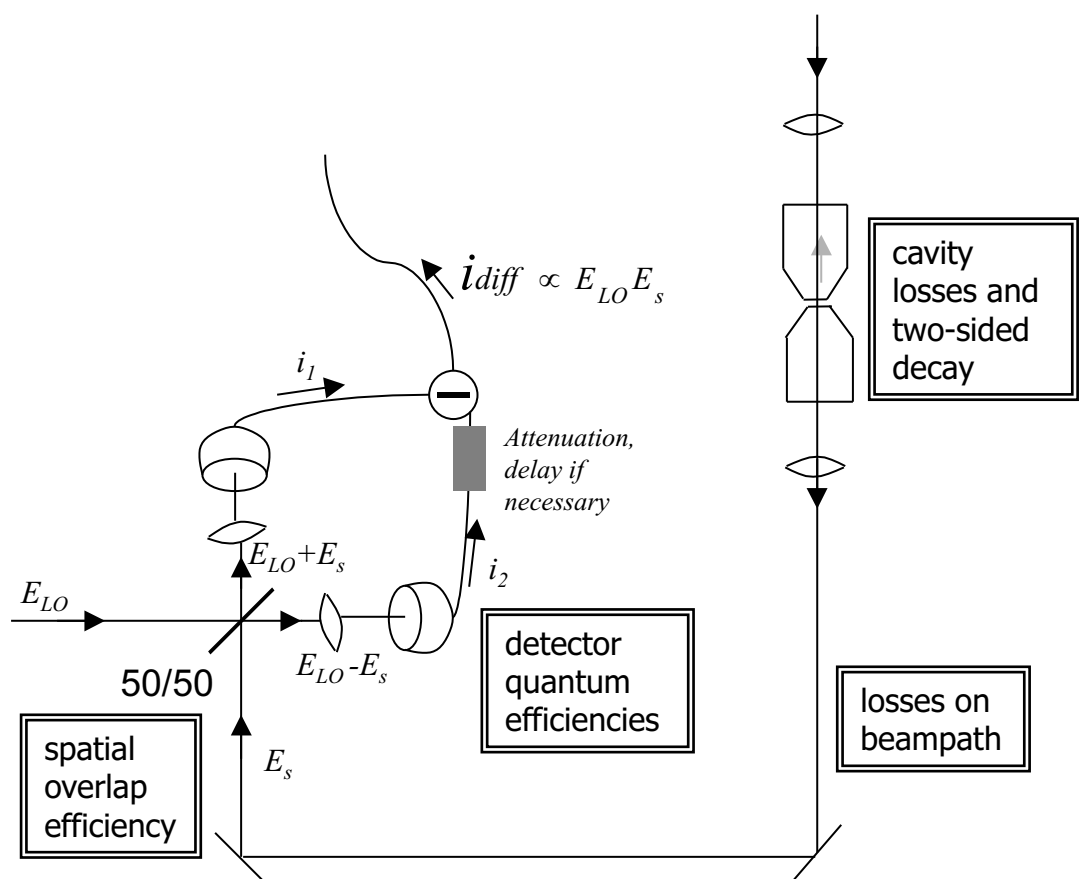


Figure 3.5: Heterodyne operation and factors contributing to detection efficiency.

If we further break down the LO and signal beams into their amplitude and noise,  $E_{LO} = A_{LO} + N_{LO}$  and  $E_s = A_s + N_s$ , we have

$$i_- \propto A_{LO}A_s + A_{LO}N_s + N_{LO}A_s + N_{LO}N_s. \quad (3.2)$$

The terms above are written in decreasing order of importance in the desired configuration of a balanced heterodyne detector; the relegation of  $N_{LO}$  to the obscurity of the last two terms allows us to write  $i_- \propto A_{LO}(A_s + N_s) \approx (\text{Constant})E_s$ . This is the vaunted LO-noise immunity of the balanced heterodyne detection method.

This noise immunity operates on (at least) two distinct levels. First, the balanced configuration and subtraction of  $i_1$  and  $i_2$  eliminates photocurrent terms containing only the large LO field, so that the difference photocurrent of Equation 3.1 is strictly proportional to the signal field  $E_s$ . As long as  $A_{LO}/N_{LO} \gg 1$ , we can write  $i_- \sim (\text{Constant})E_s$ . Second, however, it is possible to ask for more. We may hope for a situation in which the noise characteristics of the photocurrent truly reflect, to leading order, only the signal noise  $N_s$  and not the LO noise  $N_{LO}$ . In this case, referring to Equation 3.2, we require more specifically that  $N_{LO}/A_{LO} \ll N_s/A_s$ . The inequality will certainly hold for shot-noise dominated weak signal and strong LO but may be more questionable if technical noise dominates. In practice the separation in size between the four terms of Equation 3.2 is not necessarily huge and the noise immunity must be carefully evaluated in operation.

In an experimental system one contends in general with imperfect balancing, both of optical powers (beamsplitter not exactly 50/50) and of detector efficiencies and gains. In optimizing the overall performance we proceed by (1) balancing the LO and signal powers on both detectors as nearly as possible and (2) attenuating the signal from one detector if necessary to achieve balancing of the resulting photocurrents at the subtractor. “Unnecessary” attenuation certainly carries the possibility of contributing excess electronic noise if that is a primary concern. Another alternative would be to deliberately unbalance the optical powers to match the detector imbalance, i.e., adjust the beamsplitter transmission directly to cancel the  $E_{LO}^2$  term in

the difference photocurrent. This would result in a nonzero  $E_s^2$  term, but insofar as  $E_s \ll E_{LO}$  this term is unimportant anyway. The one-step overall balancing method is actually a bit more difficult to carry out with certainty that one has balanced the right thing. In terms of noise immunity, though, the relative merits of step-by-step vs. overall balancing must be weighed given the details of each case. A treatment of diverse concerns in non-ideal homodyne detection can be found in [79].

Our heterodyne detection and its calibration are presented in detail in [19], and have not changed significantly from the atom-cavity microscope to the active-feedback setup. However, I revisit here the issue of overall efficiency for detection of an intracavity photon. In that experiment we measured a heterodyne efficiency (due to detector quantum efficiency and spatial mode overlap) of 48%. The cavity mirrors each had transmission of 4.5 ppm and absorption/scatter losses of 2 ppm, while we measured just the field transmitted through one mirror. Finally, propagation losses from cavity output to heterodyne were estimated at 25%; this rather large figure comes mostly from a beamsplitter which sent 20% of the light to a photomultiplier tube for locking the cavity while optimizing the heterodyne alignment. Taking into account all these contributions, we find an overall efficiency of  $\eta = (0.48) \cdot \frac{4.5}{2(4.5+2)} \cdot (0.75) = 0.125$ , or 12.5%. This is the efficiency for detecting the *total* cavity decay, which is a signal of size  $(2\kappa)|\langle a \rangle|^2$ .

However, if we neglect the two-sided nature of the cavity and quote the total signal as  $(\kappa)|\langle a \rangle|^2$ , the corresponding efficiency will be  $\eta' = 2\eta = 0.25$  or 25%. This is the origin of the 25% efficiency quoted in [25, 19] and used in simulations of the experiment. Since the detection efficiency is relevant in determining signal-to-noise for sensing of intracavity dynamics, either set of definitions can be chosen in a given calculation. However, the mutual consistency of the definitions must be carefully checked in each situation.

I conclude the whirlwind tour of heterodyne detection with two related points. First, the strength of the local oscillator beam is determined by several considerations. Clearly the LO should be very much stronger than the signal, but there is little danger of violating this criterion in our experiment. LO power must also be high enough to

ensure that overall signal-to-noise is limited by signal shot noise ( $\propto A_{LO}N_s$ ) rather than electronic noise unrelated to the light. An important upper limit in practice is the saturation of the photodetectors, not only in terms of DC power but in the (more relevant) RF band of the actual heterodyne beatnote. The LO-signal beatnote must not saturate the detectors either for the actual experimental signal (10 pW) *or* for the much larger (10 nW) signals needed to calibrate the heterodyne-to-photon-number relationship. Another cautionary note about large local oscillator power is that a tiny fraction of the LO leaking back along the signal path to the physics cavity can wreak havoc on the atom-cavity system itself. To deal with this issue for the LO power we use, the focusing lenses and detectors in both arms of the heterodyne are tilted to avoid back-reflection of the LO.

### 3.8 Data Acquisition

The heterodyne difference photocurrent is amplified and fed into a commercial Hewlett-Packard (Agilent) spectrum analyzer for detection of the component at the LO/signal RF beat frequency [80]. An initial detection bandwidth is set via the resolution and video bandwidths of the spectrum analyzer, both typically set to 100 kHz. The video output of the spectrum analyzer then measures the difference photocurrent *power* at the heterodyne beat frequency, making it proportional in the end to  $|\langle a \rangle|^2$  since the photocurrent amplitude is proportional to  $|\langle a \rangle|$ . This signal constitutes the experimental data which is digitized, processed, saved, and used for triggering/feedback via any of several different schemes. The data acquisition and triggering protocols for the atom-cavity microscope are presented in [19], while those for the active-feedback experiment are given in Chapter 6.

## Chapter 4

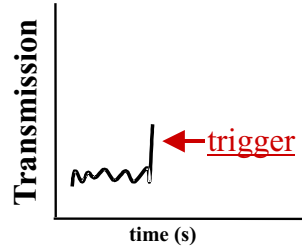
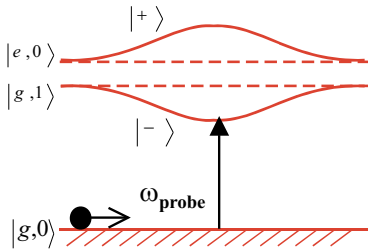
# Strong Coupling for Trapping and Sensing: The Atom-Cavity Microscope

In the work of Ref. [25, 26], much of which is also presented in [19], the sensing and trapping aspects of strong coupling are exploited to realize atom-photon binding within an optical cavity. A deep ( $\sim 2.5$  mK) potential associated with the single-quantum interaction arises from the use of a short cavity with very small mode volume ( $l = 10.9\ \mu\text{m}$ ,  $w_0 = 14.1\ \mu\text{m}$ ). This cavity, with finesse  $F = 480,000$  and  $(g, \kappa, \gamma)/2\pi = (110, 14.2, 2.6)$  MHz, gives critical photon and atom numbers  $m_0 = 2.7 \cdot 10^{-4}$ ,  $N_0 = 6.1 \cdot 10^{-3}$ . The coherent interaction energy exceeds other relevant energies in the problem, in particular the atomic kinetic energy  $E_k \approx k_B \cdot 0.46\ mK$  acquired in the 3-mm fall from the MOT to the cavity mode. Thus an atom can be caught within the cavity if the system can be driven from its ground state to the trapping state when the atom is at a maximum of the cavity field [21, 22, 23, 24].

### 4.1 Summary of Experimental Results

The implementation of this triggering strategy is summarized in Figure 4.1. Atoms are dropped through the cavity mode while cavity transmission is monitored with a weak probe beam. We define detunings of cavity and probe beam relative to the atomic resonance frequency, i.e.,  $\Delta_{ca} = \omega_c - \omega_a$  and  $\Delta_{pa} = \omega_p - \omega_a$ . The cavity is tuned

1) Detect with weak probe on red sideband.



2) Turn up driving strength to populate trapped state.

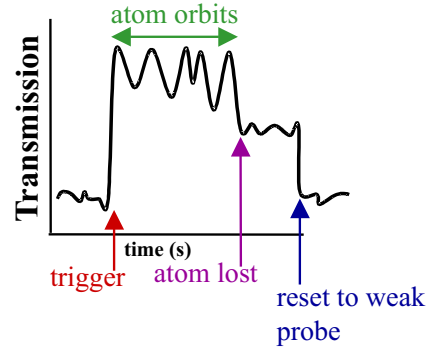
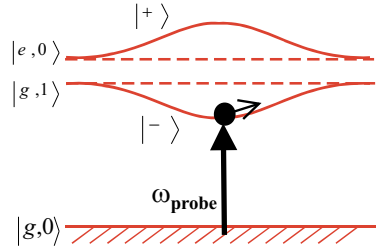


Figure 4.1: Schematic triggered-trapping protocol for the atom-cavity microscope.

slightly below the atomic resonance and the probe is placed near the lower vacuum Rabi sideband of the system,  $\Delta_{pa} < \Delta_{ca} < 0$ , with a strength of 0.05 intracavity photons. Such a weak probe allows high signal-to-noise for observation of an atom entering the cavity mode, but does not significantly populate the excited states of the atom-cavity system. Once the probe transmission rises above a predetermined threshold, indicating that an atom is in a region of strong coupling to the cavity mode, the probe power is increased to a level of about 0.3 intracavity photons to create a confining potential around the atom.

Figure 4.2(a) shows the resulting cavity transmission for an atom trapped in this way, with parameters  $\Delta_{ca}/2\pi = -47$  MHz,  $\Delta_{pa}/2\pi = -125$  MHz, and 0.3 photons in the empty cavity. Note that while the “high” probe level is set at 0.3 intracavity photons, the level rises to  $|\langle \hat{a} \rangle|^2 \sim 1$  (where  $\hat{a}$  is the cavity field annihilation operator) during parts of the measurement record due to the atom’s motion within the cavity

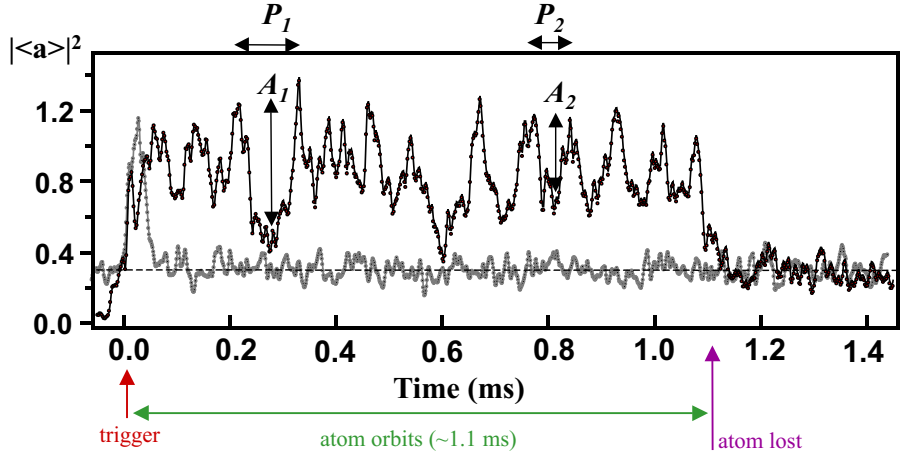


Figure 4.2: Cavity transmission record for a trapped atom moving within the cavity mode.  $(\Delta_{pa}, \Delta_{ca})/2\pi = (-125, -47)$  MHz. The probe beam is initially set to 0.05 photons in the empty cavity, and is turned up by a factor of six when triggering occurs. For contrast, an atom freely falling through a constant-strength probe field (0.3 empty-cavity photons) gives the transmission trace shown in gray.

field. Oscillations in transmission arise from atomic motion toward and away from the cavity axis, with the level falling back to 0.3 photons when the atom eventually heats out of the trap and escapes from the cavity. Using this protocol mean atom dwell times in the cavity of  $340\ \mu\text{s}$  are observed, with some rare events lasting up to several milliseconds, as compared with the  $\sim 75\ \mu\text{s}$  free-fall time for an atom to traverse the cavity mode. Lifetimes for a range of different experimental parameters are presented in [19].

Lifetimes are limited by heating associated with the many decays and re-excitations the atom-cavity system experiences during atomic motional timescales. For the parameters of Figure 4.2, the effective potential corresponds to a harmonic oscillation period of  $\tau_r = 107\ \mu\text{s}$  ( $\nu_r = 9.38\ \text{kHz}$ ) in the radial direction and  $\tau_a = 1.46\ \mu\text{s}$  ( $\nu_a = 0.688\ \text{MHz}$ ) in the axial direction, while decay and re-excitation are occurring at roughly  $\kappa$ . It is important to note that, while atoms are trapped via their dipole interaction with a red-detuned light field in a manner reminiscent of the more familiar free-space situation, the dynamics associated with the atom-cavity system are quantitatively and qualitatively different from that case [26]. In particular, a free-space potential of equal intensity would exhibit much greater diffusive heating

and thus would largely fail to trap the atoms seen in this experiment (see Section 4.4.2); furthermore, the single-atom sensing which enables the trapping strategy is only available through the use of the cavity QED system.

The most interesting feature of the measurement record for a trapped atom is undoubtedly the oscillation in transmission. The period and amplitude of these oscillations agrees quantitatively with atomic orbital motion in the Gaussian mode transverse to the cavity axis [25, 26]. Referring to Figure 4.2, we see that transmission oscillations exhibit considerable variation in period and amplitude. The examples  $(A_1, P_1)$  and  $(A_2, P_2)$  suggest that large-amplitude transmission oscillations have longer periods than small-amplitude oscillations. We expect this relationship given the anharmonic (roughly Gaussian) radial potential and initial atomic kinetic energies large enough to substantially sample the anharmonicity. Period  $P$  vs. amplitude  $A$  are plotted in Figure 4.3 for experimental and simulated transmission oscillations under the conditions of Figure 4.2. The solid curve in both plots is the prediction for one-dimensional oscillation in the known effective potential, as sketched on the right. Quantitative agreement is seen here and in numerous data sets at different trapping parameters, as set forth in [19].

Trapped atoms in this system are tightly confined close to a single antinode of the field, with typical axial amplitude  $\lesssim 50 \text{ nm}$  in simulations. Experimentally, detectable signatures from axial motion are not observed [25, 26, 19]; with our detection bandwidth of 100 kHz, the role of axial motion at  $\sim 1 \text{ MHz}$  would be to reduce the amplitude of the transmission signals we do observe, through an averaging effect. By analyzing the data for variation away from the radial predictions, we obtain an operational bound of  $\lesssim 70 \text{ nm}$  for the amplitude of axial motion, in good agreement with simulations. This corresponds to a typical variation in  $g(\vec{r})$  due to axial motion of less than 7%.

Thus transmission provides a direct, real-time record of an atom's radial distance from the cavity axis; this record can also be used along with the known effective potential to reconstruct two-dimensional trajectories. An experimental trace of transmission vs. time for a single trapped atom is shown in Figure 4.4(a), with

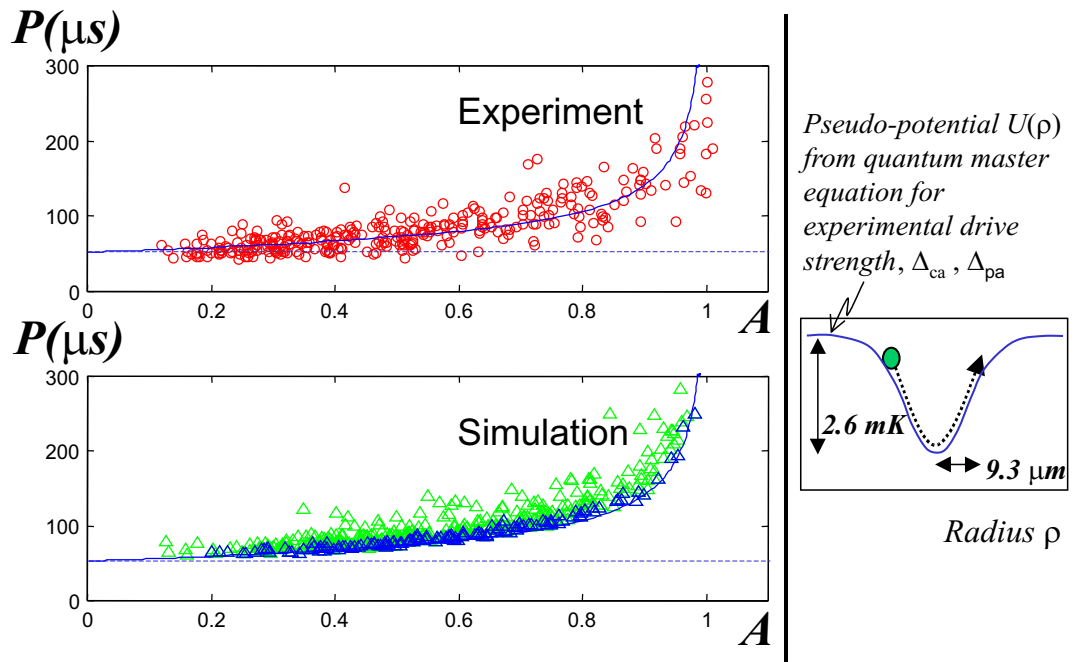


Figure 4.3: Period  $P$  vs. amplitude  $A$  of transmission oscillations for trapped atoms in experiment and simulation (parameters of Figure 4.2). Data agrees quantitatively with simulations and with the prediction from the known effective potential (solid line).

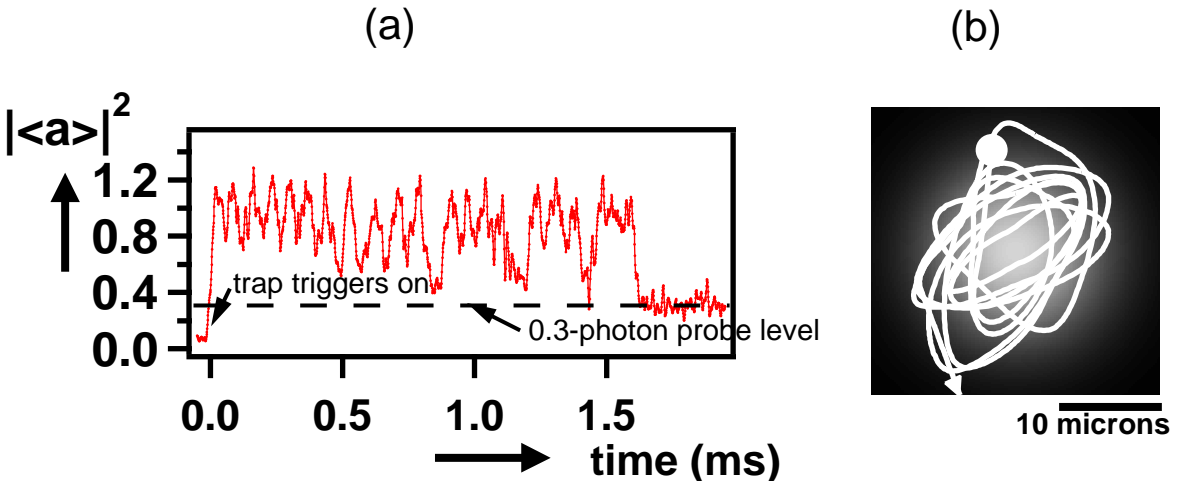


Figure 4.4: (a) Cavity transmission record for a trapped atom moving within the cavity mode (parameters of Figure 4.2). (b) Atomic trajectory in the radial ( $y,z$ ) or  $(\rho,\theta)$  plane as reconstructed from the transmission data of (a).

the corresponding reconstructed trajectory in Figure 4.4(b). The ball indicates an estimate in error of the reconstructed position, as discussed in the next section. Such reconstructions are tested by applying the method to simulated atomic trajectories. We note that while the two-dimensional reconstructions rest on the ability to neglect axial motion, it is in fact a “burst” of axial heating that typically ends an atom’s dwell time in the cavity. This axial heating occurs rapidly, so that for the final half-cycle of atomic motion in the cavity our transmission signal *is* typically considerably affected by the average over axial motion, and the two-dimensional reconstruction is not reliable at its endpoints.

## 4.2 Reconstruction Algorithms and Validation

With axial motion neglected due to its small amplitude and the separation of timescales between it and radial motion, the cavity transmission  $T(t)$  corresponds directly to a record of radial position  $\rho(t)$ . Because of the cavity mode’s cylindrical symmetry, no information is directly provided about the angular position  $\theta(t)$  of the atom in the transverse plane. However, since we know the radial effective potential via steady-

state solution to the quantum master equation, we can use the time record of  $\rho(t)$  in this cylindrically symmetric potential to derive an estimate of the atom's angular momentum  $L$  and thus of  $\dot{\theta}(t)$ . In this way we are able to use the time record of the scalar quantity  $T(t)$  to obtain a two-dimensional atom trajectory.

Because the motion is not completely conservative, but includes momentum diffusion and friction terms, angular momentum is not conserved and varies slowly during an atom's dwell time in the cavity. Thus we perform a running estimate of  $L(t)$  rather than applying a single value  $L$  throughout a given trajectory. This variation of  $L(t)$  and our ability to estimate it accurately provide important limits on the validity of such two-dimensional reconstructions, as discussed below.

The reconstruction algorithm is validated by applying it to transmission traces from simulated trapped-atom trajectories, with detection noise added. In simulations the reconstructed two-dimensional trajectory can be compared with the “actual” atomic position record to yield an estimate of error for the reconstruction method. The simulations themselves are presented in more detail in [26] and in Section 4.4.1 below. To ensure close correspondence with the detection noise in the experiment, actual “noise” data traces, taken at the appropriate transmitted powers, were added to the (otherwise noiseless) simulated transmission records.

The trajectory reconstruction algorithm is as follows (see Figure 4.5) :

- Transmission data is acquired at 100 kHz detection bandwidth and digitized at 1 megasample per second. The transmission record is then smoothed with a 20 kHz 5-pole Butterworth filter [81].
- We neglect axial motion as discussed above, assuming an atom to be confined to small-amplitude motion near a single antinode of the standing wave.
- From steady-state solution of the master equation, we know the cavity transmission as a function of atomic radius  $\rho$ . This relation is inverted through a lookup table (with linear interpolation) to turn our smoothed transmission trace into  $\rho(t)$ .

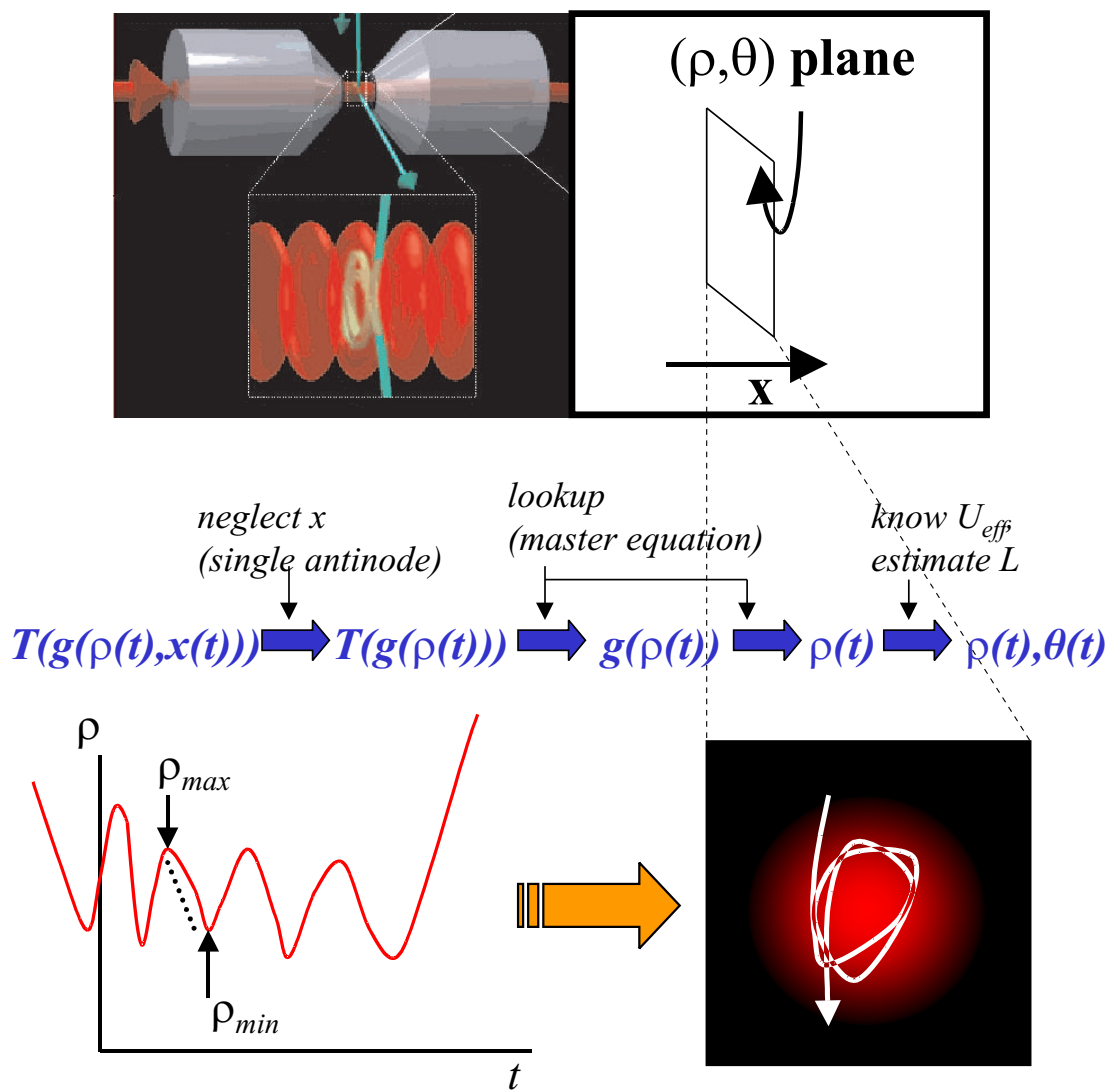


Figure 4.5: Principle of 2-D trajectory reconstructions

- Also from steady-state solution of the master equation, we know the potential  $U_{eff}(\rho)$ . We divide  $\rho(t)$  into segments between a successive maximum and minimum radius,  $\rho_{max}^i$  and  $\rho_{min}^i$ . Now for each segment we calculate an angular momentum via

$$L_i = \rho_{max}^i \rho_{min}^i \sqrt{\frac{2m(U_{eff}(\rho_{max}^i) - U_{eff}(\rho_{min}^i))}{(\rho_{max}^i)^2 - (\rho_{min}^i)^2}}. \quad (4.1)$$

- Now we have a discrete set of stepwise angular momenta. We interpolate linearly between them for a “running” estimate  $L(t)$ .
- At each time now we have an angular velocity

$$\dot{\theta}(t) = \frac{L(t)}{m(\rho(t))^2} \quad (4.2)$$

- We start the trajectory at some angle  $\theta_0$  and use  $\rho(t)$ ,  $\dot{\theta}(t)$  to obtain a 2-d trajectory.

Three basic ambiguities will be clear from this algorithm, as illustrated in Figure 4.6: 1) the sign of the angular momentum is unknown, so the trajectory has arbitrary handedness. 2) the initial angle  $\theta_0$  is arbitrary, so the resulting trajectory can be rotated freely as a unit. Trajectories are presented with the atom entering from above in a physically plausible manner, since the atom is initially falling under the influence of gravity. 3) The trajectory is constructed in two dimensions, with the axial motion confined within a single antinode, but no information is available about *which* antinode the atom occupies during the trajectory.

Reconstructions of simulated trajectories are compared with the “actual” atomic position record by first adjusting the overall sign of the reconstructed angular momentum and the initial angle  $\theta_0$  for the best possible match. An estimate of error is calculated by comparing reconstructed and actual positions over a set of simulated trajectories, excluding in each trajectory the first and last half-cycles of radial motion. These initial and final cycles are not expected to reconstruct accurately due to lack of

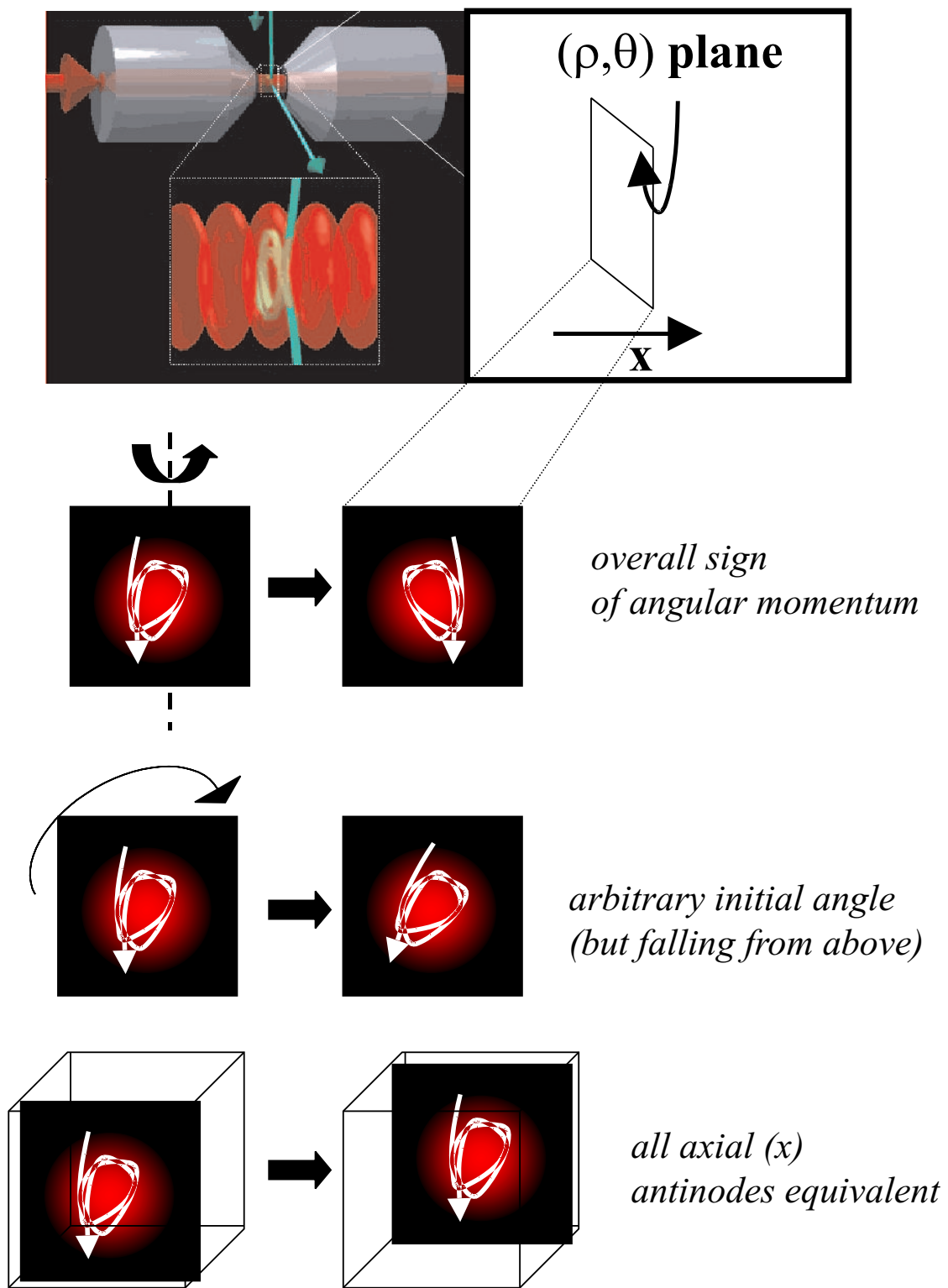


Figure 4.6: Basic ambiguities of reconstructed trajectories

confinement (for angular momentum estimation) and contamination from axial motion (as mentioned above). Several example reconstructions of simulated trajectories are shown in Figure 4.7.

Cases that cannot be reconstructed will also be clear from this algorithm and our preceding discussion. First, extremely linear trajectories cannot be reliably reconstructed because their angular momentum is so small that momentum diffusion can change them by up to (and above!) 100% during a fraction of a radial oscillation cycle. Reconstruction of such trajectories (that pass extremely close to the origin and significantly far away again) should not be attempted. These cases (about one quarter of trajectories in simulated and experimental data sets) are recognized with an estimated 97% success rate via cavity transmission traces where the transmission consistently reaches the maximum “allowed” value. Indeed the algorithm fails or gives nonsensical trajectories if these cases are attempted, as shown in Figure 4.8.

Second, trajectories that closely approach the origin (within a micron or so) cannot be reliably reconstructed from this algorithm and the data we use. The issue here is that at our probe detuning (near the lower Rabi sideband),  $g(\rho)$  and thus also  $T(\rho)$  are nearly flat near  $\rho = 0$ . In principle this problem can be overcome with improved detection schemes; I return to this question briefly at the end of Section 4.3. We note that while this limitation may seem similar to the first one, and indeed both apply to many of the same experimental data traces, they are rather fundamentally different. One is a limit arising from dynamical noise (compared to motional timescales), while the second is an issue of detection sensitivity.

Finally, the algorithm as stated above cannot deal with the case of a perfectly circular orbit which yields an angular momentum estimate of zero over zero. One might think that nearly circular orbits would be hopelessly mangled by this algorithm, especially as noise obscures what small radial variations there are. In fact, nearly-circular orbits work quite well, since the algorithm finds small wiggles (either real or noise-related) and uses them to calculate an angular momentum which is nearly that of the circular orbit at that radius. The resulting trajectory reconstruction is in fact very good, as illustrated by the examples in Figure 4.9.

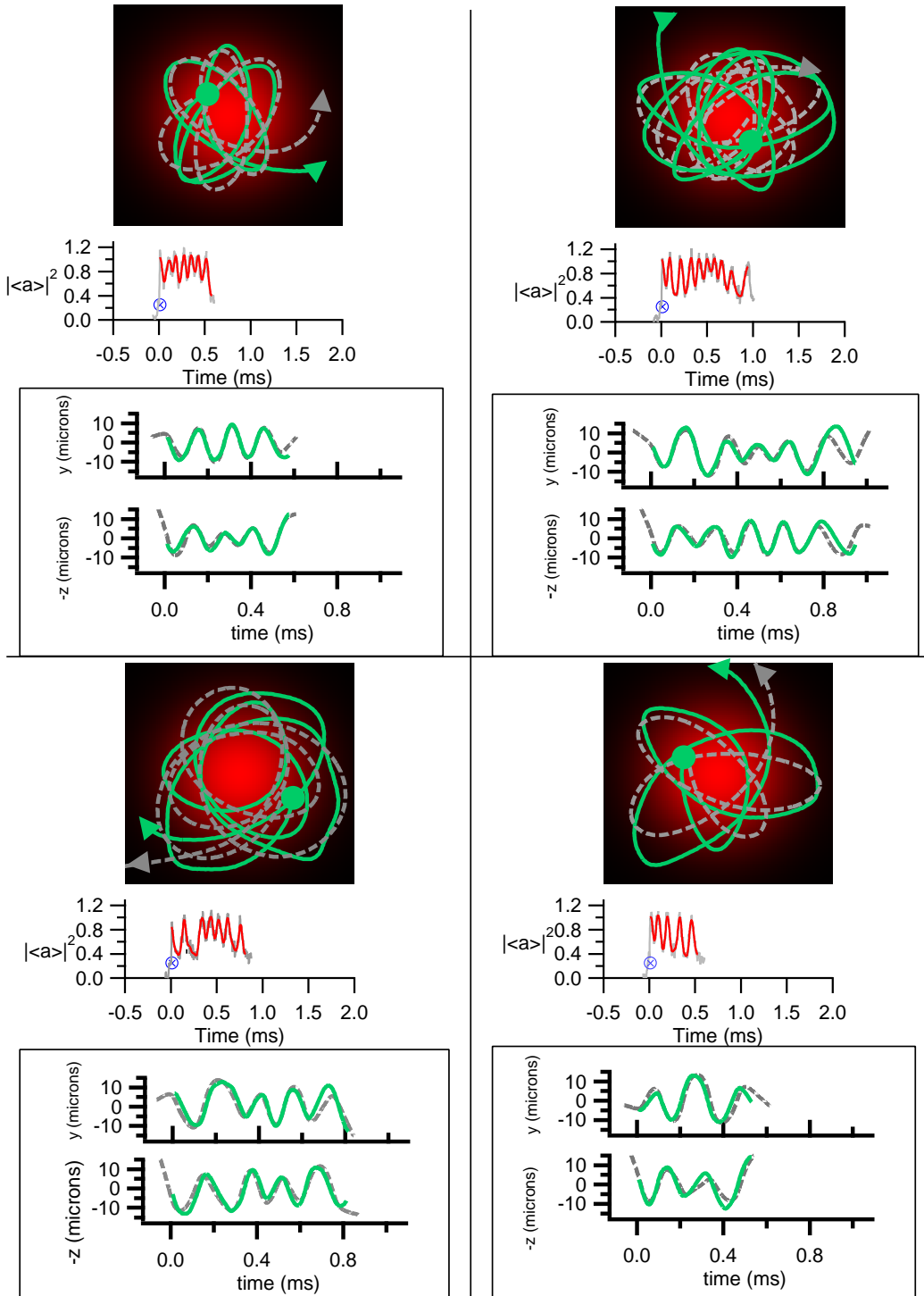


Figure 4.7: Example trajectory reconstructions from simulated transits (parameters of Figure 4.2). The two-dimensional trajectory is shown on a square  $30 \mu\text{m}$  on a side. Dotted lines indicate the “actual” simulated trajectory while solid lines show the reconstruction. In transmission traces, the filtered transmission is shown as a dark trace overlaid on the original noisy transmission signal.

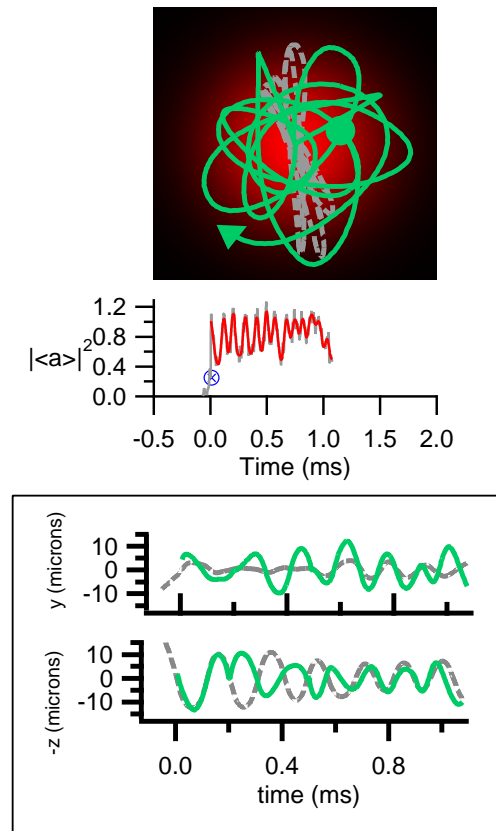


Figure 4.8: Example failed trajectory reconstruction for a linear trajectory (parameters of Figure 4.2). The two-dimensional trajectory is shown on a square  $30 \mu\text{m}$  on a side. Dotted lines indicate the “actual” simulated trajectory while solid lines show the reconstruction. In transmission traces, the filtered transmission is shown as a dark trace overlaid on the original noisy signal.

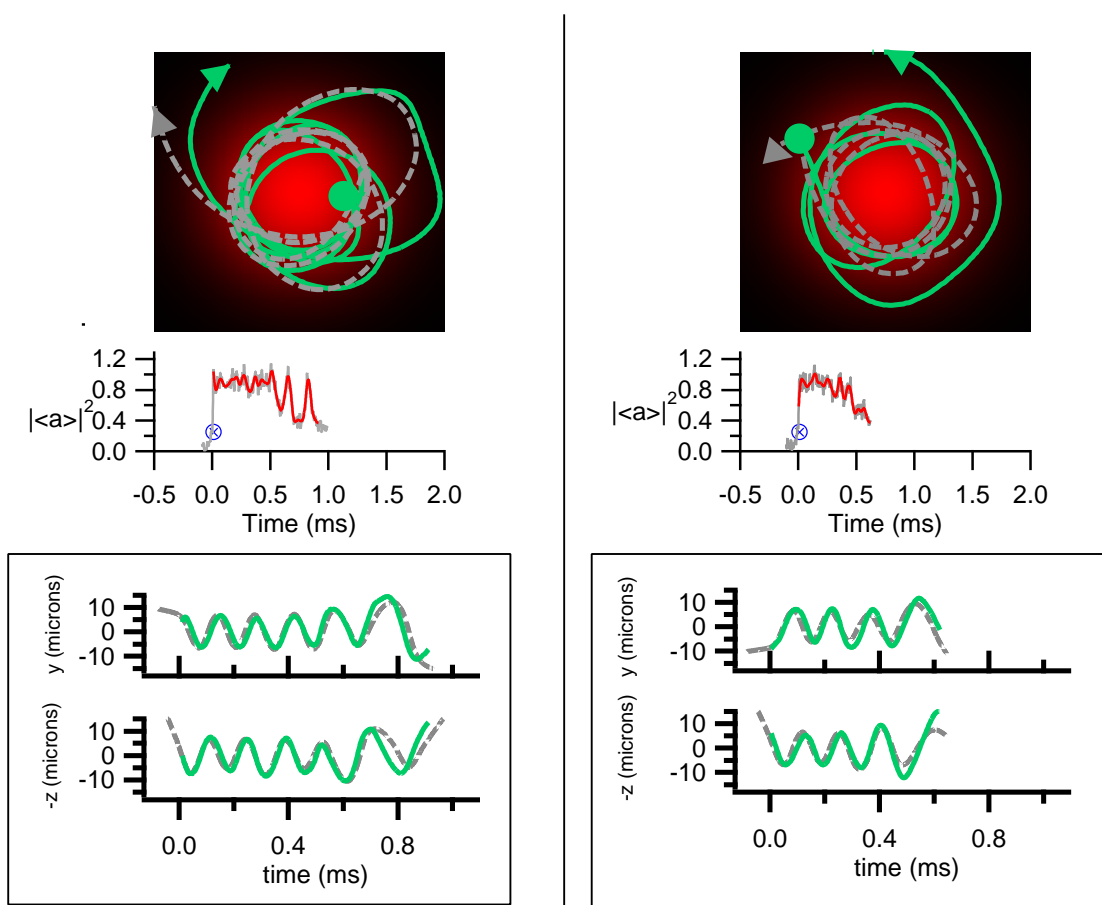


Figure 4.9: Example reconstructions of nearly circular trajectories (parameters of Figure 4.2). The two-dimensional trajectory is shown on a square  $30 \mu\text{m}$  on a side. Dotted lines indicate the “actual” simulated trajectory while solid lines show the reconstruction. In transmission traces, the filtered transmission is shown as a dark trace overlaid on the original noisy transmission signal.

A possible stumbling-block for our trajectory reconstruction method is the case of the trapped atom which has small-amplitude axial motion, heats out of the antinode in a rapid “burst” as described above, but then *falls back into an antinode* due to the action of friction and/or momentum diffusion. Such an event (an atom “skipping” between antinodes) would have cavity transmission contaminated by a brief episode of large-amplitude axial motion in the middle of the trajectory, causing our algorithm to estimate  $\rho(t)$  wrongly during the “skipping.” In a survey of a simulated data set of 410 trapped-atom trajectories of more than one radial oscillation cycle, fifteen exhibited “skipping,” giving an  $\approx 4\%$  rate for this particular issue. I mention this rate here because it is rather different from (considerably smaller than) the likelihood for axial “skipping” in some other parameter regimes, as discussed more fully in [26].

#### 4.2.1 Note on Conservative Motion in Gaussian Potentials

As a point of reference when viewing these atomic trajectories, it is interesting to note some characteristics of perfectly conservative two-dimensional motion in the same effective potential. The potential, while not strictly analytic in form, is very closely fit by a Gaussian in  $\rho$ . Conservative motion in this cylindrically symmetric potential produces trajectories which are in general not closed. Closed trajectories do arise – trivially, for zero angular momentum or circular orbits, or for small-energy motion that samples only the harmonic portion of the potential.

### 4.3 Position Sensitivity Estimates

The trajectory reconstructions described above, with their validation and error estimates from comparison with simulations, correspond to an atomic position measurement with  $2 \mu\text{m}$  resolution achieved in a timescale of  $10 \mu\text{s}$ . This corresponds to a position sensitivity of  $\sim 20 \text{ nm}/\sqrt{\text{Hz}}$  [25, 19].

We may compare this with a quick estimate of sensitivity limits for our cavity and detection scheme (Figure 4.10). We begin by writing down a rough dependence of measured cavity transmission on the atomic radial position:  $d(\text{detected photons per}$

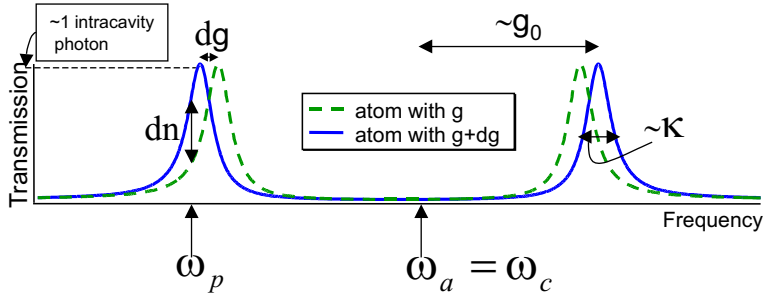


Figure 4.10: Sketch of vacuum Rabi splitting as the basis for position sensitivity estimates.

time)/ $d\rho = \eta 2\kappa \frac{dn}{dg} \frac{dg}{d\rho} = 2\eta \kappa \frac{1}{\kappa} \frac{g_0}{w_0} = 2\eta \frac{g_0}{w_0}$  ( $\eta$  is the overall detection efficiency and  $2\kappa$  is the overall cavity decay). Here we have approximated  $\frac{dn}{dg} \sim \frac{1}{\kappa}$  by reasoning that the intracavity photon number drops from  $\sim 1$  to  $\sim 0$  over the resonance feature width of  $\sim \kappa$ . Our result then implies that, as an atom moves over distance  $\Delta\rho$ , the corresponding signal (change in detected transmission) is  $2\eta \frac{g_0}{w_0} \Delta\rho$ .

To turn this into a sensitivity, we must ask how finely we can resolve a change in the number of detected photons per unit time. That is a question of how big the noise is relative to the signal. Overall there is roughly one photon in the cavity, giving a photon-detection rate of  $\eta(2\kappa)$ . Thus the shot noise is proportional to that value, i.e., shot noise for a given detection bandwidth  $B$  is  $\sqrt{2\eta\kappa B}$ . The signal-to-noise ratio in a given bandwidth  $B$  is  $\sim 2\eta \frac{g_0}{w_0} (\Delta\rho) / \sqrt{2\eta\kappa B}$ . Now if we define the sensitivity  $S_\rho$  as the  $\Delta\rho$  detectable with unit signal-to-noise, we have  $S_\rho \sim \sqrt{\frac{1}{2\eta}} \frac{w_0}{\sqrt{g_0^2/\kappa}} \sqrt{B}$ . Substituting the relevant experimental values, this analysis yields a position sensitivity limit of  $\sim 1.0 \text{ nm}/\sqrt{\text{Hz}}$ . The discrepancy between this quantity and the measured sensitivity can be somewhat attributed to technical noise – since technical noise is comparable to the shot noise it should degrade the signal-to-noise and thus the sensitivity by a factor of  $\sqrt{2}$  or so. That still leaves a very large gap, partially to do with the crude estimates of the physics going on. The fact of the matter is that there is excellent sensitivity on the side of the cavity mode ( $\rho \sim w_0/2$ ) and rather poor sensitivity on-axis ( $\rho \ll w_0$ ) and at the edges ( $\rho \gg w_0$ ), while we average over everything. Furthermore, our detection method falls short of realizing a full  $g_0^2/\kappa$  information rate for sensing an atom in the cavity, as discussed more fully in Chapter 7.

To predict a sensitivity for the as-yet unobserved axial motion, we may replace  $w_0$  with  $\lambda/4$ , the axial distance from field node to antinode, in the estimates above. This yields a limit of  $0.015 \text{ nm}/\sqrt{\text{Hz}}$  in principle, or an extrapolated sensitivity of  $0.3 \text{ nm}/\sqrt{\text{Hz}}$  based on what we achieve in the transverse direction. However, the increased sensitivity in the axial direction is offset somewhat in usefulness by the correspondingly faster timescale for axial motion, meaning that to resolve the motion on relevant dynamical timescales a higher measurement bandwidth must be employed.

From the point of view of quantum measurement and feedback schemes, it is of considerable interest to compare our position sensitivity with the limits imposed by the Heisenberg uncertainty principle – or, for quasi-continuous weak measurements such as ours, the standard quantum limit. Following the analysis of [82] for broadband position observation on a free particle, we estimate the time  $t_*$  for backaction effects to become discernible in the measurement record. Taking our radial sensitivity of  $2 \mu\text{m}$  over  $10\mu\text{s}$ , the walk-off time is  $t_* \approx 1.5 \text{ ms}$ . This means we could just begin to see the effect in the longest transits, while the mean dwell time puts us about a factor of five from the standard quantum limit.

One caveat in this analysis is the application of the free-particle theory to this case in which the atom is in fact trapped; certainly another important consideration in discussing the quantum nature of the atomic motion will be the vibrational quantization of atomic motion in the trap. In the current experiments, quantization is irrelevant in the radial dimension, where the vibrational frequency is 9.4 kHz compared to typical energies of 9.8 MHz. However, in the tightly-bound axial direction the vibrational levels are spaced by 0.7 MHz, which begins to be comparable to the typical axial energy of about 3 MHz during most of a trapped atom’s lifetime.

Improved signal-to-noise is undoubtedly desirable for developing “atom-cavity microscopy” and exploring quantum measurement limits. One opportunity for improved sensing would be to incorporate full detection of the cavity output field, i.e., amplitude and phase of  $\langle a \rangle$  rather than the  $|\langle a \rangle|^2$  measurement we now perform. Such full detection has been implemented in a cavity QED setting in [47], where atom-transit “phasors” were observed. In that work the ability to access phase-shift information

for the cavity field opened up the possibility for high signal-to-noise observations in a farther-detuned regime. Besides that possibility, full detection in our scenario would enhance signal-to-noise for observations of atoms passing very close to optimal coupling, with  $g(\vec{r}) \approx g_0$ .

## 4.4 Why Do Reconstructions Work in *This Parameter Regime?*

In this section we examine more closely the trapping potential and momentum diffusion of the triggered-trapping experiment. This analysis, largely presented in [26], was originally motivated by a desire to understand two aspects of our experiment. First, to what extent was it important that the trapping was a “binding” between a single atom and a single photon rather than an optical dipole force trap for a single atom with a classical light field? Second, how could we characterize the dynamics that made the motion of our trapped atoms quasi-conservative (and thus allowed trajectory reconstructions), especially considering the very different trapped-atom dynamics in a conceptually similar experiment (Pinkse *et al.*, [50])? I present this material here largely because it helps to characterize the dynamical regime that allows trajectory reconstructions, thus filling out the discussion of Section 4.2. Furthermore, the qualitative nature of the dynamics as reflected in the potentials and heating rates provides a relatively simple way of predicting conservative vs. diffusive trap dynamics in other parameter regimes; this is a useful tool in evaluating dynamics for different optical cavities, as discussed here and in Chapter 7.

To begin with we elucidate the quantum vs. classical nature of the trapping potential and momentum diffusion. In particular we find that, for the parameters of the atom-cavity microscope [25], the trapping potential and momentum diffusion have a quite different character from what would be expected of an equally deep standing-wave trap in free space. The usual (semiclassical) fluctuations of the dipole force along the standing wave are suppressed by an order of magnitude, which represents qual-

tatively new physics for optical forces at the single-photon level within the context of cavity QED. In the parameter regime of Pinkse *et al.* [50], still in the strong-coupling limit but with larger critical parameters ( $m_0, N_0$ ), the situation is rather different. The cavity and atom in this experiment had  $(g_0, \kappa, \gamma_{\perp})/2\pi = (16, 1.4, 3)$  MHz. For these parameters, even when the atom-cavity system is strongly coupled and driven such that it has a mean intracavity photon number of roughly one, the trapping potential and momentum diffusion are only slightly different from those in a free-space standing wave. We show that in the parameter regime of [50] the heating rates are such that the atom could be expected to gain energy equal to a significant fraction of the total trapping potential during a single motional oscillation period for both axial and radial motion. By this measure the heating rates in the atom-cavity microscope are very much slower, indicating more nearly conservative motion, and this could be expected to have a profound effect on the qualitative nature of the dynamics in the two experiments.

Ref. [26] also presents simulated transits for both experiments, and discusses the qualitative features of atomic dynamics in both cases. For the parameter regime of the atom-cavity microscope, conservative radial motion dominates diffusion and standing-wave motion, with atomic trajectories localized at peaks of a single standing-wave antinode. Atoms trapped with the mean trapping time execute several radial orbits. The eventual escape is typically due to heating along the cavity axis. By contrast, for the experiment of [50], a trajectory of typical duration does not experience a complete radial orbit and in fact resembles a scattering event, with a large contribution from radial diffusion as well. For these events the observed localization time is comparable to the time for free flight through the cavity. Axially the simulations show that in longer-duration transits the atom frequently skips between wells of the standing-wave potential due to repeated heating and recooling.

#### 4.4.1 Quasi-classical Model for Atomic Motion in the Cavity

The atom-cavity system is modeled by a quasi-classical treatment presented in [26, 83]; the term *quasi-classical* is used to distinguish this approximation from the usual *semiclassical* treatment which neglects the full quantum nature of the cavity field. Here, the atomic internal states and cavity field are treated with their full quantum character retained. The atomic motion is treated in a quasi-classical approximation which requires the spread of its wavepacket in both position and momentum space to be small compared to relevant scales in the problem. Specifically, an atom must be localized to much better than an optical wavelength of the atom or cavity resonance frequencies. This is equivalent to the requirement that the momentum spread be large compared to an individual momentum kick associated with spontaneous emission or exchange of excitation with the cavity field. At the same time, however, an upper bound on momentum spread (or equivalently lower bound on position spread) must be satisfied. This bound arises by considering the Doppler shifts of relevant fields as seen by the atom; Doppler shifts due to the momentum spread must be small relative to atom and cavity linewidths. The consistency of these conditions and their application to the atom-cavity system rely on a separation of timescales between atomic motion and atom-cavity internal dynamics; this separation is easily satisfied for motion in the radial direction, and still applicable though approaching its limit for motion in the axial dimension. Under these conditions we may calculate all quantities of interest in the system by referring to steady-state solutions of the master equation (Equations 2.6-2.7) for each atomic position  $\vec{r}$ .

The treatment outlined above and fully set forth in [26, 83] can give us a great deal of information about the nature of the dynamics that may be expected in the parameter regimes relevant to the atom-cavity microscope and to [50]. In particular we are interested in whether quantization of the cavity field leads to any significant change in the dynamics, in the sense of asking whether the atomic motion is very different in the cavity from what it would be in a free-space standing wave of the same intensity and geometry as the cavity mode. Secondly, we can investigate the nature

of the resulting atomic motion in the cavity field, which can be either predominantly conservative or significantly diffusive and dissipative, depending on the particular parameters of interest.

To get a feel for the type of atom dynamics expected, effective potentials and heating rates were calculated for both the axial and the radial directions of motion. Friction coefficients may also be calculated, but we omit them in this discussion because their contribution to the motion is much smaller than that of momentum diffusion in the atom-cavity microscope. The force operator is given by

$$\hat{\vec{F}}(\vec{r}) = -\hbar \vec{\nabla} g(\vec{r})(\hat{a}^\dagger \hat{\sigma} + \hat{a} \hat{\sigma}^\dagger) = -\hbar g_0 \vec{\nabla} \psi(\vec{r})(\hat{a}^\dagger \hat{\sigma} + \hat{a} \hat{\sigma}^\dagger). \quad (4.3)$$

The effective potential for the atom in the cavity field may be calculated from the force by

$$U_{eff}(\vec{r}) = - \int_0^{\vec{r}} \langle \hat{\vec{F}}(\vec{r}') \rangle \cdot d\vec{r}'. \quad (4.4)$$

The heating rates represent the average increase in the motional energy due to the momentum diffusion at a given position  $\vec{r}$  and may be calculated from the diffusion tensor according to

$$\frac{dE}{dt}(\vec{r}) = \text{Tr}[\mathbf{D}(\vec{r})]/m, \quad (4.5)$$

where  $m$  is the atomic mass. The total momentum diffusion tensor  $\mathbf{D}$  has two distinct contributions  $D$  and  $E$ . The first contribution arises intuitively from decays and re-excitations which switch the system stochastically between the trapping potential of the strong-field seeking state and the flat potential of the overall ground state. This contribution to momentum diffusion is given by

$$D_{ij} = \int_0^\infty d\tau \left[ \frac{1}{2} \langle \hat{F}_i(\tau) \hat{F}_j(0) + \hat{F}_i(0) \hat{F}_j(\tau) \rangle - \langle \hat{F}_i \rangle \langle \hat{F}_j \rangle \right]. \quad (4.6)$$

(Recall that the time dependence of  $\hat{F}$  arises because we are in the interaction picture with respect to the probe frequency  $\omega_p$ .) The other contribution to momentum diffusion comes simply from momentum kicks associated with atomic spontaneous

emission, and is given by

$$E_{ij} = \varepsilon_{ij} \hbar^2 (2\pi/\lambda)^2 \gamma_{\perp} \langle \hat{\sigma}^\dagger \hat{\sigma} \rangle. \quad (4.7)$$

Here  $\varepsilon$  describes the usual dipole distribution of atomic spontaneous emission and is diagonal, with  $\varepsilon_{xx} = \frac{2}{5}$  and  $\varepsilon_{yy} = \varepsilon_{zz} = \frac{3}{10}$ .

Since  $g(\vec{r}) = g(\rho, x)$ , we neglect the  $\theta$  coordinate for the time being and write the potentials and diffusions as functions of position  $(\rho, x)$ .

#### 4.4.2 Potentials and Heating Rates for Atomic Motion

Gathering up the results – and notation – of the preceding discussion, we see for example that the axial potential at the center of the Gaussian mode is  $U_{eff}(0, x) = - \int_0^x \langle \hat{\vec{F}}(0, x') \rangle dx'$  and the associated axial heating rate is  $dE(0, x)/dt = \mathbf{D}_{xx}(0, x)/m$ . These quantities along with their radial equivalents  $U_{eff}(\rho, 0)$  and  $dE(\rho, 0)/dt$  are plotted in the solid traces of Figure 4.11 for the parameters of the atom-cavity microscope. The force and momentum diffusion coefficient for the cavity system were calculated according to the formulae described above by numerical techniques based on [34, 83]. The field state is expanded in terms of number states and truncated at an appropriate level and a matrix continued fraction algorithm is used to calculate  $D$ . The axial potentials and heating rates have  $\lambda/2 = 426$  nm periodicity inherited from the standing-wave field strength. Observe that the axial heating rates have minima at both field antinodes and field nodes.

The first thing to note is that the axial and radial heating rates are very different from one another. In the radial direction, heating is dominated by diffusion due to spontaneous-emission recoils. Axially, however, the reactive or dipole fluctuation component of the diffusion dominates. This is because the reactive component is proportional to the gradient of the field squared, which is much larger for the axial direction where variations are greater (by a factor of  $2\pi w_0/\lambda$ ). This contribution also has the property that it does not saturate with the atomic response.

It is already clear that it should be possible to trap individual atoms, since the

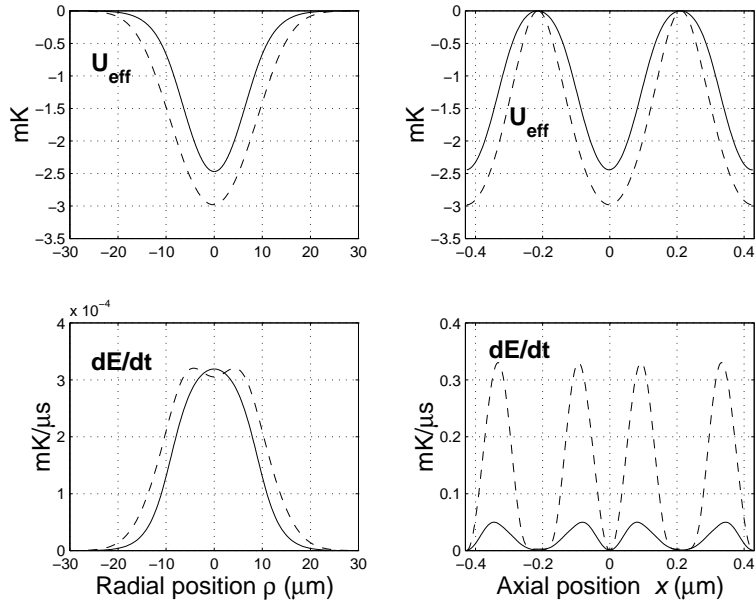


Figure 4.11: Effective potentials and heating rates for the ACM parameters, with  $(g_0, \kappa, \gamma_\perp)/2\pi = (110, 14.2, 2.6)$  MHz. Detunings are  $(\Delta_{pa}, \Delta_{ca})/2\pi = (-125, -47)$  MHz and the drive strength corresponds to 0.3 photons in the empty cavity. The quantum prediction is shown by solid lines, with the semiclassical prediction given in dashed lines.

potential depth of roughly 2.5 mK is greater than the initial energy of the atoms in the experiment (around 0.46 mK) and the heating rate in the radial potential is relatively slow. Over  $50 \mu\text{s}$  (a timescale over which the atomic motion is strongly affected by the potential) the total heating will typically still be small compared to the depth of the potential. However, the importance of the quantum character of the relevant fields or phenomena is not ensured by the statement that trapping occurs with mean field strength of about one photon, since this is trivially the case in an equivalent free-space volume for a field of the same intensity as that inside the cavity. Just as in the cavity, a free-space field at  $\omega_p < \omega_a$  creates an attractive potential which leads to the well-known red-detuned dipole trap for neutral atoms (see, e.g., [32]); whether the intracavity trap differs in any recognizable way from its simple free-space cousin is not immediately clear.

In order to see whether a full quantum description of the atom-cavity is necessary in order explain observed effects, Figure 4.11 also shows the values calculated for an

atom in an equivalent free-space standing wave, calculated by standard techniques [84]. This free-space standing wave has the same geometry as the cavity mode and the same peak field strength  $g_0|\langle a \rangle|^2(0, 0)$ . The detuning between the free-space field and the atom is chosen to be  $\Delta_{pa}$ . Perhaps surprisingly, the only large difference between the two models is in the axial heating rate, where a strong suppression of the axial heating is seen in the quantum calculation. This suppression is an effect of the quantized nature of the intracavity field. The self-consistent coupling of the cavity field and atomic position (in a semiclassical sense) cannot explain this suppression; in fact, by itself this coupling would lead to an increase in diffusion over the free-space case, since the atomic motion within the cavity induces steeper gradients in the field. The suppression of diffusion is then evidence that it is necessary to use a fully quantum description, and speak of single photons rather than classical fields for these experimental parameters. As discussed in [25], this suppression of the axial heating was essential for the trapping of atoms in the cavity. Thus for these experimental parameters, the eigenvalue structure of Figure 2.5 leads to profound differences between the standard theory of laser cooling and trapping and the extension of this theory to the regime of strong coupling in cavity QED.

By way of comparison, the same quantities are plotted for the parameters relevant to Pinkse *et al.* [50] in Figure 4.12. The smaller value of  $g_0$  in this experiment leads to a smaller effective potential, since the spatial gradients of the dressed state energy levels (which lead to the potential) are proportional to  $g_0$ . More importantly, the diffusion values calculated from the full quantum model discussed above are now little different from those of the equivalent free-space standing wave. This lack of a clear difference in potentials or diffusion indicates that the quantized nature of the field is not required to explain the radial trapping observed in [50]. Note that the resulting axial heating rates are essentially the same as those of Figure 4.11 in absolute magnitude; however, in the atom-cavity microscope the potential has been made deeper *without* the expected corresponding increase in diffusion. For the parameters of [50] one additional interesting feature appears – enhanced cooling of the atomic motion relative to the parameters of the atom-cavity microscope. This

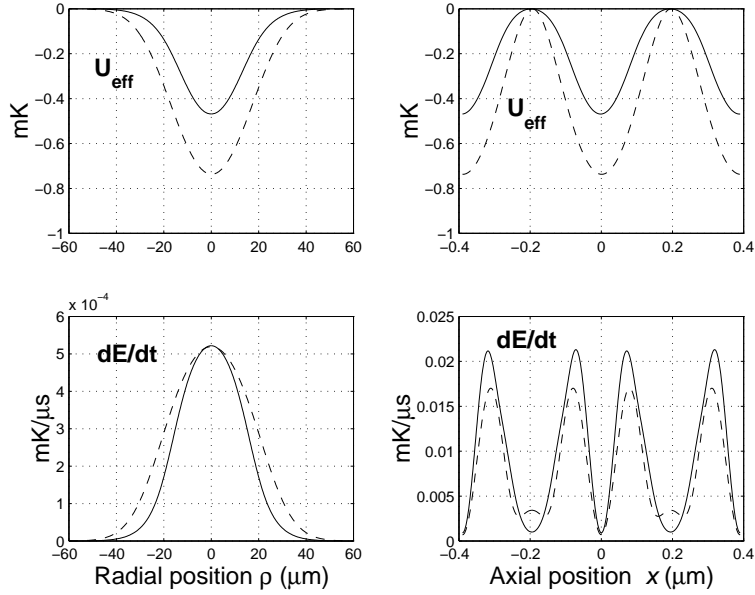


Figure 4.12: Effective potentials and heating rates in a less conservative parameter regime. Here  $(g_0, \kappa, \gamma_{\perp})/2\pi = (16, 1.4, 3)$  MHz. Detunings are  $(\Delta_{pa}, \Delta_{ca})/2\pi = (-40, -35)$  MHz, and the drive strength corresponds to 0.9 photons in the empty cavity. Solid lines are the quantum prediction while dashed lines are the result of the semiclassical calculation. Note that axial quantities here have a periodicity of 390 nm, since this experiment used Rubidium atoms with a resonant transition at 780 nm.

arises through cavity-mediated cooling [85, 86], and has an important effect on the axial dynamics of atoms in the experiment of [50].

We now wish to use these potentials and heating rates to gain an intuitive understanding of the character of atomic motion that we would expect to observe in each case. In particular, we are interested in exploring the degree to which the atomic motion in the potential can be close to conservative motion, or likewise the degree to which it could be dominated by diffusion.

The timescales of relevance to the conservative motion may be characterized by the period associated with small-amplitude oscillations in the bottom of the axial ( $\tau_a = 1/\nu_a$ ) and radial ( $\tau_r = 1/\nu_r$ ) potential wells. If the energy changes only by a small fraction of the total well depth  $U_0$  over this timescale, motion will be nearly conservative. Figure 4.13 plots the potentials and heating rates for the two cases in this new set of scaled units; heating rates are expressed as an energy increase per

oscillation period, as a fraction of  $U_0$  (note as the atom heats and explores the anharmonicity of the potential, the period of oscillation only lengthens). Interestingly, we see a clear qualitative difference in the nature of the atomic motional dynamics. For the parameters of the atom-cavity microscope (solid lines), in the radial plane spontaneous emission gives only small perturbations to the energy over the timescale of single orbits, and motion is nearly conservative. We note that this low level of diffusion enabled the reconstructions of single atom trajectories presented earlier in this chapter, for which the small changes in angular momentum could be accurately tracked. A quite different regime is found for the parameters of [50] (dash-dotted lines), where the radial atomic motion is strongly affected by heating from spontaneous emission kicks. Here an average atom gains an energy of nearly half the well depth in what would be a radial orbit time, adding a large diffusive component to the motion. This same scaling shows that the axial heating rate is also much more rapid on the scale of the potential in [50], which suggests that the atom will more quickly escape its confinement near an antinode and begin to skip along the standing wave. The qualitative understanding of the atomic motion gained here is borne out by the results of [25] and [50], and is explored in more detail in the simulations of [26].

From comparison of Figure 4.13 with simulated dynamics in [26], we arrive at a means for predicting the conservative or diffusive nature of single-photon trapping for atoms in varying parameter regimes. For example, I have calculated effective potentials and diffusion rates for a hypothetical triggered-trapping experiment in the cavity currently used in the other cavity QED lab in our group. This cavity has  $(g_0, \kappa)/2\pi = (32, 4)$  MHz and a mode waist of  $w_0 = 23.8 \mu\text{m}$ . The corresponding critical atom and photon numbers are  $(N_0, m_0) = (2.0 \cdot 10^{-2}, 3.3 \cdot 10^{-2})$ . For comparison, the atom-cavity microscope parameters were  $(g_0, \kappa)/2\pi = (110, 14.2)$  MHz, giving  $(N_0, m_0) = (6.1 \cdot 10^{-3}, 2.8 \cdot 10^{-4})$ , with a mode waist of  $w_0 = 14.1 \mu\text{m}$ .

I approximated the atom-cavity microscope conditions by keeping the cavity-atom detuning  $\Delta_{ca}$  constant relative to  $g_0$  and placing the probe a fixed fraction of  $\kappa$  inside (to the blue of) the lower dressed state resonance. Thus for the longer cavity (and smaller  $g_0, \kappa$ ) I set  $(\Delta_{pa}, \Delta_{ca})/2\pi = (-37, -14)$  MHz. To consider a single-photon

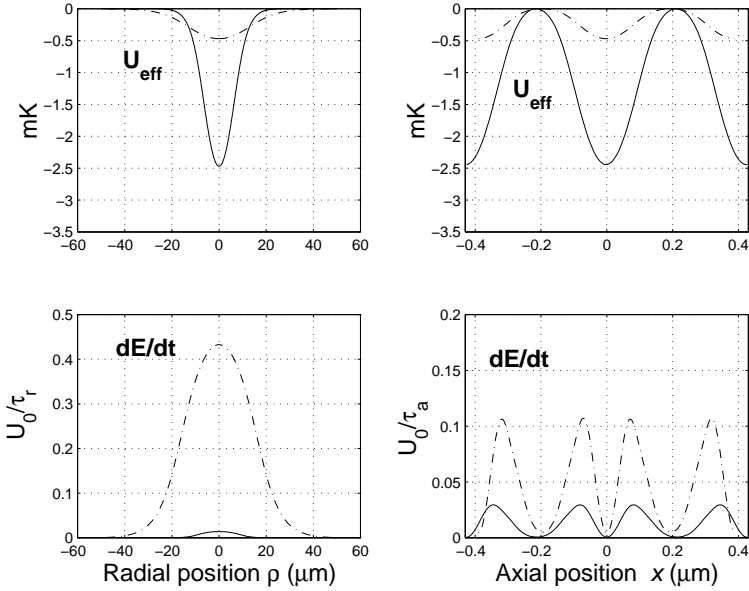


Figure 4.13: Heating per motional cycle measures conservative character of motion. Solid lines show the parameters of the atom-cavity microscope, while dash-dotted lines correspond to the situation of [50].

trapping experiment, I set a driving level of 0.3 photons in the empty cavity at this detuning. For this case I found an effective potential depth of  $U_0 = 0.57 \text{ mK}$ , with radial momentum diffusion giving a heating rate  $dE/dt = 0.21U_0/\tau_r$ . Axial motion was also characterized by higher momentum diffusion per motional cycle than we experienced in the atom-cavity microscope. Thus a single-atom, single-photon trapping experiment in this cavity would, not surprisingly, yield dynamics similar to those of [50] rather than to those of the atom-cavity microscope. Decreasing critical atom and photon numbers induces a transition from atom-cavity scattering experiments to largely conservative atom-cavity binding; in this sense the atom-cavity microscope could as well be termed the atom-cavity molecule.

## Chapter 5

# Active Feedback on Atomic Position: Towards a Quantum Servo

The atom-cavity microscope, as described in the preceding two chapters, demonstrates the ability to trap a single atom in an optical cavity and monitor its position in real time. Current experimental efforts in our group and elsewhere (see [87]) focus on the use of this real-time position information to feed back to actively control atomic positions within the cavity mode. Progress in this direction aims to use cavity QED to investigate fundamental questions of quantum measurement and optimal state estimation and control (see, e.g., [88, 89, 90]). The ability to trap an atom with a single photon field is a dramatic illustration of single-quantum physics in optical cavities; however, it is the sensing power and signal-to-noise for real-time observation of the system that makes the optical cavity unique. This chapter discusses feedback strategies and simulations of their performance for experimentally relevant parameters.

The cavity enhancement of sensing was illustrated in dramatic fashion by the two-dimensional trajectory reconstructions of the previous chapter. However, the initial goal of our feedback algorithms will be to control  $\rho(t)$ ; for this purpose it is sensible to ignore  $\theta(t)$  for the time being and apply all available signal-to-noise to the task of estimating  $\rho(t)$  and  $\dot{\rho}(t)$  in real time. The goal of such a program is then to use this information to drive  $\rho(t)$  to a constant value, or in other words to circularize an orbit

in the  $(\rho, \theta)$  plane while not necessarily driving it to the cavity axis ( $\rho = 0$ ). The latter task, which requires an explicit method of breaking cylindrical symmetry for position sensing and for the effective potential, can be considered as a later extension.

## 5.1 The Atom and Cavity as a Control System: Basic Feedback Strategy

As a guide in the identification of plausible feedback strategies and their limitations, it is useful to restate the problem somewhat in the language of control systems. To this end, we begin by setting aside the issue of axial motion and treating the atom as a particle in a cylindrically symmetric, approximately Gaussian two-dimensional potential whose depth is controlled by the input light intensity:

$$U \approx -U_0 e^{-\rho^2/w^2}. \quad (5.1)$$

Note that the potential waist  $w$  is not simply equated with the previously introduced cavity field waist  $w_0$  or with the mode intensity waist  $w_0/\sqrt{2}$ , but rather is set by the self-consistent interaction of atom and light field in the strong coupling regime. Where the cavity mode profile is exactly Gaussian,  $U$  is only approximately Gaussian and has an exact form that is nonanalytical as determined by steady-state solutions to the master equation for an atom at each value of  $\rho$ . The potential depth  $U_0$  depends on the intensity of the optical field used to drive the cavity mode. The potential waist  $w$  is in fact a (slowly varying) function of the drive strength as well.

The trapped atom is also subject to dynamical noise in the form of friction and momentum diffusion arising from decays and re-excitations of the system on timescales faster than the motion. In the regime of Ref. [25], the contribution of friction is small compared to the momentum diffusion terms in the equation of motion.

Because the two-dimensional potential is cylindrically symmetric, the atom's angular momentum  $L$  is constant, or rather, varies only due to dynamical noise. We

can thus write a one-dimensional effective potential in the  $\rho$  dimension,

$$V_{eff} = -U_0 e^{-\rho^2/w^2} + L^2/2m\rho^2 \quad (5.2)$$

and thus an equation of motion (for an atom of mass  $m$ )

$$\ddot{\rho} = -\frac{2\rho U_0}{mw^2} e^{-\rho^2/w^2} + \frac{L^2}{m^2 \rho^3} \quad (5.3)$$

which we notationally simplify to the form

$$\ddot{\tilde{\rho}} = -\tilde{\rho} E e^{-\tilde{\rho}^2} + \frac{\tilde{L}}{\tilde{\rho}^3} \quad (5.4)$$

where  $\tilde{\rho}$  is dimensionless ( $\tilde{\rho} = \rho/w$ ),  $E = 2U_0/mw^2$  is the input we control by varying the driving field strength, and  $\tilde{L} = L^2/m^2 w^4$  is constant except for the influence of dynamical noise.

The measurement of light transmitted through the cavity,  $T(t)$ , is equivalent to a (noisy) measurement of  $\rho(t)$ . The noise of this measurement is largely fundamental quantum noise (shot noise) of detection. The mapping between  $T$  and  $\rho$ , derived again from steady-state solutions of the master equation for the coupled atom-cavity system, is not linear and furthermore depends on the value of the driving strength  $E$ . The initial objective is to circularize the two-dimensional orbit – in other words, to make  $\rho$  constant or to hold  $\dot{\rho} = 0$  by varying the control input  $E$ .

The simplified system can be described by a block diagram as shown in Figure 5.1. The system exhibits myriad nonlinearities; for example,  $(T \rightarrow \rho)$  is nonlinear and depends on  $E$ , the dynamical noise depends on  $E$ , and the equation of motion for  $\rho$  is itself nonlinear. Nonetheless, while this statement of the problem does not suggest provably optimal feedback strategies, it does motivate some conceptually simple algorithms based on switching between discrete values of driving strength  $E$ . Switching strategies of this sort are often invoked for the sake of robustness, a major consideration in this scenario; robustness to dynamical and measurement noise is certainly important, but perhaps even more relevant is robustness to small uncertainties in sys-

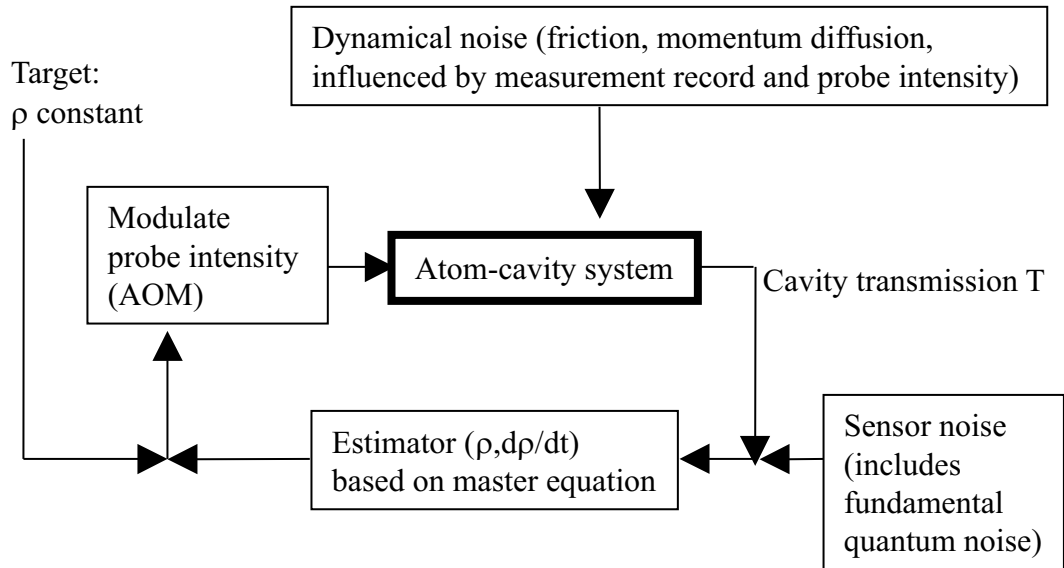


Figure 5.1: Block diagram for the atomic position feedback loop, illustrating sources of noise and system nonlinearities.

tem parameters (e.g., driving strengths or detunings). Switching or “bang-bang” type algorithms have the additional virtue of admitting easy implementation in simulations and in experimental design.

### 5.1.1 General Feedback Strategy

The feedback algorithms we investigate in this chapter all share the same basic strategy of switching the driving field intensity between two discrete levels. This corresponds to switching between two potential depths (and, incidentally, two different sets of friction and momentum diffusion coefficients as well). The simple objective is to time this switching relative to the atomic motion so that an atom sees a steep potential when climbing out of the trap ( $\dot{\rho} > 0$ ) and a shallow potential when falling back towards the trap center ( $\dot{\rho} < 0$ ), as illustrated in Figure 5.2. The feedback algorithm, then, is based on switching the potential at turning points of  $\rho$ , i.e., each time  $\dot{\rho}$  crosses zero. Implemented effectively, this approach promises significant dynamical cooling of the radial motion ( $\rho \rightarrow \text{constant}$  or  $\dot{\rho} \rightarrow 0$ ) in just a few oscillations.

The initial detection and trapping of an atom are accomplished as in Chapter 4 and [25, 26]; a weak probe at driving level  $exlo$  is used to detect the atom’s arrival in

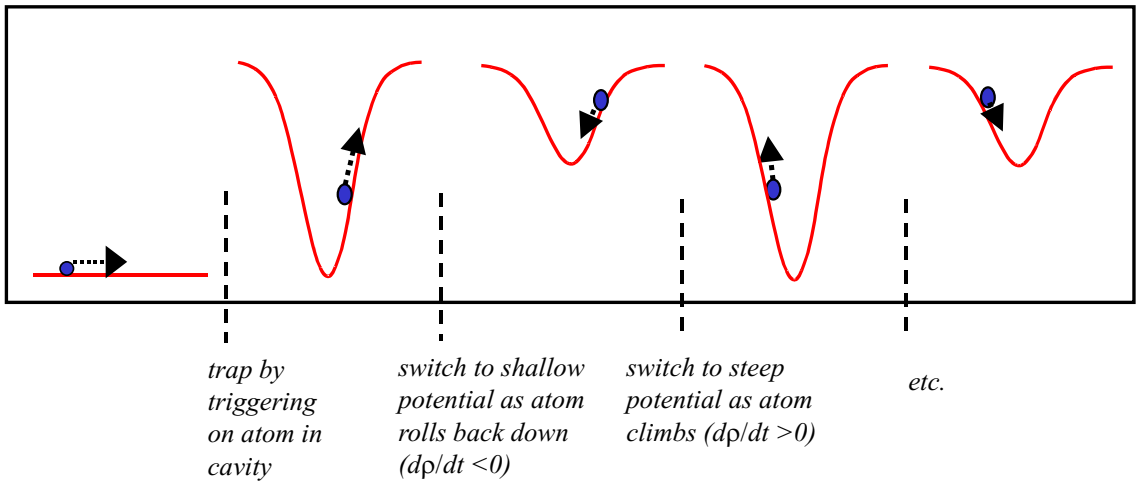


Figure 5.2: General feedback strategy for atomic radial coordinate

the cavity with minimal effect on the motion, and an increase in transmission of this beam triggers a switch to driving level  $hi$  to populate strong-field-seeking states and trap the atom. Feedback is then implemented by switching the trapping potential between the  $hi$  level and an intermediate  $lo$  setting, with switching times based on real-time information about the motion of the single atom.

The simplest algorithm would be to switch back and forth between  $hi$  and  $lo$  potentials at the turning points of  $\rho(t)$ , which are the zero-crossings of  $\dot{\rho}(t)$ . That is, trap initially in  $hi$ , switch to  $lo$  when  $\dot{\rho}$  crosses zero from above (i.e., when  $\rho$  begins to decrease), switch back to  $hi$  when  $\dot{\rho}$  crosses zero from below ( $\rho$  reaching its minimum and increasing), and so on until the atom escapes. However, this strategy calls for a theoretically infinite sequence of switching events, while it is desirable to instead achieve a steady state in some large-time limit. The presence of dynamical noise implies that the exact steady state of  $\dot{\rho} \rightarrow 0$  is in any case unreachable, so we replace it with a goal of confining  $\dot{\rho}$  to some range  $[-lim, +lim]$ . Thus the feedback strategy is modified to include slight hysteresis:  $hi \rightarrow lo$  when  $\dot{\rho} \rightarrow -lim$  from above,  $lo \rightarrow hi$  when  $\dot{\rho} \rightarrow +lim$  from below. With this modification, switching stops once  $\dot{\rho}$  is confined within the acceptable range. Furthermore, we prefer a steady state with  $hi$  potential because of the deeper confinement. To bias the system towards this final state, we use asymmetric hysteresis limits:  $lo \rightarrow hi$  when  $\dot{\rho} \rightarrow +lim$  from below,  $hi \rightarrow lo$

when  $\dot{\rho} \rightarrow -(lim + \delta)$  from above.

## 5.2 Simulations of Feedback Algorithms in Operation

For our simulations, we have chosen cavity parameters as well as driving strengths and detunings based on Ref. [25], with  $\Delta_{ca} = -47$  MHz,  $\Delta_{pa} = -125$  MHz,  $n_{exlo} = 0.05$  photons in the empty cavity,  $n_{hi} = 0.3$  photons in the empty cavity, and  $n_{lo} = 0.15$  empty-cavity photons. These driving strengths are chosen to be high enough so that an atom of typical kinetic energy can be trapped by both *lo* and *hi* drives, yet low enough to ensure the increase in momentum diffusion between *lo* and *hi* does not outstrip the increase in potential depth.

Our simulations of the atom-cavity dynamics are based on the treatment outlined in Section 4.4.1 and described in detail in Ref. [26, 83]; the treatment is fully quantized for the atomic internal state and the cavity light field, but considers the atomic center-of-mass motion quasi-classically. This approximation is suitable for the current experimental situation, with more manifestly quantized motion to be accessed by better cooling and/or detection of the atom’s axial motion. The dynamical noise of the system, in the form of friction and momentum diffusion, is included in the simulation; the resulting “heterodyne transmission” trace is a perfect record of  $|\langle a \rangle|^2$ , on which measurement bandwidths and shot noise must be imposed separately. Shot noise is modelled as Gaussian white noise with an amplitude that depends on the size of the (noiseless) transmission signal.

In the presence of sensor noise, we require estimators for the quantities  $\rho$  and  $\dot{\rho}$ . Because one parameter ( $L$ ) in the equation of motion is unknown and in fact slowly varying, we have chosen not to implement estimators based on a Kalman-filter approach [91]. More sophisticated treatments include Kalman-type approaches to simultaneously estimate  $\rho$ ,  $\dot{\rho}$ , and  $L$  [92], but these have not been explored in full detail. Possible approaches include various methods such as the extended Kalman filter

or unscented Kalman filter; for an introduction and overview, see [93]. Meanwhile, we choose to estimate  $\rho(t)$  and  $\dot{\rho}(t)$  directly from the measurement record, with no explicit reference to the equation of motion for the system.

The noisy transmission signal  $T$  is sampled at 1 MHz as mentioned above. Digitization of the signal at finite resolution can introduce noise, so the resolution of this step should be kept small relative to pre-existing noise amplitudes. To estimate  $\rho$ , we first perform an RC low-pass filter on  $T$  at 100 kHz. This step is an infinite impulse response (IIR) filter which consequently introduces only a small delay in the estimator. This filtered transmission signal is then put through a lookup table with linear interpolation to obtain  $\rho_{est}(t)$ .

The resulting  $\rho_{est}(t)$  tracks the actual  $\rho$  closely but still with significant noise. Obtaining a time derivative without excessive noise thus requires some care. A variety of methods are mentioned in Ref. [94], in which the authors are concerned with estimating the sign of a time derivative in order to feed back to a system – essentially the same problem we encounter. We employ a simple finite impulse response (FIR) filter that takes the slope of a linear least squares fit to  $\rho_{est}(t)$  over a window of fixed size. A detailed implementation of this filter is found in Ref. [95]. The resulting  $\dot{\rho}_{est}(t)$  is a good estimator for  $\dot{\rho}$  at the middle of the window, so the delay induced is approximately half the window size. We find that a window size of 30 to 40  $\mu s$  gives a signal  $\dot{\rho}_{est}(t)$  which is quiet enough for use in our control. Thus reliable estimation in the presence of noise introduces a delay of approximately 15 to 20  $\mu s$  in the feedback loop. This time delay can be compared to a typical atomic orbital period of  $\tau_r \sim 100 \mu s$ , corresponding to a period of  $\sim 50 \mu s$  for  $\rho$ . Feeding back effectively in the presence of such large delays requires a certain amount of adjustment to the naive cooling algorithm of Section 5.1.1, as discussed in detail below.

### 5.2.1 Actual Dynamics But No Measurement Noise

Before treating the case of actual experimental noise, we explore the performance of our feedback strategy in simulations with noiseless measurement and thus per-

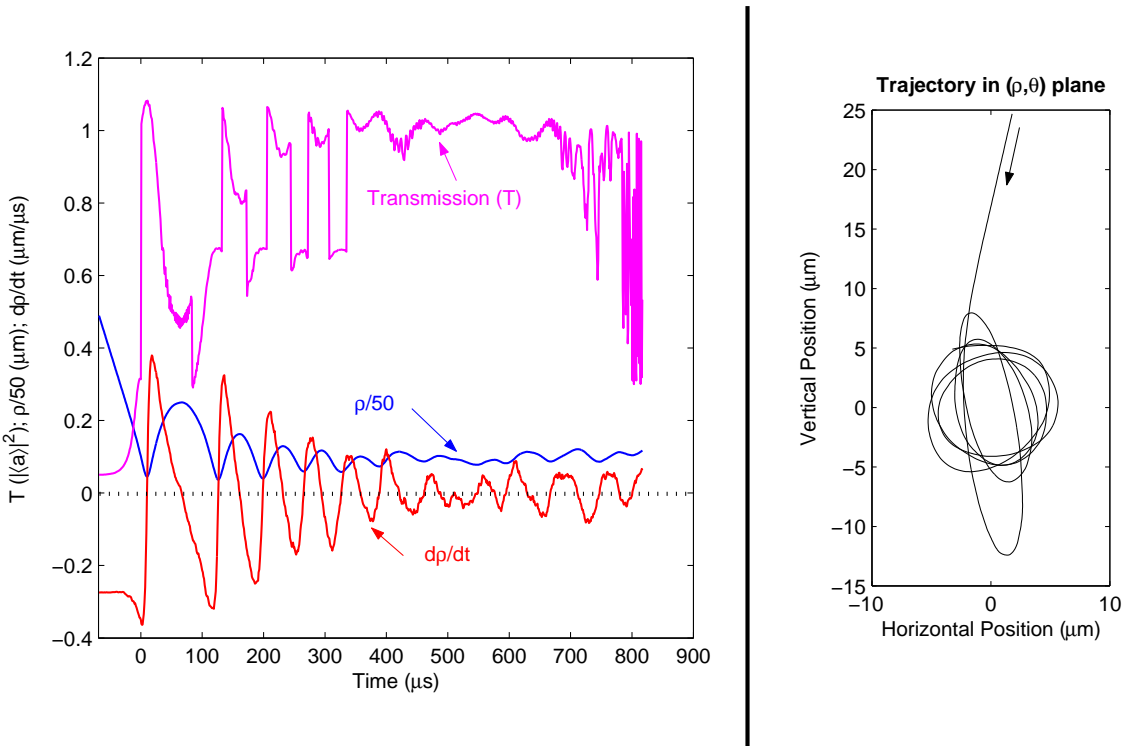


Figure 5.3: Simulated feedback example with perfect sensing of  $\rho(t)$ .

fect, zero-delay sensing of  $(\rho, \dot{\rho})$ . Figure 5.3 shows an example trajectory using this asymmetric-hysteresis switching strategy. The values of cavity transmission  $T$  and atomic position variables are sampled every  $1 \mu\text{s}$ , but the dynamical timestep is 3,000 times finer than this ‘‘information’’ timestep. Note that axial motion (the  $x$  direction our strategy neglects) is included in the simulation, and when its amplitude is large it gives rise to the very fast variations seen in  $T(t)$ . However, since the period of  $x$  motion is similar to the information timestep used, note that these signals are undersampled in the record.

A  $10 \mu\text{s}$  box filter is applied to  $\dot{\rho}$  in order to remove some oscillations caused by  $x$  motion and also partially to anticipate some effects of noisy detection and delay. In setting the conditions for potential-switching, we employ the asymmetric hysteresis described above, so the potential depth is switched at  $\dot{\rho} = +0.05, -0.08 \mu\text{m}/\mu\text{s}$ . Switching events, since they correspond to turning the light level up and down, can be seen as sharp edges in the transmitted light  $T$ . As the example illustrates, the control

strategy successfully circularizes atomic trajectories within a few orbital cycles. This can be seen from  $\rho(t)$  as well as from the trajectory shown in the  $(\rho, \theta)$  plane. The hysteresis limits are chosen so that variations in  $\rho$  due only to dynamical noise tend not to trigger any switching of the drive. This is illustrated by the continued high control level throughout the time  $t = 450 - 600 \mu\text{s}$ , while  $\rho$  is wandering diffusively rather than oscillating with regularity.

The overall trap lifetime is dominated, as in this example, by heating in the  $x$  direction. (In the example shown, note the fast, large-amplitude variation in transmission just before the atom escapes; this is a signature of rapid axial heating.) Thus our feedback strategy has little impact (at the level of 10%) on average trapping lifetimes. Circularizing the orbit helps decrease axial heating since the potential depth no longer wanders as  $\rho$  varies; however, the feedback is accomplished by sharp switching events which occur at arbitrary times relative to the oscillations in the  $x$  direction. The overall impact on lifetimes is therefore small in the simulations we have performed. Since the feedback algorithm is aimed at reducing motion in the  $\rho$  direction, its success is best measured by its performance at that task specifically. Lifetime effects can become apparent only if the axial motion is suppressed by some other means; that case is treated briefly in the final set of simulations presented in this chapter.

### 5.2.2 Adding Measurement Noise Adds Delays

The addition of measurement noise and consequent estimation of  $\dot{\rho}$  introduce significant loop delays, as described above. Since  $\dot{\rho}_{est}$  can be almost half a cycle behind the actual  $\dot{\rho}$ , we expect naive switching to be well out of phase with the atomic motion and thus relatively ineffective as a cooling mechanism. Figure 5.4 shows an example in which the feedback strategy is identical to that of Figure 5.3, but applied to  $\dot{\rho}_{est}$  rather than to  $\dot{\rho}$  itself. The resulting time delay seriously compromises performance, as shown. In the figure, note that the switching events, recognizable as sharp edges in transmission, do not line up with turning points of  $\rho$ . As a result,  $\dot{\rho}$  is not damped

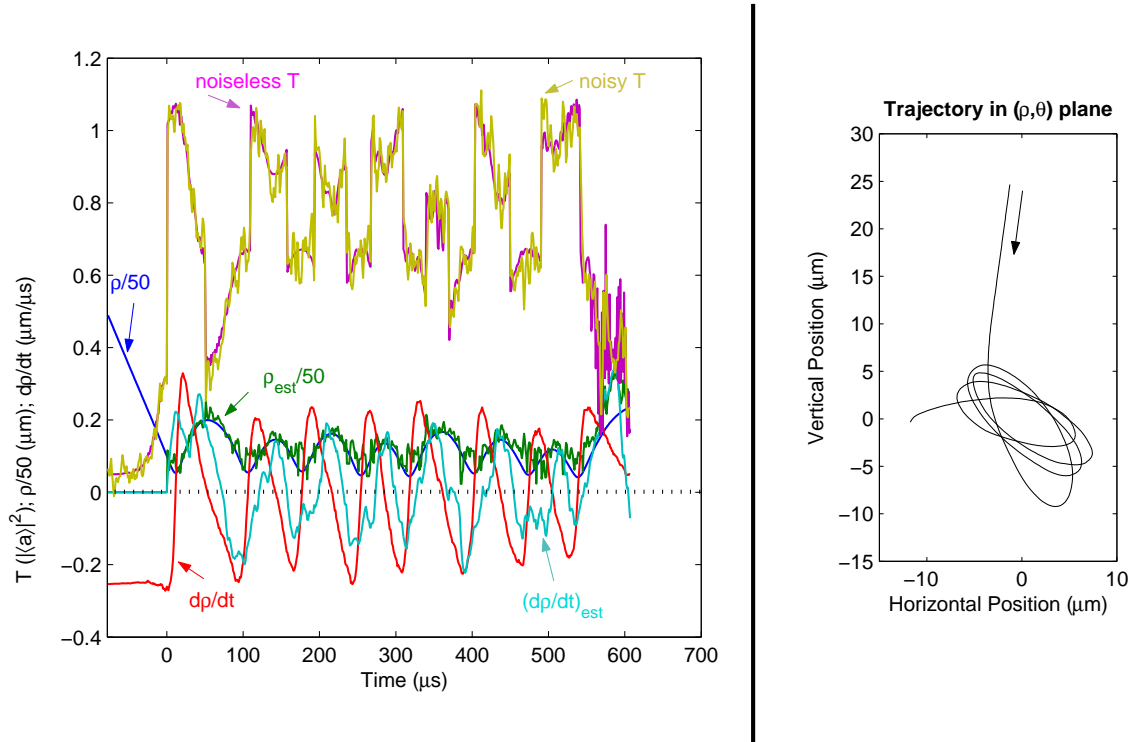


Figure 5.4: Measurement noise leads to filtering and unacceptable loop delay.

and the trajectory remains elliptical.

### 5.2.3 Account for Delays by Waiting a Cycle

Since it seems clear we cannot simply close the loop with the delays necessitated by measurement noise, we choose to address the problem by adding even more delay – that is, by detecting a switching condition ( $\dot{\rho}_{est}$  crossing a hysteresis limit) and then waiting to switch the potential at a time which should catch the *next* oscillation of  $\rho$ . A first attempt in this direction would be to assume a fixed period for oscillations of  $\rho$ . In this case the additional wait before switching is given by this fixed period minus the estimator delay for  $\dot{\rho}_{est}$ . Since each switching time is now set by the detected signal from the previous cycle, the first switching opportunity (first minimum of  $T$  and maximum of  $\rho$ ) will be missed in this strategy. Rather than miss this cooling cycle, we impose a single switching event a fixed time after the initial trap turn-on. Thus the potential switches *exlo*→*hi* on the initial trigger, *hi*→*lo* a fixed time later,

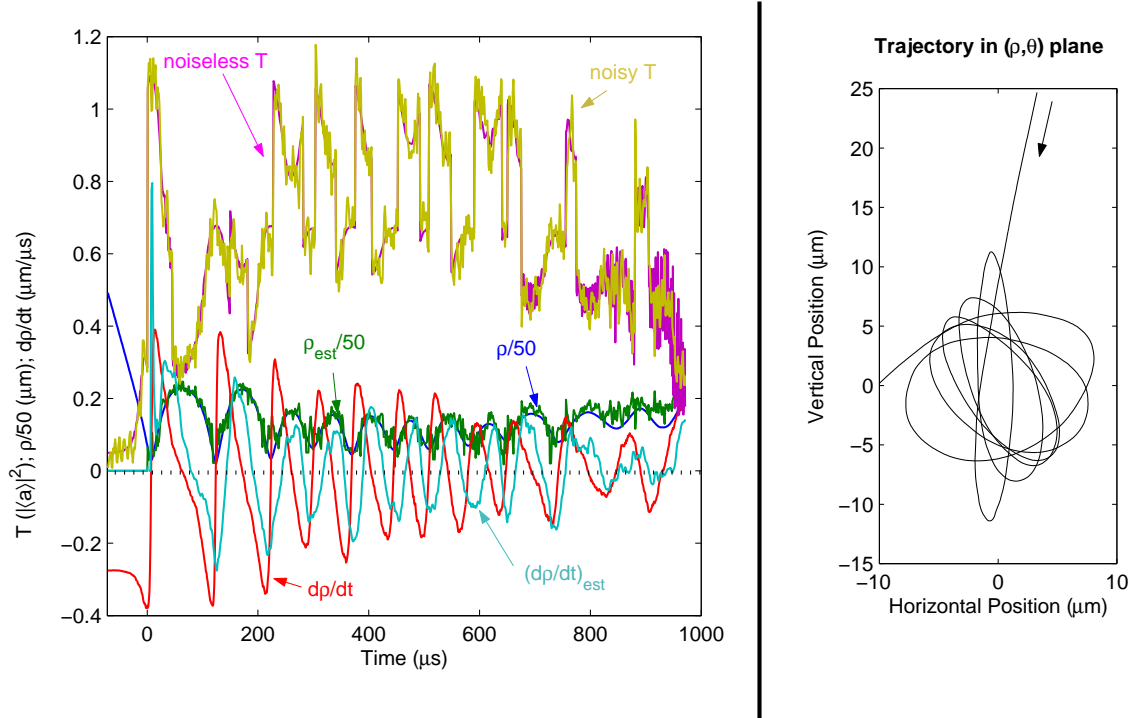


Figure 5.5: Delay is dealt with by tracking  $\rho$  turning points and using this information from each cycle to switch the potential at the predicted *next* turning point.

and  $lo \leftrightarrow hi$  thereafter based on the last zero-crossing time of  $\dot{\rho}_{est}$ .

However, the actual dynamical period varies by easily a factor of two over the course of an atom's trapping lifetime due to changing amplitude of oscillation in the anharmonic potential. Thus the fixed-period assumption is a poor one. A better strategy is to record the length of each period in  $\dot{\rho}_{est}$  and assume each cycle will be the same length as the previous recorded one. Thus the “waiting time” estimate will adjust itself as the dynamical period changes, though it will in general be one cycle behind. This strategy is employed for the trajectory shown in Figure 5.5. The initial switch occurs 45  $\mu\text{s}$  after trap turn-on, the least-squares window is 40  $\mu\text{s}$ , and the “wait time” between  $\dot{\rho}_{est}$  limit-crossings and the resultant potential switches is given by the previous period minus 20  $\mu\text{s}$ . This switching strategy, with deliberate delay based on an active measurement of the  $\rho$  oscillation time, appears to be a viable means of performing control in the presence of sensor noise and its associated loop delay.

### 5.2.4 Comparisons with Open Loop Strategies

To evaluate the effects of feedback more quantitatively, we introduce a figure of merit for the damping of radial oscillations in an atomic trajectory. Since the goal of the control strategy is to confine  $\dot{\rho}$  near zero, the performance can be measured by comparing the variance of  $\dot{\rho}$  over intervals of equal duration near the beginning of the trajectory and after feedback has been operating for some time. We choose a time window of duration  $200 \mu s$  as long enough to encompass well over one cycle of the radial motion. The comparison is taken between two such windows separated from one another by  $200 \mu s$ ; this delay is selected as long enough for several cycles of feedback action, yet short enough so that the statistic exists for a large fraction of trapped atom events. Thus our figure of merit for feedback performance is given by

$$M = \frac{\sigma_{15 \mu s \rightarrow 215 \mu s}^2(\dot{\rho}_{est}(t))}{\sigma_{415 \mu s \rightarrow 615 \mu s}^2(\dot{\rho}_{est}(t))} \quad (5.5)$$

where times are measured from the initial trapping (*exlo*  $\rightarrow$  *hi*) switch. Large values of the quantity  $M$  correspond to well-damped radial motion,  $\rho(t) \rightarrow constant$ , though orbits may still be circular at any radius  $\rho \geq 0$ . (Damping in the sense of actual energy removal is discussed further in Section 5.2.5.) Small ( $\sim 50 - 100 \mu s$ ) changes in delay time or window size have been investigated and do not appreciably change the nature of the results for  $M$ .

Figure 5.6 shows histograms of  $M$  for several data sets in which different switching protocols, detailed in Table 5.1, have been employed. Each data set is generated by simulating a fixed number of individual atom drops from the known distribution of initial conditions. Only some fraction of trajectories result in a triggering/trapping event, and of these only a fraction of atoms have dwell times long enough to compute a value for  $M$ . Thus, for example, set C2 was generated from 5,000 trajectories, yielding 1,335 trigger events and 147 trajectories for which  $M$  could be obtained (i.e., with dwell times at least  $615 \mu s$ ).

While Table 5.1 gives the specifics of each data set represented in Figure 5.6, the essential comparison is between closed loop – i.e., active feedback – algorithms and

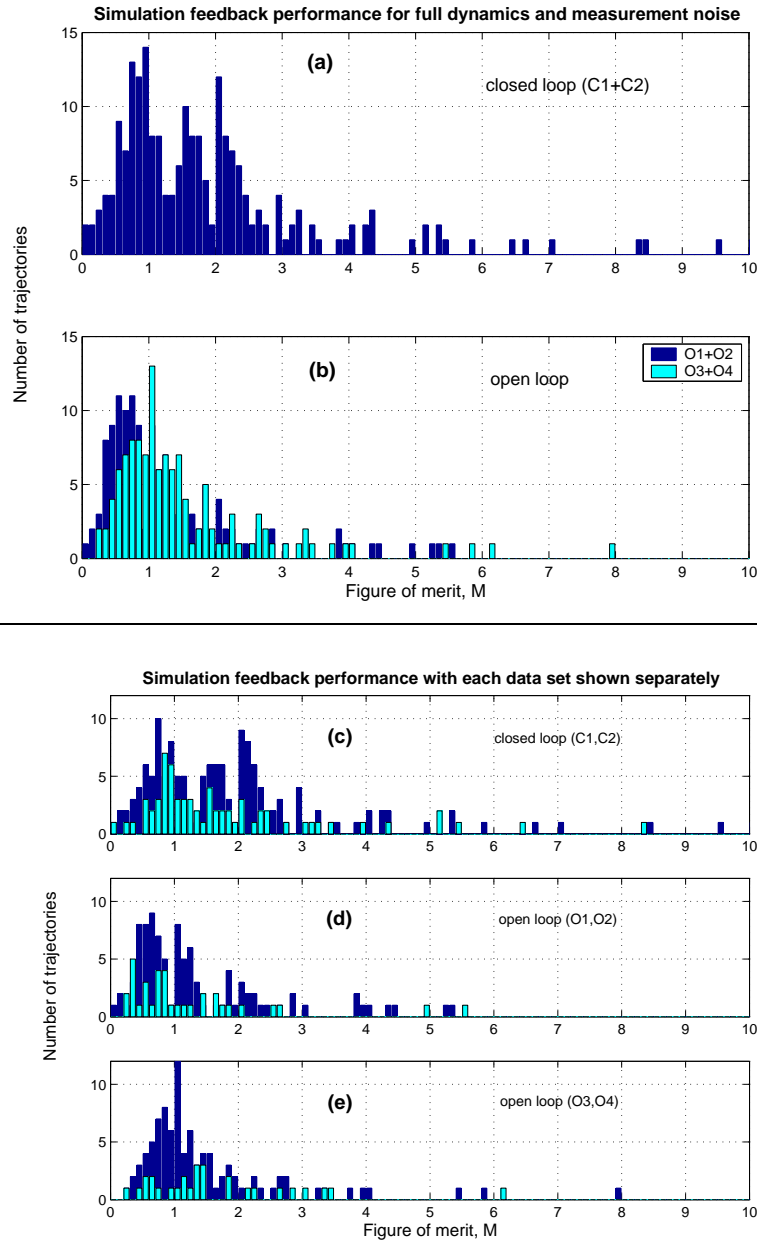


Figure 5.6: Figure of merit for feedback in closed- and open-loop cases (full dynamics). The data of (a,b) are redisplayed in (c,d,e) with each data set shown separately. In (c,d,e), the smaller data sets ( $C_1, O_1, O_3$ ) are shown with light-colored bars.

Data set	switching protocol	# atom drops	# triggers
C1	Closed loop Switch once $45 \mu\text{s}$ after initial trigger Thereafter switch (previous cycle length) - $20 \mu\text{s}$ after $(d\rho/dt)_{est}$ crosses limits	2000	534
C2	Same as above (C1)	5000	1335
O1	Open loop Switch every $45 \mu\text{s}$ after initial trigger	2000	561
O2	Same as above (O1)	5000	1319
O3	Open loop Switch every $35 \mu\text{s}$ after initial trigger	2000	552
O4	Same as above (O3)	5000	1322

Table 5.1: Exact conditions used for data of the full-simulation histograms.

open loop counterparts which simply switch potentials in a predetermined sequence independent of real-time position information for the individual atom. The closed loop algorithm is that of Figure 5.5, in which measurement noise and loop delays are dealt with by waiting nearly one cycle to apply the knowledge of motion gained during the previous oscillation. The open loop algorithms, in contrast, simply switch the potential between  $hi$  and  $lo$  at fixed intervals following the initial trapping event; the fixed interval is chosen to coincide with a reasonable average value for an atomic oscillation period.

Closed loop, active feedback clearly damps radial oscillations more effectively than its open loop counterpart. The  $M$  distributions in Figure 5.6(a,c) have larger mean than those in Figure 5.6(b,d,e), with the closed-loop histograms showing many trajectories pushed out to higher values of  $M$  by the active feedback. These results indicate that real-time measurements of  $\rho(t)$  can indeed be applied to facilitate cooling of a single atom's motion in that dimension.

Further refinements should improve the performance of the algorithm. For instance, the cycle-length predictor could be changed to allow asymmetries between  $\dot{\rho} > 0$  and  $\dot{\rho} < 0$  half-cycles. Additionally, the filters themselves could be adjusted or replaced with better estimators which incorporate information about angular momentum  $L$ .

### 5.2.5 Performance with Axial Motion Suppressed

In a final set of simulations, we investigate the performance of our radial cooling algorithm in a setting where the axial atomic motion is independently suppressed. With no (or little) axial motion, axial heating no longer limits trapping times and the effects of radial feedback can be seen more clearly. To achieve this in simulations, we impose an *ad hoc* elimination of the axial dimension; however, this case could be relevant to several future experimental scenarios. For example, trapping and sensing mechanicsms, both currently accomplished with the same probe beam, could be separated to allow a trapping field with a low scattering rate and much-reduced axial diffusion. Alternatively, the separation of axial and radial timescales could be exploited, either to apply axial cooling [96] between cycles of radial feedback or to simply avoid extra axial heating by ramping the potentials up and down at a rate that appears adiabatic to the axial motion while still impulsive in the radial dimension.

Prospects for implementation aside, simulations with no axial motion demonstrate some aspects of the radial feedback protocol that are otherwise less transparent. We explore this regime with a set of simulations that differ in three ways from those presented above. First, the axial dimension is eliminated entirely and the atom is artificially constrained to remain at rest at an antinode of the standing-wave cavity field. Second, since axial heating is no longer an issue, we employ somewhat deeper trapping potentials than in the simulations above. The weak probe level is still  $n_{exlo} = 0.05$  photons in the empty cavity, but now we turn on the trap initially at a level  $n_{exhi} = 0.6$  photons in the empty cavity, and we feed back by switching between this and the weaker level  $n_{hi} = 0.3$  photons. The effective potentials thus generated are  $\sim 50\%$  deeper than in the previous simulations using  $n_{hi}$  and  $n_{lo}$ . Finally, without axial motion we employ a coarser computational timestep of  $(1/30)\ \mu s$ .

Figure 5.7(a) shows the feedback figure of merit for the cases of closed-loop feedback, constant trapping at  $n_{hi}$  or  $n_{exhi}$ , and open-loop switching. Taking advantage of longer overall atom dwell times, we can now consider time windows separated by

a greater delay, so the quantity displayed here is

$$M' = \frac{\sigma_{15\ \mu s \rightarrow 215\ \mu s}^2(\dot{\rho}_{est}(t))}{\sigma_{1015\ \mu s \rightarrow 1215\ \mu s}^2(\dot{\rho}_{est}(t))} \quad (5.6)$$

rather than the original  $M$  of Figure 5.6. The result is qualitatively similar to that of the full simulation, with the closed loop strategy performing significantly better than its open loop counterpart. In this case, the mean value of  $M'$  for closed-loop feedback is  $\sim 2.5$  times greater than for open-loop switching or for no switching.

The data of Figures 5.6 and 5.7(a) indicate that our feedback algorithm acts to drive  $\dot{\rho}$  to zero, i.e., to circularize atomic orbits at a constant value of  $\rho$ . Such demonstrations, however, leave open the question of whether this algorithm actually removes total energy from the radial motion. With axial motion eliminated, we can now explore this issue by asking how the feedback algorithm affects trapping lifetimes. Figure 5.7(b) shows atom dwell times for the same three cases of closed-loop feedback, constant drive levels of  $n_{exhi}$  or  $n_{hi}$ , and open-loop switching. The increase in lifetime for closed-loop feedback is immediately apparent. Indeed, the closed-loop results agree well with an exponential lifetime of 8.9 ms, as contrasted with 2.6 ms for trapping at  $n_{exhi}$  alone, 1.9 ms for trapping at  $n_{hi}$ , and 1.1 ms for open-loop switching between the drive levels. This effect shows that active feedback as applied to the radial dimension does act to remove radial energy, in addition to simply pinning  $\rho$  to a constant value. Note that all these lifetimes are enhanced relative to the full three-dimensional case, in which both experiments and simulations have mean trapping times of only  $\sim 400\ \mu s$ . Lack of lifetime enhancement from radial feedback in the full simulation is some indication of the very weak mixing between axial and radial motion, so that cooling in one of these dimensions does little to control temperatures in the other.

### 5.3 Outlook for Experimental Implementation

The feedback simulations discussed in this chapter have been conducted with very close reference to the conditions realized in the experiment of Ref. [25], in particular

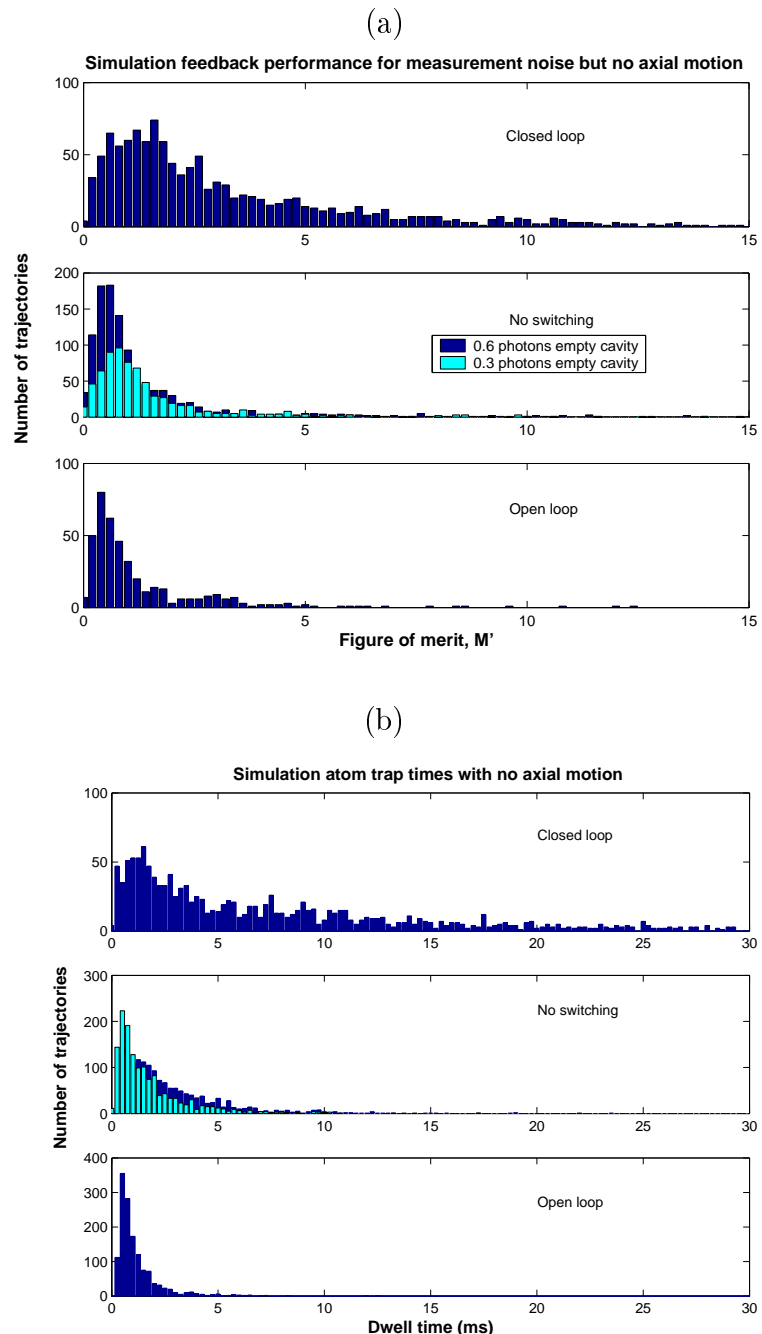


Figure 5.7: Feedback performance and lifetime enhancement in simulations with no axial motion.

for cavity properties, trapping statistics, and signal-to-noise in the balanced heterodyne detection. The current experimental effort, aimed at realizing the feedback strategies described here, employs very similar conditions while incorporating some improvements as in Ref. [51, 52]. Notable changes from Ref. [25] include a slightly shorter cavity, improved vacuum pressure in the cavity region ( $3 \times 10^{-10}$  torr) enabled by a differentially pumped double chamber, and cavity length stabilization via an error signal generated by an independent laser one free spectral range away from the cavity QED light. Implementation of the feedback strategy described above is clearly outside the regime of analog electronics, so an additional modification is the use of digital processing and FPGA technology [97]. With these tools, experimental data similar to the simulation results presented above seem well within reach; the experimental effort is discussed in more detail in the next chapter.

It seems reasonable to ask how much experimental data should be necessary to exhibit a distinction between active feedback and open loop schemes. From the simulations of Figure 5.6(c,d,e) (Table 5.1), we see that with data sets of about 500 trapped atoms the differences between open- and closed-loop schemes already begin to become apparent, and these differences are well demarcated with two or three times that much data. With fairly conservative estimates of one trigger per MOT drop and one MOT drop every 5 seconds, this means significant effects could well be seen with just one to two hours of experimental data at each setting. Much more data collection is experimentally realistic, allowing exploration of a wealth of additional questions.

## 5.4 Current Limits and Future Directions

The feedback algorithm developed above for the atomic radial position  $\rho$  is subject to basic limits arising from dynamical and measurement noise in our system. These limits can be expressed as lower bounds on the (one-dimensional) temperature for  $\rho$ . Because the strategy is based on discrete switching, with feedback delayed and timed based on the previous switching-cycle length, the control is always based on informa-

tion gathered over the previous motional cycle. Thus dynamical noise over an atomic motional timescale will set a lower limit on radial temperature  $T_\rho$ . Referring to Figures 4.11 and 4.13, we find that momentum diffusion (due to spontaneous emission) gives a typical energy increase per radial oscillation time of  $\Delta E_{\tau_r} \sim 0.02(U_0) \sim k_B(50 \mu K)$ . Furthermore, measurement noise places a limit on the detectable amplitude of  $\rho$  variations. This amplitude depends strongly on the absolute value of  $\rho$  due to the nonlinearity of the  $T \rightarrow \rho$  mapping. However, using the measured sensitivity (see Section 4.3) from the atom-cavity microscope, we estimate that over a motional cycle we can resolve  $\rho$  oscillations of amplitude  $(20 nm/\sqrt{Hz})\sqrt{1/2\pi\tau_r} \approx 0.77 \mu m$ . On the side of the cavity mode, where the effective potential is steepest, this corresponds to  $T_\rho \approx 150 \mu K$ . While this limit corresponds closely to the simulations of the previous section, where axial motion is suppressed, the full simulation never reaches this limit because axial heating cuts off atomic lifetimes too quickly. Thus improvements to address axial heating are of great interest for seeing the full effect even of radial cooling.

Beyond the experimental and algorithmic variations already discussed, a number of broader questions are raised by the use of active feedback to dynamically cool a component of motion for a single atom. One question deals with the ultimate limits of such a cooling mechanism. Within the current experimental setting, limits to radial cooling arise from atomic lifetimes (dominated by axial motion), but are also constrained by the dynamical noise and by the shot noise of detection. Some lifetime and dynamical noise issues could be addressed by separating trapping and sensing, for example by using a far off resonance trap in conjunction with a sub-photon level cavity QED probe [52]. The remaining issues would then center on signal-to-noise for the atomic position measurement, as well as on limits imposed by backaction of the measurement itself as it approaches the standard quantum limit [82, 98].

Extension of active feedback beyond the  $\rho$  dimension raises related questions. The question here is one of using various techniques – for example, a symmetry-breaking potential or frequency-domain filtering of the signal – to estimate and control a three-dimensional vector using the time record of a single quantity, the transmitted light

field. Undoubtedly, different driving parameters, detection methods, and data processing will be appropriate depending on the relative importance placed on information about each dimension of the motion. These questions address in various ways some basic issues of optimal state estimation and control for single quantum systems, and this experimental system promises to be a rich one for exploring such issues in further detail.

# Chapter 6

## Farther Up and Farther In

This chapter describes the current experiment to implement active feedback on the atomic radial position. In contrast to the general experimental summary of Chapter 3, here I treat in detail those aspects of the current experiment which were not present in the atom-cavity microscope setup.

The changes are in four broad categories. First, a more sophisticated vacuum chamber allows the pressure in the cavity region to be in the  $10^{-10}$  torr range even though the MOT loads from a Cesium vapor at several  $10^{-8}$  torr. The motivation for better vacuum in the cavity region is twofold: to allow longer trapping lifetimes for atoms should we reach that stage with the current apparatus, and to help protect the cavity mirrors from the slow death of Cesium coating. Since the chamber now has separate MOT-loading and cavity portions, we use a double MOT as well; the first MOT is loaded from Cesium vapor, cooled, and dropped through the differential pumping hole to be caught in a second MOT just above the cavity.

Second, the generation of probe light and the stabilization scheme for laser frequency and cavity length has been completely overhauled. We abandoned the Ti:Sapph for probe beam generation to avoid dependence on it and its 5-Watt pumping laser in favor of the cheaper, simpler diode laser option. At the same time, the desire for a cavity lock that was quieter and could tolerate longer atom transits led us to introduce an independent “locking” laser whose transmission now provides the error signal for locking the cavity length. As this laser is one free spectral range away from the cavity QED resonant light, we can use substantially more optical power in this

beam for a better error signal and more aggressive locking. The locking laser also has the clear advantage that it (and the cavity lock) can be left on throughout the atom-cavity interaction so that the cavity need not be left to drift for the duration of a transit.

The third change is, of course, what drove the rebuilding of the entire experiment: the absolute need for a new physics cavity. In replacing the ACM cavity we attempted to do better in a couple of ways. We adjusted details of the mirror mounting and gluing process in an attempt to eliminate some birefringence problems that have plagued earlier cavities. We also designed the cavity length exactly in order to leave open the possibility of a FORT at the “magic wavelength” [99, 52]; for a cavity as short as ours, the free spectral range is about 40 nm and so exact planning is required to make the cavity simultaneously resonant at 852 nm and near 935 nm. The new cavity succeeds in these areas, but brings its own unexpected quirks which we have had to deal with in pulling together the experiment.

Finally, getting serious about feedback as in Chapter 5 has led to the replacement of our old data acquisition and signal processing with a new Gage board for data acquisition and field-programmable gate array, or FPGA, for triggering and feedback. The old regime of data acquisition was Labview, notoriously slow and cumbersome to use online. Worse yet, our signal analysis and feedback tools were analog – essentially resistors and capacitors – and were ill-equipped to deal with a fundamentally digital feedback algorithm. In the feedback experiment we are performing right now, analog methods run into the problem of excessive loop delay due to differentiating the noisy signal. However, there is a more fundamental reason for the transition to digital. Referring to Figure 5.1, we recall that when we adjust the driving intensity to implement feedback, we change the whole system in a highly nonlinear way. The effective potential for the atom changes, but so do the dynamical noise for the atomic motion, the measurement noise, and the transfer function from cavity transmission to atomic position. Thus for each value of the control parameter the servo must adjust to reflect the altered transfer functions throughout the system. FPGA’s, with their reconfigurable nature and high speed a/d, d/a, simple signal analysis, and conditional

logic, come to the rescue in the implementation of effective feedback in the system [97].

## 6.1 Vacuum and MOTs

A schematic of the differentially pumped vacuum chamber is shown in Figure 6.1. The main upper chamber is constructed from a Kimball Physics small spherical hex, while the main lower chamber is the custom NorCal vacuum feedthrough retained from the atom-cavity microscope main chamber. They are connected via a long, narrow differential pumping hole to support a sizeable pressure difference between the upper and lower chambers. The lower chamber is pumped with a 55 l/s Varian Starcell ion pump and equipped with a nude Bayard-Alpert ionization gauge to monitor vacuum pressure, while the upper chamber is pumped with a 20 l/s Starcell and has a straightforward B-A gauge. The upper chamber contains the Cs reservoir and is operated as a Cs vapor cell for loading of the upper MOT; the pressure in this part of the chamber is a few times  $10^{-8}$  torr. The lower chamber, on the other hand, is maintained at several  $10^{-10}$  torr and contains the physics cavity itself.

### 6.1.1 Chamber Design and Construction

The chamber itself, surrounded by MOT coils and optics for the MOT and probe, is shown in Figure 6.2. The lower chamber has two large (6") windows for generous optical access along the cavity (and primary MOT) axis; in this direction we couple light into the cavity and also align a retro-reflected MOT beam skimming the top of the cavity substrates. The MOT is also imaged through the large windows. The chamber has eight smaller ports in the transverse plane. Four of these are windows permitting MOT beams in the remaining two dimensions. One goes to the lower ion pump/gauge region, one connects to the upper chamber, and one is used for imaging of the lower MOT. A final window (the bottom) is unused and provides optical access only to the bottom surface of the cavity mount piece.

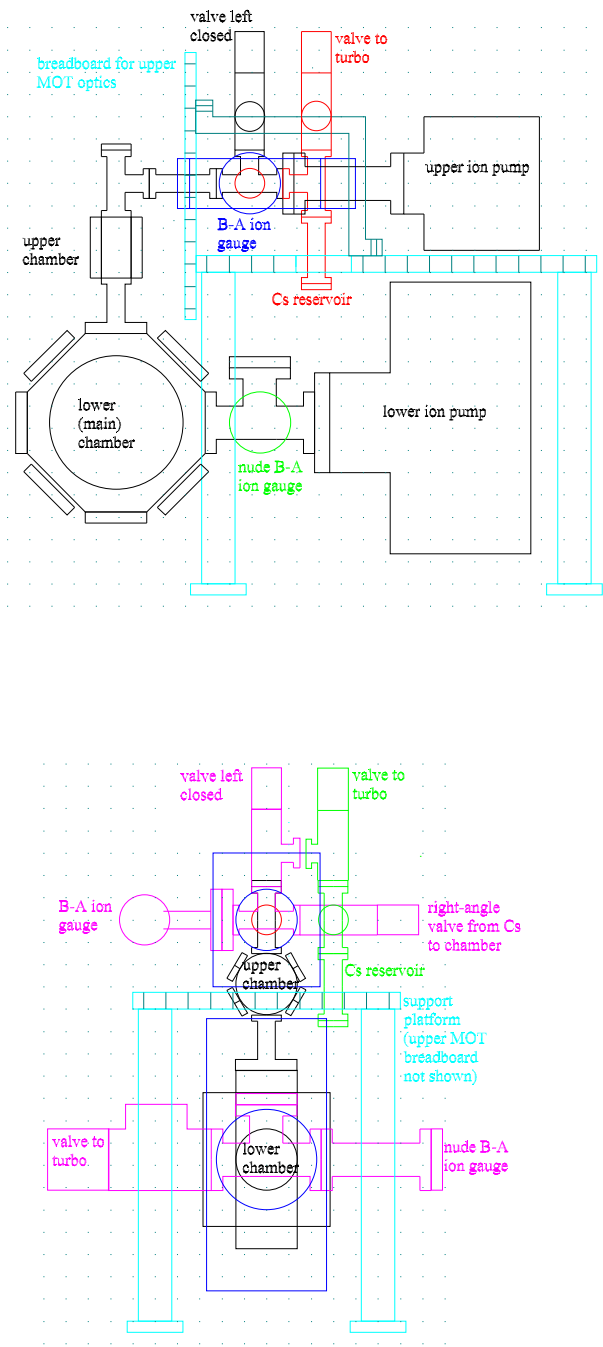


Figure 6.1: The differentially pumped vacuum chamber, seen from along the physics cavity axis (top view) and from the side (bottom view).

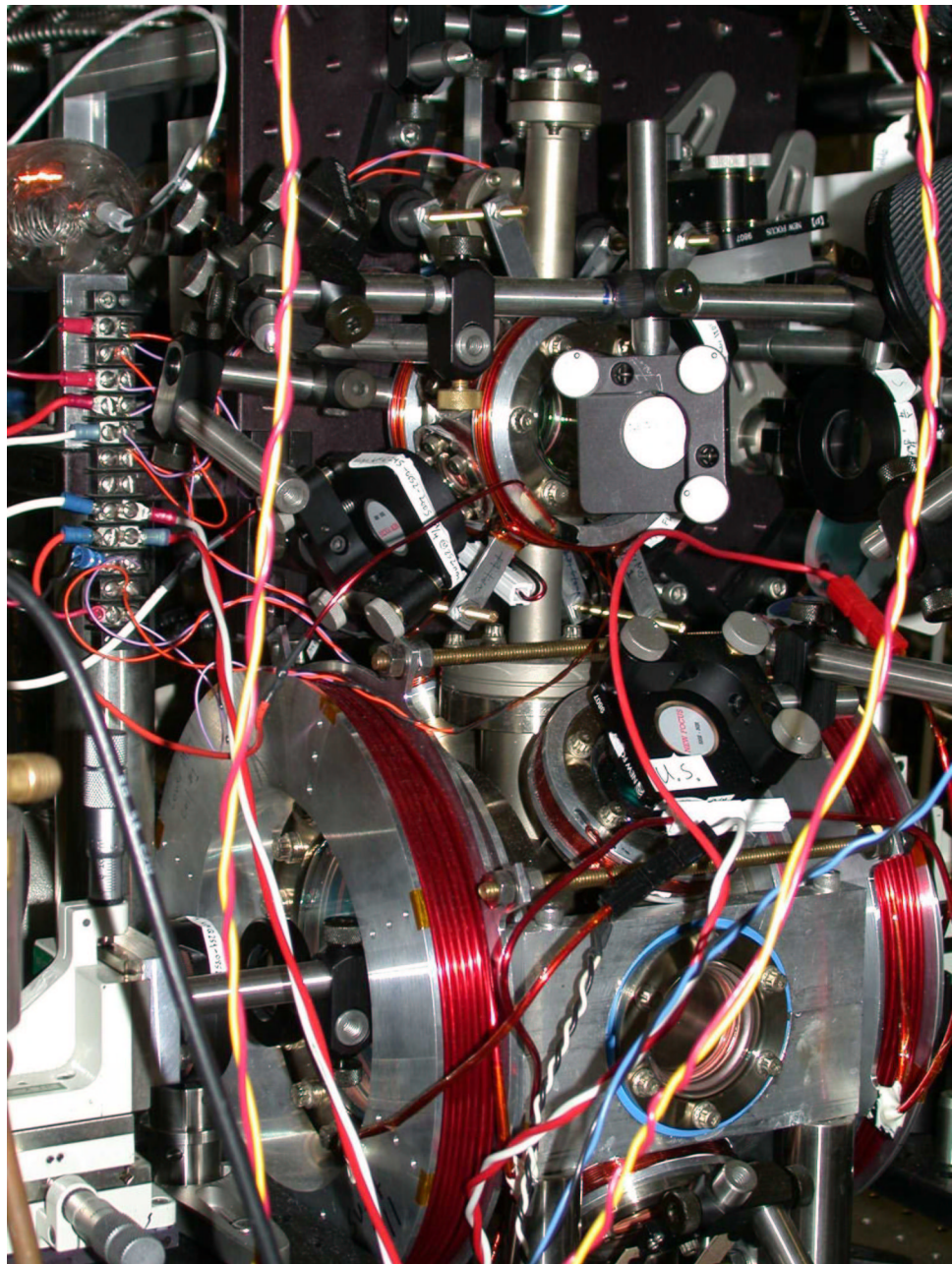


Figure 6.2: Actual upper and lower chambers with MOT coils and optics in place.

The upper chamber has two 2-3/4" windows along the upper MOT axis and six 1-1/3" ports evenly spaced around the sides. Four side windows are used for MOT beams, giving us three pairs of MOT beams which are not strictly orthogonal. The effect on MOT performance has been minimal, both here and in the lower chamber where the cavity-axis MOT beam pair are slightly angled as well. The upper chamber's small bottom port connects to the lower chamber, and the top port connects to a window and the upper pump/gauge/reservoir region. Upper MOT imaging is performed through the top window and through the front 2-3/4" window of the hex. All the vacuum windows are antireflection coated from 820-930 nm by Larson.

### **6.1.2 Cesium Reservoir and Vapor Cell Loading**

The Cesium reservoir is separated from the upper chamber by an all-metal right-angle valve (from VAT). Cesium is loaded into the (already pumped-down) chamber as illustrated in Figure 6.3. The reservoir region is valved off from the main chamber and opened to air (or nitrogen if Cesium has already been present in it). A complete glass ampule containing Cesium metal and a buffer gas is cleaned and placed inside the bellows, with one end resting against each side of the bellows wall. The reservoir region is connected to a turbo pumping station and pumped down from atmosphere. Bending the bellows (as forcefully as necessary) cracks open the ampule, and the turbo pump load surges as buffer gas is pumped out. After ultrahigh vacuum (UHV) is attained, the reservoir is closed to the turbo pump and opened to the rest of the upper chamber if desired. Cesium is kept in the reservoir by closing the right-angle valve to the chamber and Peltier cooling the bellows end. The vapor cell in the main upper chamber is replenished by opening the right-angle valve and gently heating the reservoir. Initial buildup of the vapor cell took about ten days with the Cesium open to the chamber and kept a few degrees above room temperature. This time is consistent with initial coating of the surfaces between the reservoir and the upper MOT location. Subsequent re-loading of the vapor cell is much faster as surfaces remain mostly coated with Cs.

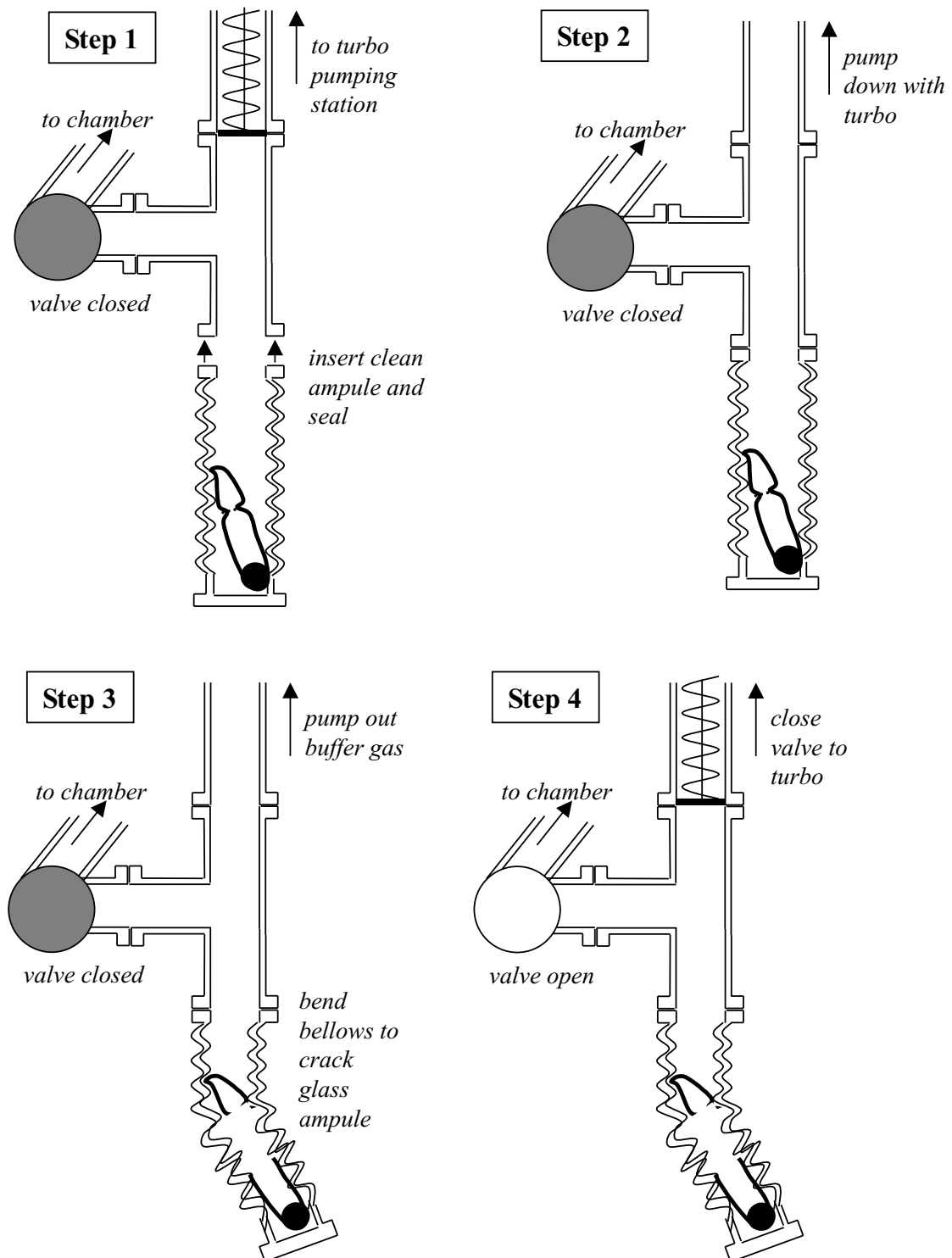


Figure 6.3: Cesium reservoir and loading procedure

### 6.1.3 Differential Pumping

The pressure difference between the upper and lower chambers is made possible by means of a deliberately low-conductance (long and narrow) connection between them, known as a differential pumping hole. Our differential pumping hole forms a tube of length 122.6 mm and diameter 5.75 mm which connects the upper and lower chambers. The tube begins 1.9 cm below the center of the upper chamber, and does not extend far enough into the lower chamber to cut off any optical access through the large windows there. The dimensions of the hole are constrained by two requirements: support for the desired pressure differential between upper and lower chambers, and clearance for dropping a cloud of cooled Cs atoms through the hole.

To support a ratio of pressures  $P_{upper}/P_{lower} \geq \Delta$  in a system where the lower chamber effective pumping speed is  $S$ , the conductance through the differential pumping hole must satisfy  $C \leq S/\Delta$ . A hole of diameter  $D$  and length  $L$  has a conductance (for Cesium) of  $C = 5.7 \frac{D^3}{L + \frac{4}{3}D}$  where the dimensions are expressed in centimeters and the conductance is measured in liters per second. Thus a minimum pressure ratio  $\Delta$  imposes a relationship between the length and diameter of the hole,  $L \geq 5.7 \frac{\Delta}{S} D^3 - \frac{4}{3}D$ . The lower chamber is pumped by a nominally 55 l/s ion pump, estimated to be close to  $S_{pump} = 25$  l/s in practice for Cesium. The connection to the pump is through an arm of diameter 1-1/2" and total length 7.68", giving a conductance of  $C_{path} = 12.8$  l/s. Thus an overall effective pumping speed for the lower chamber is estimated at  $S = (\frac{1}{S_{pump}} + \frac{1}{C_{path}})^{-1} = 8.5$  l/s. Under these conditions we set a target of  $\Delta \approx 100$ .

In order to drop atoms through the hole with reasonable throughput, we first position the hole as close below the initial cloud position as we reasonably can without cutting off optical access. In reality we have allowed a vertical space of  $s = 1.9$  cm which generously allows for trapping beams and for some error in positioning of the initial MOT. Assuming the pumping hole is aligned perfectly with respect to gravity, a cooled atomic cloud with initial diameter  $d_0$  and transverse velocity spread  $v_s$  clears the hole if  $L \leq [(\frac{D-d_0}{v_s})^2 \frac{a_g}{2} - s]$ . Here  $a_g$  is used to denote the acceleration due to gravity. By assuming an attainable sub-Doppler temperature of

$3 \mu K$  ( $v_s = \sqrt{2}v_{rms} = 1.8 \text{ cm/s}$ ) based on a similar system quoted in [100], and an initial diameter of 1.5mm, we obtain bounds on  $L$  and  $D$  from this requirement.

Considering these two effects of pumping hole dimension, we plot in Figure 6.4 the constraints on  $L$  and  $D$  imposed by our target requirements. By these arguments our pumping hole should support a pressure ratio of  $P_{upper}/P_{lower} = 102$  and barely allow a cloud of initial diameter 3 mm and temperature  $6 \mu K$  to pass as described above. A cloud of temperature  $3 \mu K$  passes even allowing a 1% deviation of the pumping hole axis from the direction of gravity. Clearly alignment with gravity is an important step in the chamber assembly! In practice we maintain a pressure ratio of about 50 as measured with ion gauges in the upper and lower chambers. The transfer efficiency from the upper MOT to the lower chamber has not been calibrated but is certainly sufficient for our single-atoms experiment.

The differential pumping hole is a custom piece mounted to fit into the upper and lower chambers and the standard adapting nipple which connects them. In mounting the piece, care was taken to ensure a good vacuum seal everywhere except through the actual tube. At the same time, a design goal was to promote overall good vacuum pressure by avoiding “virtual leaks” arising from large surface areas close to one another, leading to low-conductance regions which are hard to pump out. Furthermore, any excess surface areas (in close contact or not) should be put on the worse-vacuum side of the design if possible. Finally, based on the bitter experience of Jun Ye and Dave Vernooy in their differentially pumped chamber, care must be taken to ensure that the pumping hole will stay in place during transient pressure differences that arise during initial pumpdown from atmosphere.

The mounting of the differential pumping hole is shown in Figure 6.5. The pumping hole is essentially a hollow tube of 304 stainless steel, with an inner diameter of 5.75 mm over its entire 122.6-mm length. Most of this length is taken up by the top portion, of outer diameter 10 mm, which begins in the upper chamber and extends through the adapting nipple while staying well away from its walls. At the very bottom of the nipple’s length, the differential pumping tube steps up to an outer diameter of 17.1 mm to snugly fit into the end of the nipple. The larger outer diameter persists

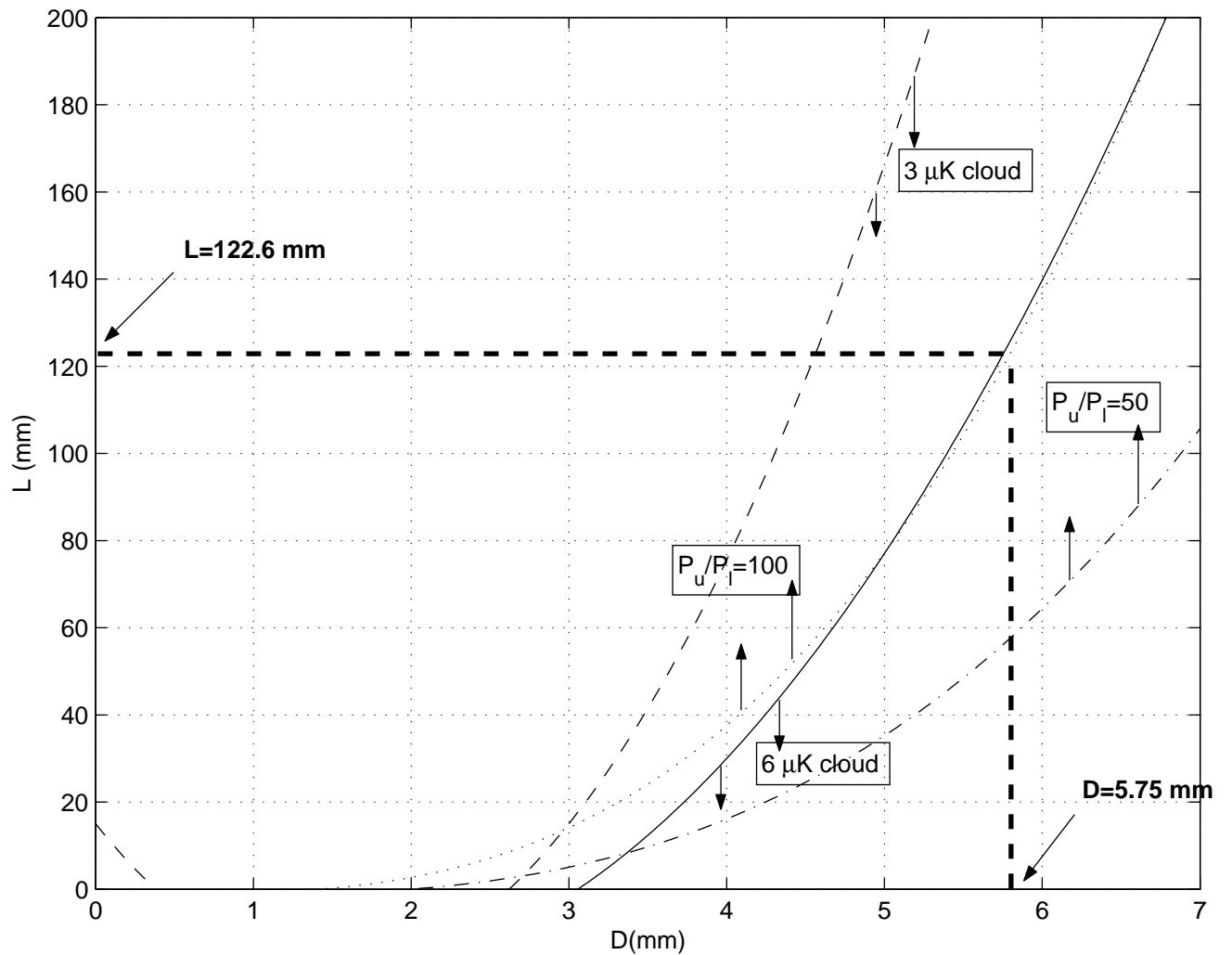


Figure 6.4: Pressure-ratio and MOT-dropping constraints on differential pumping hole length  $L$  and diameter  $D$ . For a given value of  $D$ , pressure requirements give lower bounds on  $L$ ; these constraint curves are shown with arrows pointing up from them. Transmission of an atom cloud gives an upper bound on  $L$ , so these constraint curves are denoted by downward arrows.

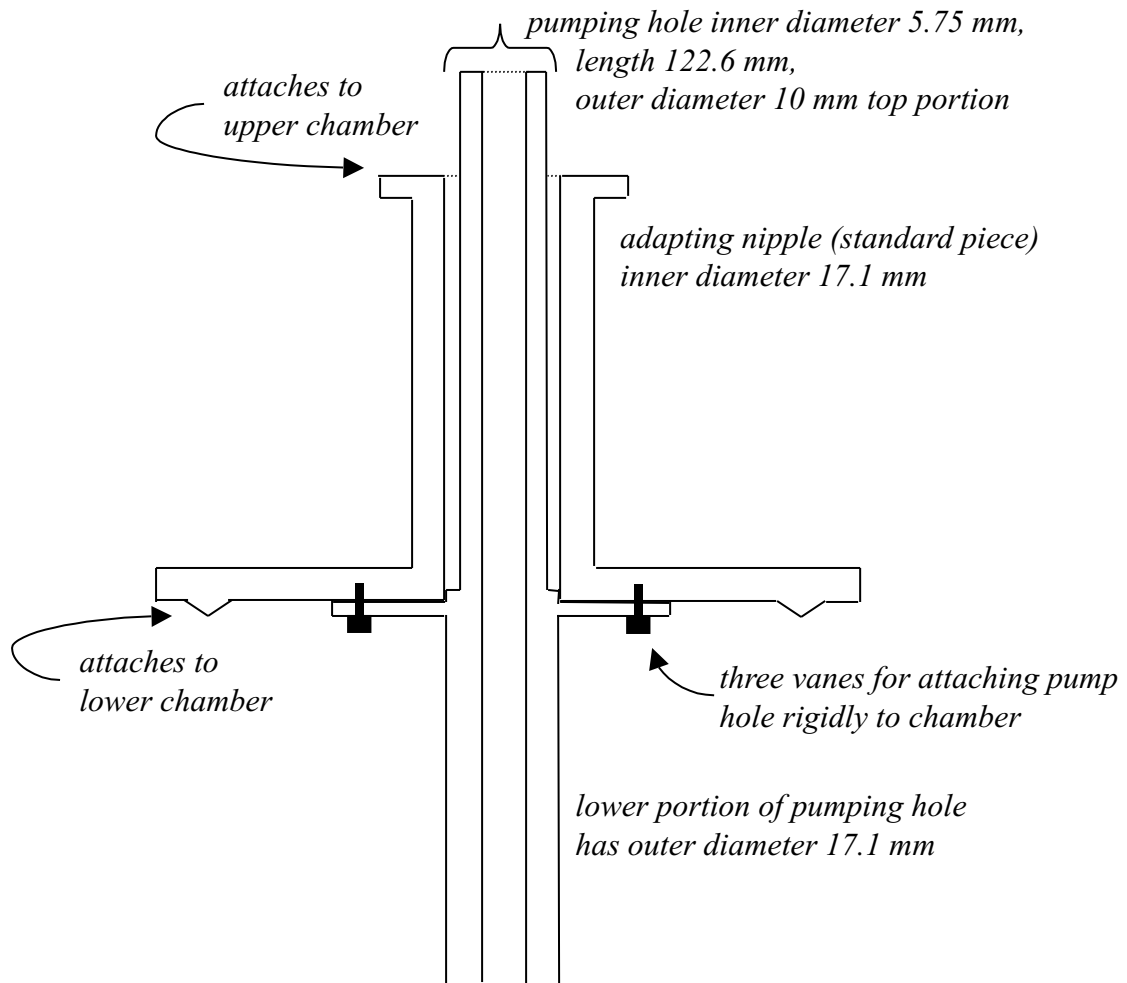


Figure 6.5: Design and mounting of the differential pumping hole. The adapting nipple attaches to the lower chamber via a 2-3/4" conflat flange, and to the upper chamber via a 1-1/3" conflat flange.

through the portion of the pumping hole length that extends into the lower chamber. Finally, at the junction with the bottom of the adapting nipple, three vanes extend radially from the pumping hole with through-holes for 6-32 screws. Corresponding threaded holes are drilled into the flat surface of the adapting nipple at this end, allowing firm attachment of the pumping hole piece to the chamber with 3/8"-long screws. It is important to plate these screws with gold before assembling the components; otherwise the UHV-clean screws and stainless-steel threaded holes will almost inevitably seize up and get stuck during assembly.

### 6.1.4 Getting Atoms to the Cavity: Upper and Lower MOT's

Atoms are delivered to the cavity mode volume by a cycle of

- loading the upper MOT in the center of the upper chamber, with upper anti-Helmholtz coils on and trap light on (3 seconds).
- cooling the upper cloud, with quadrupole coils off and trap light reduced and detuned (35 milliseconds).
- dropping the upper cloud, with coils and trap light off (100 milliseconds).
- catching the cloud in a lower MOT just above the cavity substrates, with lower antiHelmholtz coils on and trap light on (200 milliseconds).
- cooling the lower cloud, with quadrupole coils off and trap light reduced and detuned (35 milliseconds).
- dropping the lower cloud, with coils and trap light off, observing transits through the cavity, performing triggered trapping and feedback (25 millisecond average drop time to cavity mode, acquire data during 10 or 20 ms window around this).

A diagram of timing for this cycle is shown in Figure 6.6.

The trap light for both MOT's is generated from a single diode laser pumping an SDL tapered amplifier and single-passed through an AOM for intensity-switching capability. The final trapping beam is split to separate polarization-preserving fibers for the upper and lower MOT's. Thus the light in upper and lower chambers is switched as a single unit rather than individually; since the timing of upper and lower MOT's does not overlap anyway, this is an acceptable strategy. A double-pass AOM before the SDL amplifier controls the detuning of the trap light. The trap beam is tuned 11.8 MHz to the red of  $(F = 4) \rightarrow (F' = 5)$  during MOT loading and 23.8 MHz to the red during sub-Doppler cooling. Repump light on  $(F = 3) \rightarrow (F' = 4)$  is likewise generated from a single diode laser, split to pass through the same two fibers as the trapping light as well as through a third fiber which delivers some of it to the cavity input path itself. The repump light is left on continuously.

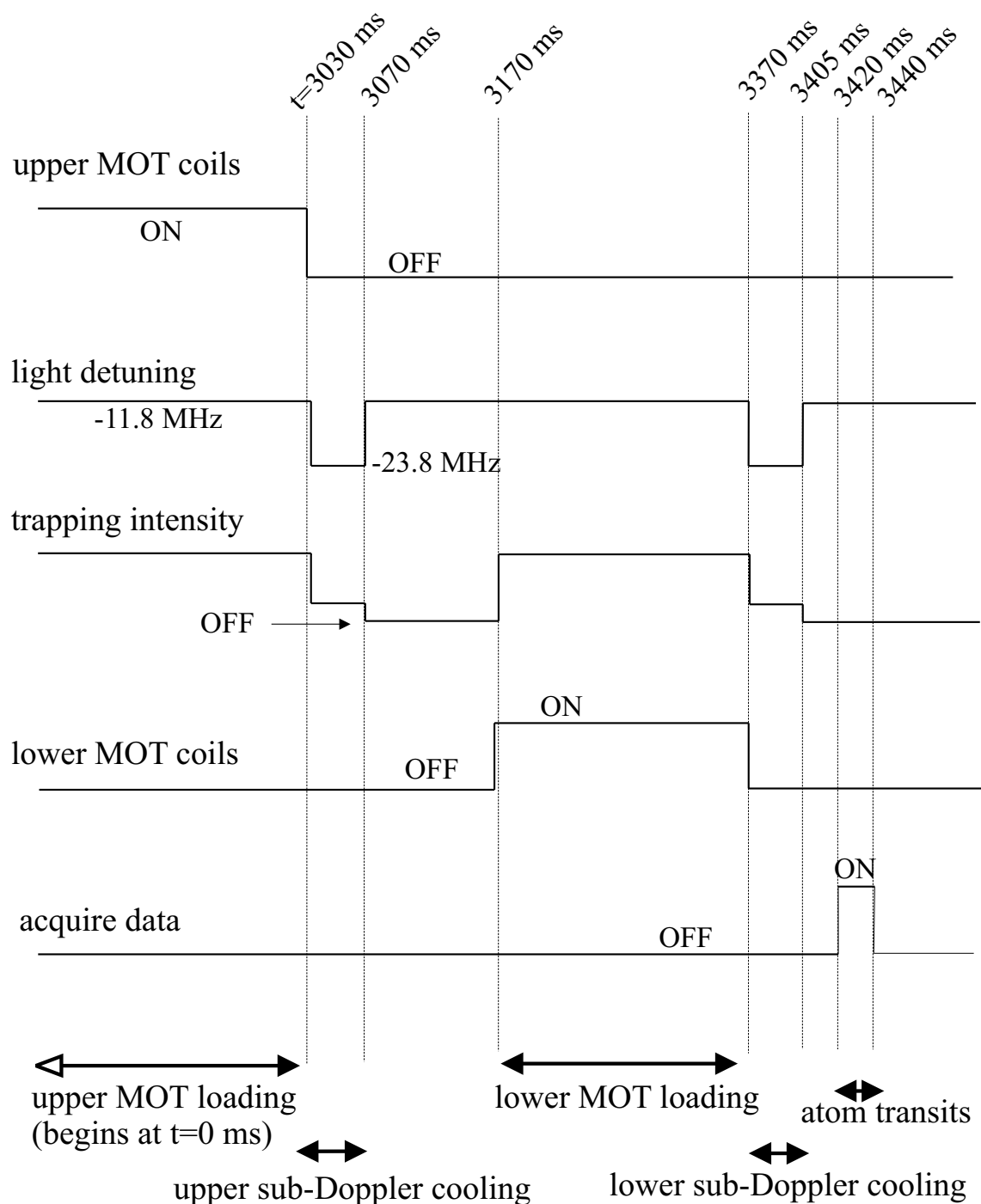


Figure 6.6: Timing diagram for experiment with double MOT.

The magnetic field gradients for the MOT's are provided by upper and lower sets of anti-Helmholtz coils (main coils), with additional Helmholtz coils in all three dimensions to provide zeroing of the magnetic field. The upper main coils are 14 AWG single-build insulated magnet wire wound onto aluminum forms and mounted without direct contact with the chamber. The lower main coils are of similar construction but wound with 10 AWG heavy-build insulated magnet wire. While anti-Helmholtz magnetic field coils may ideally have their dimensions (coil radius and separation) designed to realize as closely as possible a perfect linear gradient field at their center [101], in practice our coil design is driven instead by crowding and requirements of geometry close to the chamber. The properties of upper and lower main coils are given in Table 6.1. The table gives the average radius ( $R$ ) of each coil, the average separation ( $2A$ ) between the coils, the number of turns in each coil ( $N$ ), and the resulting field strength at the center of each coil for an applied current. The operating current and the resulting field gradient at the MOT location are also shown. A bias coil below the chamber is also used to push the lower MOT field zero up about 3 mm from its natural location, essentially at the physics cavity itself.

	upper MOT	lower MOT
trap power (total)	43 mW	65 mW
loading time	3 s	200 ms
sub-Doppler power	2.4 mW	4.3 mW
cooling time	35 ms	35 ms
repump power (total)	4.3 mW	7.2 mW
coil radius ( $R$ )	4.0 cm	9 cm
coil separation ( $2A$ )	6.0 cm	18 cm
turns per coil ( $N$ )	18	118
field at center of each coil	(2.85 G/A, 2.83 G/A)	(9.0 G/A, 8.4 G/A)
operating current	8 A	15 A
field gradient on-axis at MOT	8.4 G/cm	16 G/cm

Table 6.1: Upper and lower MOT parameters

Optical powers and magnetic field properties for the upper and lower MOT's are given in Table 6.1. The number of atoms in each MOT has not been calibrated, and rough magnetic field zeroing through time-of-flight imaging has so far resulted in hot

sub-Doppler temperatures ( $\sim 60 \mu K$ ). However, as these conditions have produced the desired result of one to several atom transits per MOT-dropping cycle, further optimization has not yet been pursued.

## 6.2 Probe Beam Generation and Locking Scheme

This experiment has seen considerable modification in probe beam generation and in locking of both the probe beam frequency and the cavity length itself. The new lab schematic borrows the concept of the cavity and probe lock used in [51, 52, 100], where the error signal for locking the physics cavity length is generated by transmission of a separate “locking laser” on a different longitudinal mode from the cavity QED light. The frequencies of this laser and the probe laser are both locked to modes of a stable reference cavity introduced for this purpose. Finally, Cesium FM saturated absorption spectroscopy of the probe beam provides an error signal for maintaining the reference cavity at a fixed frequency and tying the entire system to the atomic transition. The probe beam itself is no longer generated from a Ti:Sapph, but comes from a grating-stabilized diode laser at 852nm (total output power 40 mW).

Figure 6.7 shows a schematic of the frequency shifting and locking setup for the experiment. A portion of the probe laser power, as a single-frequency beam with no sidebands, is sent through a fiber to the probe and local oscillator paths. The probe beam is double-passed through AOM’s before being sent to the cavity. The probe is thus shifted down by 2(110 MHz) and up again by 2(95 MHz) to provide the 30 MHz LO-probe frequency offset used for heterodyne detection. The use of two separate AOM’s avoids the presence of strong RF signals at the heterodyne frequency itself; if a single AOM at 15 or 30 MHz is used, electrical pickup of the driving signal can cause excess noise on the heterodyne.

The probe light *not* used for the probe and LO paths is double-passed through an acousto-optic modulator (AOM), sent through a electro-optic modulator (EOM) where it acquires 5.1 MHz FM sidebands for locking purposes, and finally sent to the reference cavity and to Cesium. The probe beam detuning from atomic resonance

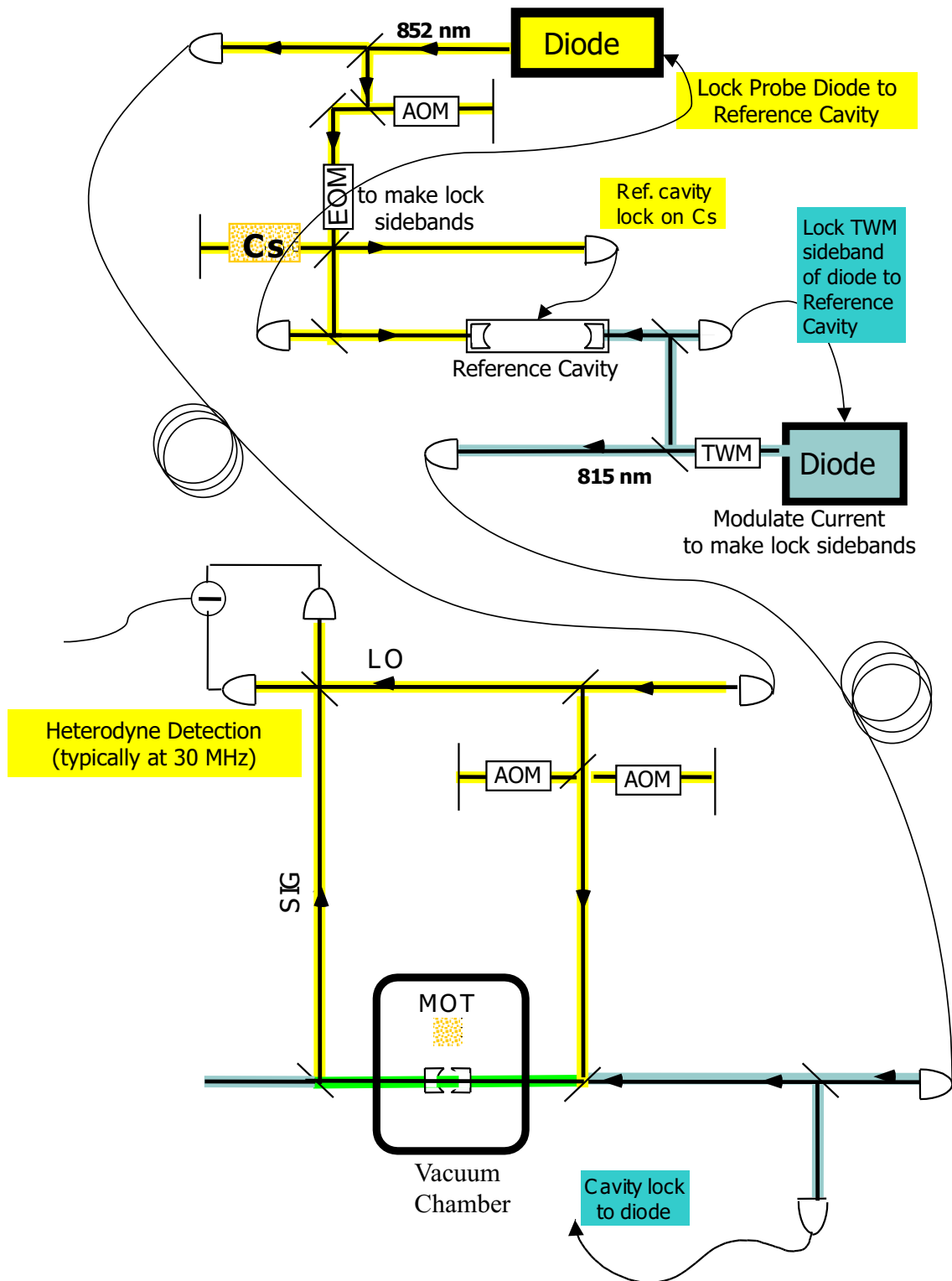


Figure 6.7: Schematic of laser and cavity stabilization

can be set by tuning the double-pass AOM frequency and locking to different Cesium saturated absorption features.

The locking laser operates at a wavelength of 814.8 nm, which is one free spectral range away from 852 nm on the physics cavity. This laser was originally an 825 nm unit pulled to 814.8 nm by cooling to about 12°C. For better linewidth and stability, we have recently replaced it with an 808 nm diode from JDS Uniphase which is grating-pulled to 814.8 nm and operated at 24°C to increase stability at this wavelength. The locking diode is current modulated to produce FM sidebands at 6.2 MHz on the entire lock beam; these sidebands are used for locking of the locking laser to the reference cavity and also of the physics cavity to this laser. The lock laser is also passed through a traveling-wave modulator (TWM) which generates sidebands as far out as 1 GHz; the TWM-generated sideband is locked to the reference cavity but the physics cavity is locked to the carrier. Tuning of the TWM frequency ensures consistency in the resonance conditions of both lasers (probe and lock) with both cavities (reference and physics).

Both lasers are locked to the reference cavity in reflection using the Pound-Drever-Hall technique [102, 103]. The locks employ the lab-standard two-branch locking circuit, worked on by many group members in sequence, including notably Joe Buck and Hanns-Christoph Naegerl, with the most recent version coming from J. M. Geremia. The demodulated error signal drives the diode current via a fast branch and also drives the grating-mount piezo via a slow branch with an integrator.

The reference cavity has finesse  $\sim 10,000$  and length 30 cm for a linewidth of about 50 kHz. The mirrors are mounted on either end of a quartz tube, with one mirror mounted on a PZT for length adjustment. The cavity is solidly held in a series of vibration-isolating materials, but is not kept in vacuum or actively temperature stabilized. The probe laser Cs spectroscopy setup provides an error signal used to lock the reference cavity to an atomic transition. This lock uses the slow branch of the same two-branch locking circuit to feed back to the reference cavity piezo; the important feature in this lock is simply a good integrator for slow drifts.

Finally, the physics cavity itself is locked to the locking laser carrier, as described

above, again in reflection and via the Pound-Drever-Hall technique. The locking circuit used to feed back to the physics cavity closes loop at  $\approx 5$  kHz; this error signal is then added to the voltage-divided output of a 300 V battery and sent to one of the shearing PZT's on the cavity mount. The second shear PZT is grounded to the cavity mount. A battery is used to generate the large DC offset voltage in order to avoid the introduction of electrical noise, particularly near the  $\approx 50$  kHz mechanical resonance of the cavity mount system. Noise near this frequency is unfortunately endemic in the lab, due to power supply switching of, among other things, HeNe power supplies and television monitors. Using a simple chemical-cell battery in place of a more conventional high-voltage power supply helps to reduce the electrical noise driving the cavity PZT. In voltage-dividing the battery output, however, it is important to consider the effect on the transfer function of the servo system. This point is critical because the shear mode PZT itself has a quite large (4 nF) capacitance. Thus the equivalent resistance introduced through the voltage divider creates a low-pass filter that tends to reduce the servo bandwidth. We use a  $100\text{ k}\Omega$  resistance in the voltage divider, resulting in a  $\sim 1\text{kHz}$  low pass for the final voltage onto the shear mode PZT (400 Hz to 1.6 kHz depending on the setting of the voltage divider).

The physics cavity finesse at 814.8 nm is about 240,000, a factor of two below the finesse at the center of the mirror coating curve (near 852 nm). The circulating lock beam power in the physics cavity must be small enough to cause negligible AC Stark shifts on the relevant cavity QED transitions. Since the lock beam is 16 THz from resonance, we may still use considerably more optical power for locking here than we were able to use with the cavity QED probe beam itself. In particular, a mode-matched power of  $0.2\ \mu\text{W}$  of lock beam light on the physics cavity will shift the cavity QED transition by  $\lesssim 1$  MHz, at the edge of the frequency resolution we possess in the experiment. This estimate considers only the  $6S_{1/2} \rightarrow 6P_{3/2}$  transition; actually the Stark shifts will even be somewhat smaller due to contributions from the  $6P_{3/2} \rightarrow 8S_{1/2}$  transition at 794 nm (see Figure 3.2).

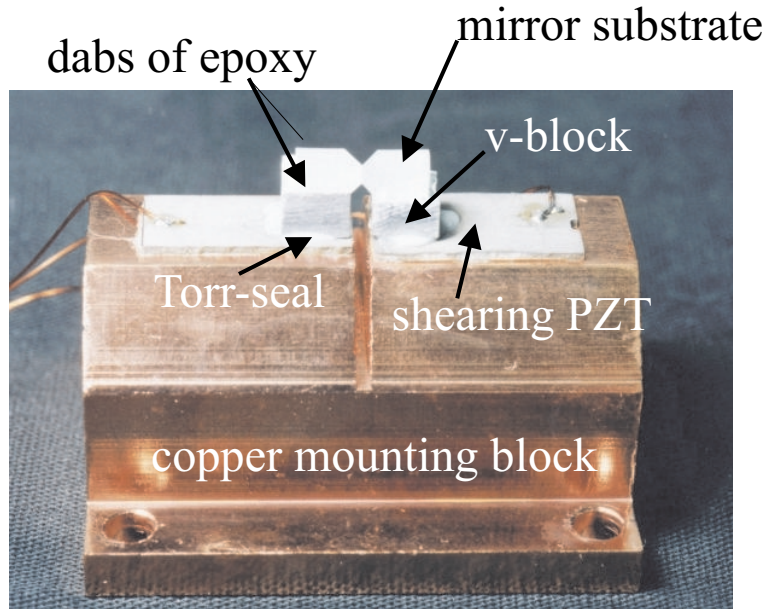


Figure 6.8: Cavity mount piece: detailed design

### 6.3 New Physics Cavity: Improvements and Difficulties

We replaced the atom-cavity microscope physics cavity with one which is similar but has several changes in its design and construction. Figure 6.8 shows a detail of the cavity mounting piece.

Before discussing this cavity in detail, I briefly review the procedure for assembling a cavity of this design. All components except the mirrors are first cleaned and baked with a view to their eventual introduction into a UHV environment. Mirrors are cleaned and inspected by hand as close as possible to the time of use. Even so, they are shielded from dust in the intervening time by careful storage, and by construction of the cavity in a clean hood. The shear-mode PZT's are glued to the copper mounting block, allowing one day for this glue to set, and leads are soldered to the PZT's and mount. One v-block is then glued on top of its PZT, and mirrors are glued to both v-blocks with small dabs of epoxy. These adhesives are allowed to set for one day. Finally, the cavity is aligned by placing the mounting block on a translation stage and positioning the free mirror/v-block unit in a holder attached to a mirror mount.

The cavity is aligned and set to the desired length; then the translation stage is wound down, glue is applied, and the translation stage is wound up again to form the final bond between the free mirror-v-block unit and its shear-mode PZT. Small adjustments may be made during the first 30 to 60 minutes after this glue is applied. After this bond has set for one day, the holder is removed and the resulting cavity can be measured and moved into place.

The current physics cavity is constructed from mirrors of the same coating run as the previous cavity, giving it a measured finesse of  $F = 480,000$ . Both mirrors have 10-cm radius of curvature, and the cavity length is now  $l_{eff} = 9.2 \mu\text{m}$ , giving a field waist of  $w_0 = 13.3 \mu\text{m}$  for the  $TEM_{00}$  mode. The new cavity has  $(g_0, \kappa)/2\pi = (130, 17)$  MHz, leading to  $m_0 = 2.0 \cdot 10^{-4}$  and  $N_0 = 5.2 \cdot 10^{-3}$ . This cavity was built, as described below, with particular attention to ensuring low birefringence and to selecting a specific cavity length. Unfortunately it also suffers from an unintended length sensitivity to magnetic fields, as chronicled below as well.

### 6.3.1 Controlling Birefringence

Cavity birefringence is discussed in more detail in Chapter 7, but here I simply remark that it has been an issue in the construction of all very high finesse cavities to date, and can largely be traced to mirror mounting techniques rather than to inherent properties of the coatings themselves. Stress induced by gluing (or clamping) transmits through the substrate to the mirror surface and induces a troublesome birefringent phase shift in the coating.

As mentioned in Chapter 3, the previous prescription for reducing cavity birefringence was to glue down the substrates with as little glue as possible, as far from the mirror surfaces as possible. Furthermore, our experience was that a low-birefringence cavity, when subjected to a heating and cooling cycle (to  $\approx 100^\circ\text{C}$ ), often developed birefringence as much as an order of magnitude larger than the original. When such a cavity was disassembled, the same mirrors could again be used to make a low-birefringence cavity; thus blame still focused on stress induced by the mount, this time

through a process of final glue setting or differential thermal expansion/contraction of mounting components. The end result was a prohibition on heating of physics cavities, meaning a complete inability to bake out a vacuum chamber after insertion of the cavity.

To address this concern we maintained the same basic mount design but Kevin Birnbaum did some research and substituted different materials for two components: the v-blocks and the glue connecting mirror substrates to v-blocks. Previously the v-blocks were aluminum pieces and the mirrors were glued to them with small dabs of Torr-Seal (the commonly used Varian catalog name for a UHV epoxy otherwise available as Dexter Hysol 1-C). According to manufacturer specifications, Torr-Seal sets to 90% hardness in 24 hours at room temperature. Complete cure is specified in one hour at 82°C or three days at room temperature. Our cavity construction method takes place entirely at room temperature. During a heating and cooling cycle, then, two dangers arise. First, the dabs of Torr-Seal may asymptotically approach complete hardness at room temperature but in fact “set” completely for the first time during bakeout, reaching new hardness and stress that persist after cooldown. Second, differential expansion of the mirror substrates, epoxy, and v-blocks may cause the components to pull away from one another and result in residual unrelieved stress after the temperature cycle is complete.

We replaced the aluminum v-blocks with identical pieces constructed from BK7 glass, the same material as the mirror substrates themselves. Kevin then spent considerable effort identifying an epoxy which would: (1) be UHV compatible, (2) set rigidly at room temperature, and (3) match thermal expansion properties as nearly as possible with BK7. A guide in these investigations was information from the telecommunications industry, where fiber and optical components must be attached in an industrial process that ensures robustness to *in situ* temperature variations over periods of years. In the end we employed Master Bond EP30LTEND for gluing of mirror substrates to v-blocks. The epoxy is still applied in two small dabs (one on either side) near the back end of the mirror (as far as possible from the mirror surface). This modified mount design caused some improvement, not in initial cavity

birefringence, but in thermal cycling properties, such that a completed physics cavity *may* now be baked gently. The baking tolerance of the overall mount is now set by length considerations and the PZT's (see Section 6.3.3) rather than by birefringence. Reducing the birefringence below the current value ( $\lesssim 1\%$  conversion of off-axis input linear polarization to circular) would involve a drastically different mounting scheme or the use of less glue. However, gluing rigidity is also a primary requirement for cavity length stability, so that further reductions in that area are not feasible for our experiments.

### 6.3.2 Specifically Chosen Cavity Length

For the first time we built a cavity with a fixed target length in mind, i.e., with the desire to have it a certain number of half-wavelengths and not one more or one fewer. Operationally this process involved a certain amount of gluing a cavity and adjusting the length based on how we thought the glue-setting process would pull it after it was too late to actively adjust any more. In other words, it was a procedure with some trial and error involved in hitting the correct length, even with the  $> 1$  FSR tuning range provided by our PZT's as discussed in Section 6.3.3. The motivation for a specific target length was to have the option of eventually including a FORT at (or near) the “magic wavelength” as discussed in [99, 19] and currently pursued experimentally in [52]. At this wavelength the AC Stark shift associated with a FORT actually shifts both the  $6S_{1/2}$  and  $6P_{3/2}$  states *down*, by approximately the same amount, so that roughly speaking a FORT is transparent to cavity QED probing under these conditions. The magic wavelength depends on FORT polarization, ranging from 923 nm for  $\sigma_-$  light to 952 nm for  $\sigma_+$ . A linear FORT – desirable because of its greater stability to polarization errors – has a magic wavelength of 935 to 936 nm, depending on which  $(F', m'_F)$  level we consider for the  $6P_{3/2}$  excited state. For a cavity only 10  $\mu\text{m}$  long, 935 nm is only about two FSR's away from 852; if one wants a cavity QED field and a magic-wavelength FORT to be simultaneously resonant in the cavity, cavity length *must* be set to an exact number of half-wavelengths.

Table 6.2 gives a chart of cavity lengths and corresponding resonant wavelengths for the mirrors used in our experiment. The choice of mirrors is important because mirror coatings have dispersion that causes the FSR to deviate from  $c/2l$ . Instead, successive resonant wavelengths are calculated from the detailed coating model presented in [18, 19].

$l_{eff} = 8.4 \mu m$ ( $l_{phys} = 18(\lambda/2)$ )	811.2 nm	852.359 nm	897.8 nm	945.4 nm
$l_{eff} = 8.8 \mu m$ ( $l_{phys} = 19(\lambda/2)$ )	813.1 nm	852.359 nm	895.5 nm	941.1 nm
$l_{eff} = 9.2 \mu m$ ( $l_{phys} = 20(\lambda/2)$ )	814.8 nm	852.359 nm	893.5 nm	937.1 nm
$l_{eff} = 9.6 \mu m$ ( $l_{phys} = 21(\lambda/2)$ )	816.4 nm	852.359 nm	891.6 nm	933.3 nm
$l_{eff} = 10.1 \mu m$ ( $l_{phys} = 22(\lambda/2)$ )	817.8 nm	852.359 nm	889.9 nm	929.8 nm

Table 6.2: Resonant wavelengths for short physics cavities (T95 mirrors). Physical cavity length is given in units of  $\lambda/2$  where  $\lambda = 852.359$  nm is the wavelength of the Cesium transition used for cavity QED.

Thus for a linear FORT in a  $\approx 10 \mu m$  cavity, geometry forces us to choose between wavelengths of 933 nm and 937 nm. Though neither wavelength gives us exactly equal AC Stark shifts for ground and excited states, both still allow negative AC Stark shifts for the two states. We see from Figure 3.2 that the  $6P_{3/2}$  state participates in transitions to higher-lying states at 917 nm and at 921 nm, so its AC Stark shift varies more rapidly with wavelength below 935 nm than above it. For this reason we choose to target a FORT at 937 nm, giving us a design cavity length of  $l_{eff} = 9.2 \mu m$  (set off by double bars in the table). The distinction between  $l_{eff}$  and  $l_{phys}$  need not concern us until Chapter 7;  $l_{eff}$  is the length we measure in the lab while aligning and building a cavity, and has been quoted as the length  $l$  for the cavities discussed so far.

Note that, if another nearby longitudinal mode is to be used for a cavity locking beam, 814.8 nm is the clear choice. Only 814.8 nm and 893.5 nm fall well within the mirror coating curve, assuring good cavity finesse and a narrow line for locking. The 893.5 nm mode must be avoided because of the  $6S_{1/2} \rightarrow 6P_{1/2}$  transition in atomic Cesium at 894 nm.

### 6.3.3 The Shear Mode PZT's

The active element in the cavity mount system for this experiment, as for the atom-cavity microscope, is a shear mode piezoelectric transducer (PZT) from Staveley Sensor. Each cavity mirror/v-block unit is glued to its own shear mode PZT, with the two PZT's oppositely directed so positive voltage on each acts to lengthen the cavity. The PZT's are made of a lead zirconate titanate material known as EBL3, and we obtain them in 1" by 1" sheets of thickness 0.020" (20 mil). In the construction of a cavity, these sheets are scored and cleaved to produce the individual pieces we use, which are approximately 1/2" long by 1/4" wide (and still 20 mil thick). Each PZT is bonded to the main mount piece with electrically conductive epoxy, spread over the entire bottom surface of the PZT and clamped down aggressively while drying since a good bond is essential for maximum mechanical stability in the system. A v-block is glued to the top surface of the PZT with Torr-seal. The PZT's are driven by applying voltages to the top surface of one or both PZT's, while they share a common ground through the cavity mounting piece.

The shear mode PZT's were a vast improvement over the previous design (cylindrical piezo within the mount) in terms of mechanical stability; the mounting system with a large cylindrical PZT exhibited a forest of mechanical resonances at only a few kHz, where we now obtain a lowest mechanical resonance of 50-60 kHz with the current design. However, there are numerous characteristics which might well be improved upon in a future design. Toward that end, I take some space here to present some advantages and disadvantages of the present design and of the piezos in particular. The chief overall design considerations are vacuum performance (including bakeability), length tuning range, and stability; as can easily be imagined, the latter two considerations are often at war with one another.

From a vacuum pressure point of view, the weak link in the mounting chain ought to be the electrically conductive epoxy, which is only rated by the manufacturer for use at  $10^{-3}$  torr. However, we have had no noticeable difficulty with this component over years of use both in this design and in the old one. Either the manufacturer's

rating is extremely conservative, or we simply benefit from the fact that we use the epoxy only in small quantities and in a setting where an extremely small surface area of it is exposed.

A bigger limitation is the relatively low baking temperature set by the piezo material itself. EBL3 is a Staveley material very similar in properties to some other common materials, e.g., PZT-5H, EC-76, and Navy Type VI. One less-than-ideal characteristic is its unusually low Curie temperature, 190°C. Because of this very low Curie temperature and our observations of stability problems after baking of mounts, we now bake these elements at no more than a few degrees above 100°C; even this may be a bit aggressive for this material. Most other EBL types have much higher Curie temperatures ( $\approx 300^\circ\text{C}$  is common), and should perhaps be considered in future cavity mounts for this reason.

The main attractive feature of shear mode PZT's, and EBL3 in particular, is the large cavity length tuning range that they provide as compared with other flat PZT's. Given that the flat, glued-down piezo paradigm is helpful for mechanical stability, the challenge is then to assure final length adjustability over at least one free spectral range so that the finished cavity can always be tuned to the Cesium D2 resonance. This corresponds to a length range of at least 426 nm to be obtained from some reasonable voltage applied to one or both piezos. For the shearing mode of displacement we are using, the directly relevant property is the “d-constant”  $d_{15}$ , which describes shear displacement between top and bottom surfaces as a function of the voltage between them. EBL3 is quoted as having  $d_{15} = 730 \cdot 10^{-12} \text{ m/V}$ , which is the same order of magnitude as related materials but at the upper end of the range. Since the recommended maximum DC applied voltage for the material is 10 V/mil or 200 V, it seems marginal that even the combined effect of two piezos should give us our desired tuning range.

In practice, however, we see displacements well above this specified value; in fact, in the current physics cavity we tune over one free spectral range of 426 nm with a voltage of zero to about 250 V, suggesting  $d_{15} = 1,700 \cdot 10^{-12} \text{ m/V}$  or more than twice the nominal value. Some of this tuning range may be related to hysteretic effects we

observe in the piezo, and some may in fact be due to even our gentle baking procedure. While the generous range is in many ways a pleasant surprise, the discrepancy most likely indicates some unintended alteration of the material properties which may have other, less benign consequences. One possible choice in future designs might be to resign ourselves to high voltages and obtain the requisite tuning range with a different material of lower  $d_{15}$  but larger allowed voltage.

A final consideration is the frequency of the lowest mechanical resonance in the system, and the way in which this all-important quantity is tied to the choice of PZT. Technical noise on cavity transmission signals is substantially due to electrically excited mechanical resonance of the cavity mounting structure. The piezo itself has a native resonant frequency  $\nu_0$  set by its thickness and by the material's "transverse frequency constant," which for EBL3 is 1105 Hz·m. This implies  $\nu_0 = 2.2$  MHz for the elements we use. For a piezo (spring) of mass  $m$  mechanically loaded with a mass  $M_L \gg m$ , the overall resonant frequency becomes  $\nu = \nu_0 \sqrt{\frac{m/3}{m/3 + M_L}}$ . Thus a loading mass of  $M_L = 1600(m/3)$  would bring the 2.2 MHz resonance down to the 50 kHz frequency we observe. In fact, however, the mirrors and v-blocks constitute a load only a few times more massive than the piezos themselves, so the predicted resonance is still well above what we observe. Thus we see that other spring constants are in action and it remains crucial to push the resonance as high and small as possible by rigidly attaching the mount elements and minimizing the height of the mirrors above the PZT's themselves to fight tuning-fork effects in the mount. The observed importance of rigid gluing in ensuring a high resonance frequency, as mentioned earlier, confirms that the native resonance of the loaded PZT is not yet the biggest issue.

### 6.3.4 Length Variation with Magnetic Field

The current physics cavity was installed in the vacuum chamber, the chamber was closed and pumped down, MOT coils and optics were built up around the chamber, and Cesium was introduced. The first time MOT's and cavity lock were operated simultaneously, we encountered a completely unexpected (and, needless to say, un-

welcome) variation of the cavity length with applied magnetic field. This effect had not been seen in previous cavities. The lack of a corresponding voltage jump on the PZT's eliminated the hypothesis of PZT shearing in response to the field. Instead the effect suggested the presence of a magnetic material in the cavity mount or somewhere nearby where the mechanical stress could be transmitted to the cavity.

After considerable hunting for the source of the effect, I picked up a spare cavity mounting block, applied an external magnetic field, and measured with a Gaussmeter an unmistakable induced field from the mounting piece itself. The explanation became simple. Hoping to ensure good vacuum pressure in the cavity region, and concerned about oxidation of the copper mount over the several days between cleaning of the piece and insertion of the finished cavity in the vacuum chamber, we had taken the protective measure of sending the copper mount pieces to be *gold-plated* before cavity construction. Unfortunately we were completely ignorant of the standard gold-plating process for copper, which involves application of a thin coating of *nickel* between the copper substrate and the gold top layer [104]. Thus our cavity mount piece itself is magnetic; applied fields induce magnetization in the nickel layer, force on the mount, and a jump in length of the cavity itself.

With this fact established, future mount construction can be altered in one tiny way; gold-plating can be specified without the nickel-plating step in the process. The chief purpose of the nickel layer is to prevent gradual diffusion of the gold into the copper substrate, an effect which is completely unimportant in our application. However, with our cavity already assembled, in UHV, and with Cesium and working MOT's around it, we chose to proceed with it in our experiment and compensate for the length jump rather than starting over with a new cycle of building up cavity, chamber, and optics.

The measured effect consists of a cavity length jump of  $4 \text{ \AA}$  when the lower MOT main anti-Helmholtz coils are turned on. When the coils are switched off, the cavity returns to its original length with remarkable accuracy, at the level of a linewidth. Nevertheless, this length jump is as rapid as the field switching and is huge compared to a linewidth ( $\approx 10 \text{ fm}$ ); it requires an applied voltage of 250 mV to the PZT to

compensate for the length change. The cavity lock, with gain designed to deal with small-amplitude vibrations and integration to deal with slow drifts, cannot possibly follow this jump during lower MOT loading or recover the lock quickly after the MOT is turned off. Thus the cavity locking circuit was modified to include a magnetic field compensator which directly samples the current in the main lower MOT coils and feeds that signal forward to send a corresponding additional voltage to the PZT. With this modification, the cavity length lock is still lost transiently at the switching of the MOT coils, but recovers fully in less than 5 ms after switching. Since atoms do not arrive in the cavity region until much later (after sub-Doppler cooling and a 3-mm drop), the cavity is amply prepared for atom-trapping by the time transits occur.

A second concern, however, is the lingering presence of the induced magnetic field of the mount itself and how it might alter the atom-cavity interaction by shifting the atomic levels. I have put some bounds on this effect by using the spare cavity mount to measure the size of the induced field at the cavity position. In the experiment, the top face of the mount sits at the center of the antiHelmholtz coils (in three dimensions) and extends  $\pm 1.6$  cm along the main coil axis. Given a field gradient of 16 G/cm along the main axis, we can use an applied field of 25 G to approximate the situation. Using a Gaussmeter and a permanent magnet, I applied this field to the cavity mount and subsequently measured an induced field of 0.1 Gauss (vertical) at the position of the cavity mode. This induced field would cause precession between  $m_F$  levels as otherwise defined by the circularly polarized cavity probe.

For magnetic fields small enough to be perturbative relative to hyperfine splittings, we are in the regime of the anomalous Zeeman effect, and levels are shifted by  $\Delta E_{|F m_F\rangle} = \mu_B g_F m_F B$ . Here  $\mu_B = h \cdot 1.40$  MHz/G is the Bohr magneton, and  $g_F$  is the hyperfine Landé  $g$ -factor. For  $6S_{1/2}$  and  $6P_{3/2}$  we have  $g_F = \frac{1}{4}$  and  $\frac{2}{5}$ , respectively [74]. Thus we estimate Zeeman shifts of  $\approx m_F \cdot 0.035$  MHz for the ground state and  $\approx m'_F \cdot 0.056$  MHz for the excited state. These Zeeman shifts between  $m_F$  levels as defined by the vertical magnetic field correspond to precession between  $m_F$  levels in the orthogonal basis defined by the circularly polarized cavity QED probe. The rate

of precession can be estimated as  $\approx 0.05 \text{ MHz} \cdot m_F$ , small compared with the scattering rate between field and probe with one photon in the cavity, but not vanishingly small and certainly disturbing from the point of view of future FORT experiments in this cavity.

On the other hand, the measurement described above is certainly an overestimate of the mount-induced field at the cavity position. In the actual experiment the mount is not magnetized by a constant field, but by a gradient field with its zero at the mount center. Thus two mitigating factors should make the induced field significantly *less* than 0.1 Gauss at the cavity position. First, the two halves of the mount are oppositely magnetized (at least along the primary axis) by the gradient field. Second, the portions of the mount closest to the cavity are also those which see the smallest applied field. An improved diagnostic for the induced field would be to apply the actual quadrupole field to the test mount, turn off external fields, and measure the induced field at the cavity position in this setup.

## 6.4 Into the Digital Era

While the overall timing of the experiment is still controlled from Labview as in the atom-cavity microscope, data acquisition and triggering/feedback have been changed. The spectrum analyzer video output signal is sent to a Gage (CompuScope 1450) board for digitization and storage of the transmission data. The Gage board can acquire up to 50 megasamples per second, with 14-bit resolution. We digitize at only 1 MHz and acquire data during a 20 ms interval for each MOT drop. Triggering and feedback are now accomplished through the digital processing capabilities of an FPGA board. The motivations for this change lie in the implementation of active feedback algorithms, due both to near-term technical issues and to more basic properties of the servo loop, as discussed in the introduction to this chapter. We use a VirtexE DSP hardware accelerator board (GVA-290a), which incorporates four dedicated A/D and D/A channels as well as three Xilinx FPGA's (two fully configurable). The A/D and D/A conversion has a depth of 12 bits and a maximum rate of 100 megasamples per

second; the FPGA clock rate is 100 MHz.

The programming of a very similar device for use in a quantum optics experiment is discussed in detail in [97]. FPGA's are an attractive choice for inherently digital processing, and additionally excel at rapid digitization, lookup tables, and simple but fast on-chip logic producing output pulses conditioned on the input data stream. The incorporation of the FPGA in our experiment has been largely undertaken by Kevin Birnbaum. The function of the board in our experiment is to (a) digitize the signal from the spectrum analyzer video out, (b) convert it to units of intracavity  $|\langle a \rangle|^2$ , and (c) implement the triggering and feedback scheme of Chapter 5, whose chief computational elements are a lookup table converting  $|\langle a \rangle|^2$  to  $\rho$  and an FIR filter for estimating turning points of  $\rho$  (zeros of  $\dot{\rho}$ ).

## Chapter 7

# Fabry-Perot Cavities for Fun and Profit

### 7.1 REO/ATF Mirrors at the Current State of the Art

If the cavity is the heart of a cavity QED experiment, the highly reflective mirrors are the heart of the cavity. We obtain these mirrors from the group of Ramin Lalezari at Research Electro-Optics (REO) in Boulder, CO – or within the last year from the same individual in his new effort at Advanced Thin Films (ATF), also near Boulder. The substrates, currently BK7 glass or fused silica, are superpolished on front (HR) and back surfaces. A standard antireflection coating is applied to the back surface. The mirror surface is coated with a multilayer stack of dielectric materials so that coating layers have alternating high and low index of refraction; the layer thickness is  $\lambda_c/4$  for a coating centered at  $\lambda_c$ .

These coating techniques are capable of producing mirror transmission  $T$  at or below  $10^{-6}$  (1 ppm). However, current technology has yet to push mirror loss  $A$  below one to a few ppm. Thus cavity finesse in the range of  $F \approx 10^5$  to  $10^6$  constitute the current state of the art for high-reflectivity, low-loss mirrors and coatings. These mirrors are useful not only in cavity QED but in numerous other scientific applications that exploit the high sensitivity they offer [105]. Mirror absorption/scatter losses set a limit on  $F$  and are furthermore a hindrance to signal extraction when nonlinear

interactions are present. They are a critical limiting factor in the loss rate for present cavity QED systems; for the very short cavities used in these experiments, loss rates associated with A are usually similar in size to the atomic spontaneous emission rates. To build robust quantum computing/communications devices from cavity QED components, it will be necessary to improve the ratio of mirror transmission (useful information) to mirror losses (loss of coherence).

In addition to the ratio of transmission to loss, another significant consideration is the role of mirror dispersion in determining cavity properties. At the current very short cavity lengths (about 20 half-wavelengths of the optical field), it is important to consider that the standing-wave light field inside a cavity penetrates into the mirror coatings, giving a larger mode volume than would be otherwise expected from the physical distance between the mirror surfaces. When the micro-cavities are pushed to shorter lengths in the quest for greater interaction strengths, the leakage field into the mirror coatings will have a non-negligible effect on the cavity mode structure.

A detailed coating model of the current experimentally-employed mirrors is described in [18], and a manual on the cleaning and evaluation of these mirrors can be found in [19]. Mount design considerations were presented in Chapter 6. In this chapter I focus on optical, geometric, and cavity QED properties of the cavities themselves.

## 7.2 Birefringence Issues

One unavoidable consequence of using high-finesse optical cavities seems to be a nagging issue of cavity birefringence. In a nutshell, the problem is that with cavity finesse in the range of  $10^5 < F < 10^6$  or higher, any birefringent phase shift  $\delta$  per round trip is ultimately enhanced by the very large finesse.

A very quick computation calculates the splitting between cavity resonance frequencies ( $\nu_a, \nu_b$ ) for  $TEM_{00}$  modes of orthogonal linear polarizations. Assume  $\hat{a}$  acquires a phase shift  $\delta$  relative to  $\hat{b}$  on each round trip in the cavity. Then the resonance conditions for a given longitudinal mode imply  $\frac{2\pi}{\lambda_a}2l + \delta = \frac{2\pi}{\lambda_b}2l$  and so  $\frac{2\pi l}{c}(\nu_b - \nu_a) =$

$\frac{2\pi l}{c} \Delta\nu = \delta/2$ . Thus  $\Delta\nu = \frac{\delta}{2\pi} \frac{c}{2l}$  and substituting  $\frac{c}{2l} = FSR = (FWHM)(F)$ , we have the result

$$\frac{\Delta\nu}{FWHM} = \frac{\delta}{2\pi} F \quad (7.1)$$

for the birefringent splitting relative to the cavity width. Thus even phase shifts  $\delta \sim 10^{-7}$  are quite noticeable;  $\delta \sim 10^{-6}$ , for instance, will completely scramble circular polarization injected into an otherwise beautiful high-finesse cavity.

Notice an equivalent formulation of this result is that, if the cavity is resonant with one polarization, the other polarization is detuned  $\Delta\nu$  off its resonance. Thus any orthogonally polarized light that is transmitted gets a phase shift of  $\tan^{-1}(2 * \text{detuning}/FWHM)$  [106], i.e.,  $\theta = \tan^{-1}(\frac{2\Delta\nu}{FWHM}) = \tan^{-1}(\delta \frac{F}{\pi})$ . For small overall phase shifts  $\theta$ , this becomes  $\theta \approx \delta \frac{F}{\pi}$ , meaning the *single-pass* phase shift  $\delta/2$  is simply magnified by the standard cavity enhancement factor  $2F/\pi$ .

If the previous two paragraphs were a long way of saying that even a small phase shift  $\delta$  is evil, where does the evil arise? From a variety of circumstantial evidence over the years, the most likely culprit is stress-induced birefringence in the dielectric coating stack of the mirrors. This conjecture is discussed in Chapter 6 and in Christina Hood's thesis [19], but a short summary is that cavities tend to be more birefringent when the mirrors are glued or clamped down more firmly and/or at positions closer to the coated surface. Often they become birefringent when they are glued and then baked, a process that could induce stress on the coatings as glue hardens and pulls the mirrors. Additionally, I have some experience with 7.75 mm substrates which are clamped with a set screw close to the coated surface; cavities made from two of these tend to be least birefringent when the mirrors are well centered on each other and thus the mode stays away from the point of greatest stress.

Another, but weaker, candidate for our suspicions is some sort of polarization-dependent absorption, scattering, or reflectivity resulting from defects or irregularities of wavelength scale or smaller. These effects would lead to different cavity decay widths for orthogonal linear polarizations, but would only cause a peak splitting  $\Delta\nu$  if they altered the spatial mode profile and thus induced different Guoy phase shifts

for the modes (see, e.g., [106]). This possibility should be easy to distinguish from the stress hypothesis by comparing the peak splitting to the difference in peak width for the two cavity eigenpolarizations. The evidence indicates stress is to blame in all but one instance of cavity birefringence measured over six and a half years. Thus I will concentrate on the situation where  $\hat{a}$  and  $\hat{b}$  are birefringent axes with equal cavity linewidths.

There are many possible measures of birefringence, and any one will suffice for the purpose of comparing different cavities to one another. Care is essential, though, when relating different measurement methods, since the easiest few measurements fit together in simple yet not-so-simple ways. Much of the difficulty lies in the typical measurement process of scanning over the cavity resonance(s) and doing a polarization-sensitive measurement of transmitted peak height. This process is well-suited to a tabletop building/testing situation where the cavity length is not well stabilized. However, because the lineshape too is polarization sensitive, this measurement is not as clean and direct as one could hope. Here I have looked at the three or four measurements most common in our group over last few years, relating each of them to one another and to the underlying birefringent phase shift  $\delta$  per round trip.

The general technique for most measurements is depicted in Figure 7.1. The cavity length is scanned over the entire resonance profile; light is injected into the cavity after some set of polarization optics, transmitted through the cavity, and analyzed on some (different) set of output polarization optics plus a photodetector. For interpretation and the discussion that follows, we assume the time to scan over any resonance feature is itself much greater than the cavity buildup/ringdown time, so that the transmitted lineshape unambiguously reflects steady-state cavity transmission as a function of length.

- Perhaps the simplest way to measure a birefringence is to directly measure a peak splitting as a fraction of underlying peak width. This is simple if the peaks are well-resolved,  $\Delta\nu \gtrsim FWHM$ . A cavity linewidth is measured for on-axis linear input polarization, and a peak splitting is read directly off the same scan

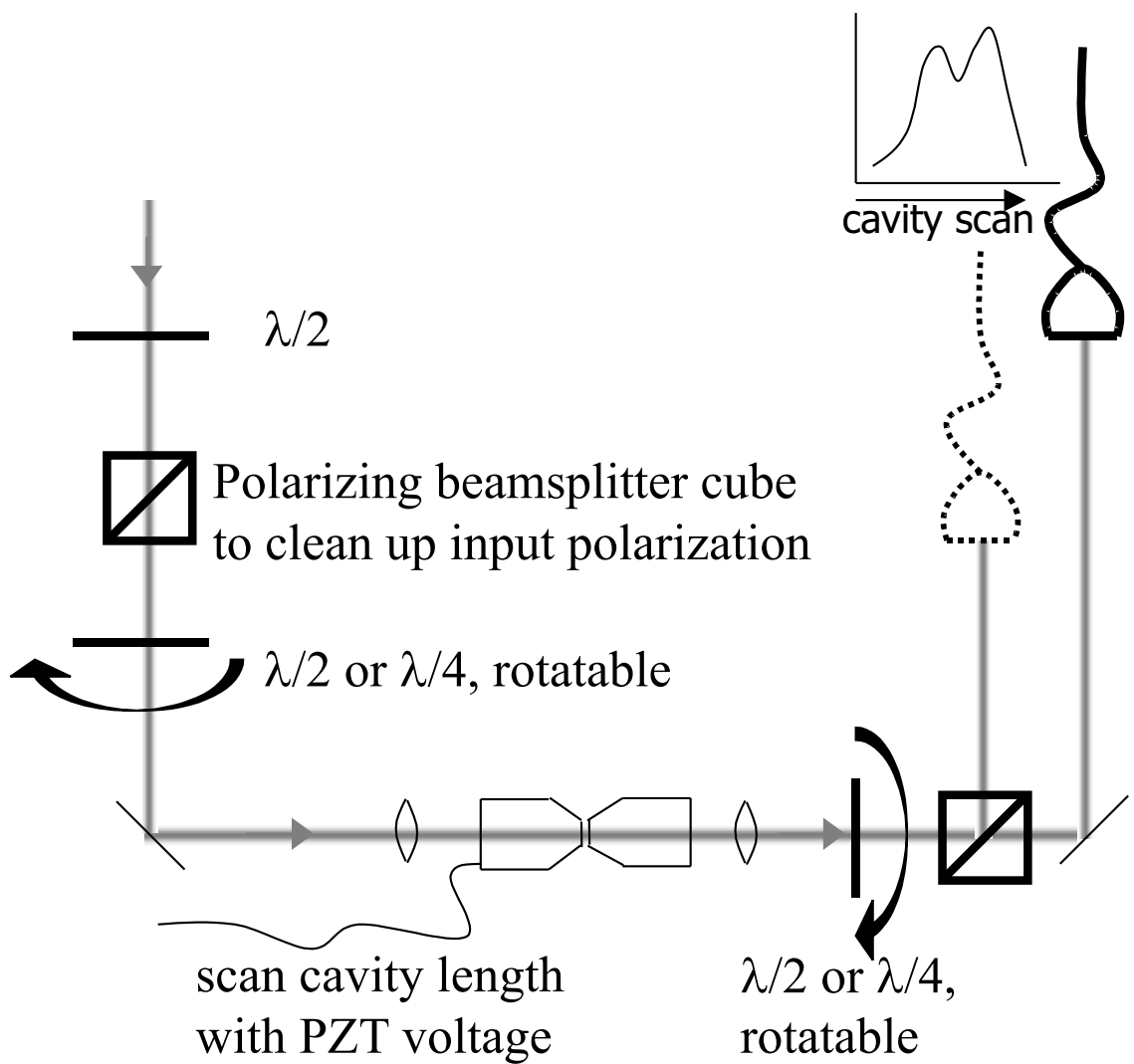


Figure 7.1: Setup for measurements of cavity birefringence

for circular input polarization (or off-axis linear input). If  $\Delta\nu \gg FWHM$ , the peak splitting is just  $\Delta\nu$ . If the splitting is smaller, some care must be taken in backing out  $\Delta\nu$  from the summed intensity transmission of the two modes.

For somewhat smaller birefringence (line not resolved into two peaks), one can measure the width separately on a birefringent axis and halfway between axes; peak splitting can always in theory be inferred from this. In practice, for splittings smaller than  $\Delta\nu \sim FWHM$ , direct peak splitting measurements may be hard to perform with any reasonable accuracy even though the birefringence is still large enough to be of interest.

- For small birefringence, a fairly simple measurement for diagnostic purposes is to scan the cavity, inject linearly polarized light, and detect it on a rotatable linear polarizer at the output (e.g., with a half waveplate and polarizing beam-splitter cube in front of the photodetector). On-axis or for no birefringence, the output light remains linear and one can rotate the output selector to transmit all of it or cancel it entirely (Figure 7.2(a)). Off-axis, though, the transmitted field of one polarization is phase shifted relative to the other; the overall output polarization is not linear but varies across the (split) cavity line. At overall line center, halfway between  $\nu_a$  and  $\nu_b$ , the polarizations have relative phase shift  $2\tan^{-1}(\Delta\nu/FWHM)$ . We inject light off-axis along  $(\hat{a} + \hat{b})/\sqrt{2}$ . For small enough birefringence, rotating an output linear polarizer gives maximum transmitted peak height at  $(\hat{a} + \hat{b})/\sqrt{2}$ , and minimum peak height at the orthogonal setting. (See Figure 7.2(b).) For larger birefringences, there will be maxima slightly away from the original axis due to peak splitting effects. Thus as long as the transmitted peak height achieves maximum and minimum values at orthogonal output analyzer settings ( $\theta_{out} = (\pi/4, 3\pi/4)$ , we can record the max and min heights and apply

$$Contrast_{lin} = \frac{\max - \min}{\max + \min} = \cos(2\tan^{-1}(\Delta\nu/FWHM)) = \frac{1 - (\Delta\nu/FWHM)^2}{1 + (\Delta\nu/FWHM)^2} \quad (7.2)$$

As soon as the strict  $\pi/2$  max/min condition is violated (Figure 7.2(c,d,e)), the formula above no longer applies.  $\Delta\nu$  can still be extracted, but it is best to go to a different measurement method anyway. Thus this measurement works nicely for  $\Delta\nu \lesssim 0.42(FWHM)$  or  $Contrast_{lin} \gtrsim 0.70$ .

- A similar measurement involves injecting circular polarization and measuring transmitted peak heights through an output linear polarizer. In this case there should be no dependence on analyzer setting in the perfect case, and contrast grows with birefringence. As long as contrast goes from max to min in  $\pi/2$  rotation of the output polarizer (Figure 7.3(a,b,c)), max and min occur at line center and we have

$$Contrast_{circ} = \frac{\max - \min}{\max + \min} = \sin(2\tan^{-1}(\Delta\nu/FWHM)) = \frac{2\Delta\nu/FWHM}{1 + (\Delta\nu/FWHM)^2}. \quad (7.3)$$

Just as with the previous measurement, this no longer holds when the  $\pi/2$  condition is violated (Figure 7.3(d,e)) and it is best to seek another measurement. However, it turns out this measurement holds a bit further, out to  $\Delta\nu \lesssim 0.64(FWHM)$  or  $Contrast_{circ} \lesssim 0.44$ .

- Other measurements are thus required for intermediate birefringence where the peaks are not yet clearly resolved but the two methods above already give dubious results. A nice method is to inject circular or off-axis linear polarization and measure the output transmission profile through a selector for the original polarization. When the birefringence is still too small to resolve the overall peaks, this polarization-sensitive measurement will show two resolved peaks from which the underlying splitting can be inferred (Figure 7.4).
- Yet another intermediate-splitting method, employed by Jason McKeever and Dan Stamper-Kurn, is to inject circular polarization, rotate a linear analyzer, and watch the transmission peak move around line center. They recorded a “maximum” peak height and the smaller peak height when the line was centered. A measurement of the splitting can be backed out of these quantities

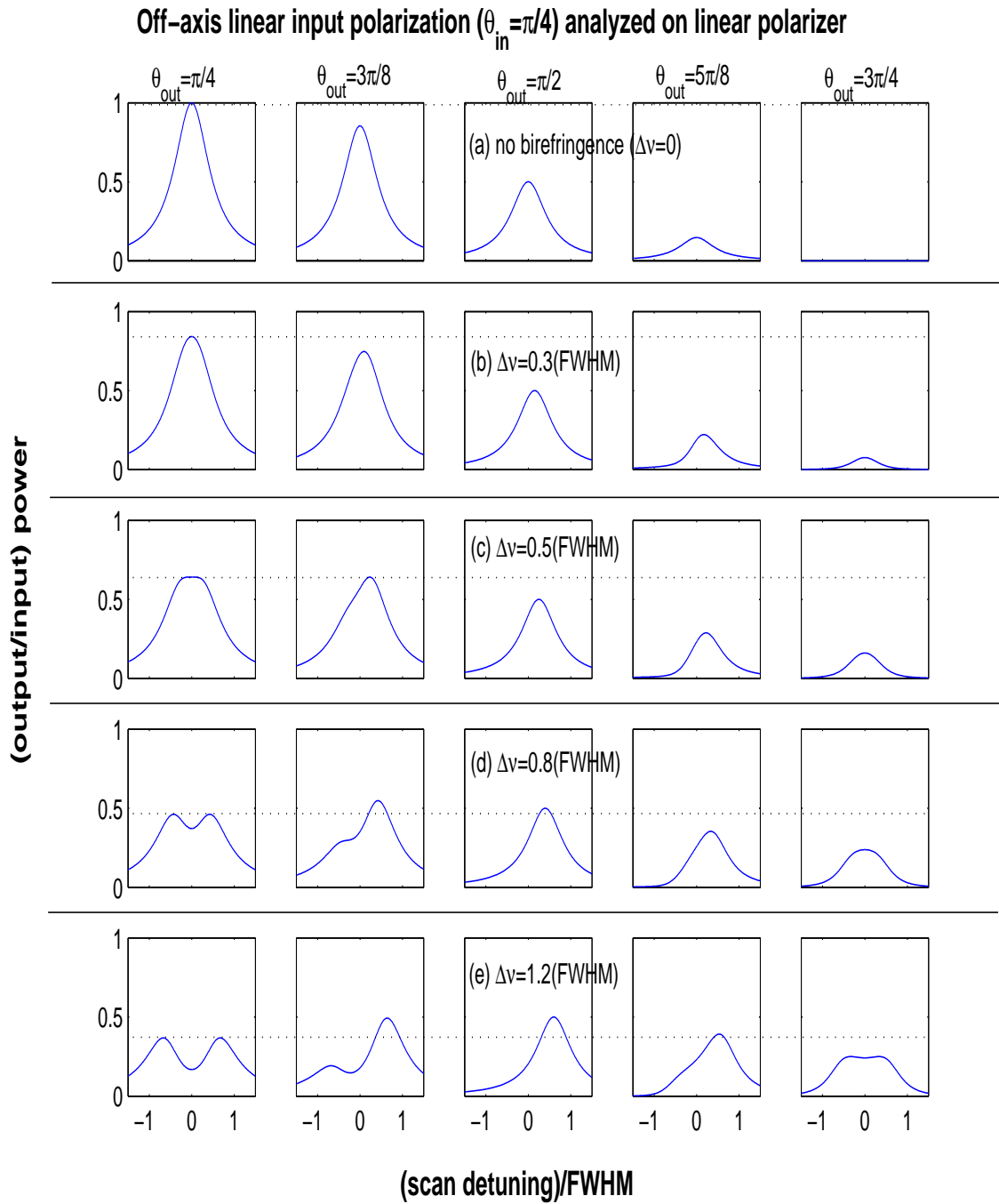


Figure 7.2: Calculated transmission of off-axis linear input light ( $\theta_{in} = \pi/4$ , or  $\frac{1}{\sqrt{2}}(\hat{a} + \hat{b})$ ) through cavity and output linear polarizer for five different values of cavity birefringence

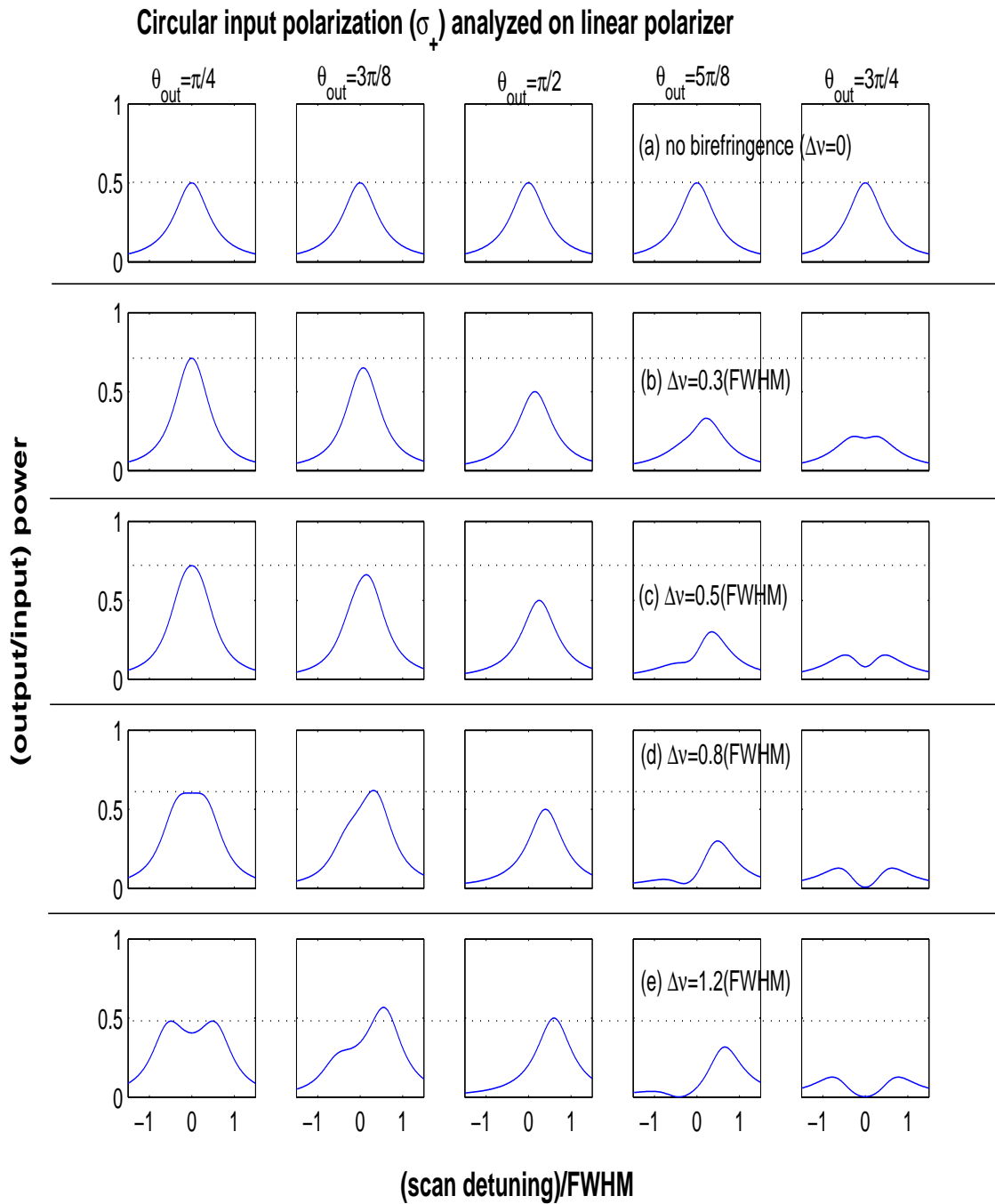


Figure 7.3: Calculated transmission of circular input light ( $\sigma_+$ , or  $\frac{1}{\sqrt{2}}(\hat{a} + i\hat{b})$ ) through cavity and output linear polarizer for five different values of cavity birefringence.

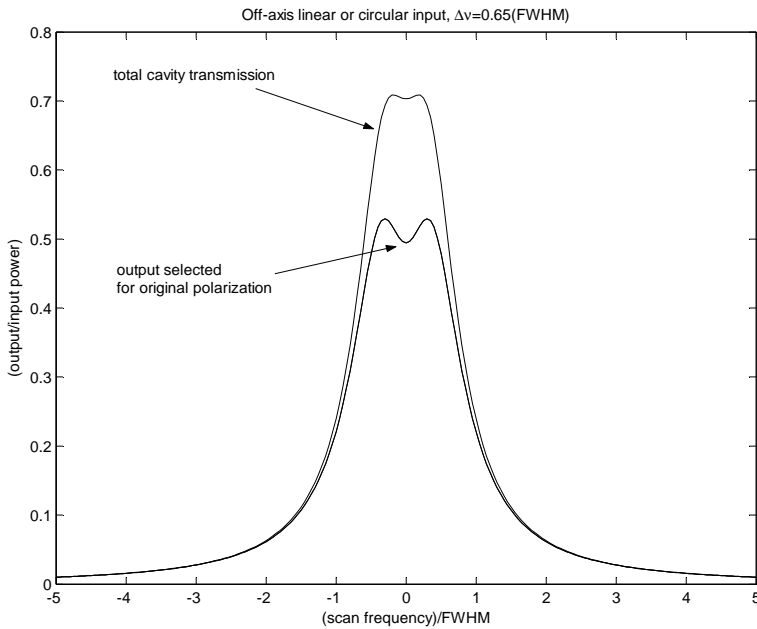


Figure 7.4: Preservation of input linear or circular polarization through birefringent cavity.

in the intermediate regime. However, the contrast on this measurement can be improved significantly by doing the same thing but with off-axis linear input light. Aside from the trouble needed to identify the axes, the linear input measurement is definitely superior. (Refer to Figures 7.2 and 7.3.)

- Often the “real” question from the operative point of view is: if we drive the cavity with a given polarization containing both  $\hat{a}$  and  $\hat{b}$ , how much does the actual intracavity polarization differ from our drive? This question is crucial for quantitatively predicting scattering rates and all atom-field interactions in the cavity. Unfortunately the question is not a simple one. It depends on the cavity detuning from resonance with each probe polarization. If the probe in question is the strongly-coupled cavity QED light, the polarization is also altered by the presence of an atom, since the atom itself shifts system resonances. Thus such a measurement can be performed for the empty cavity, but in reality any carefully set input polarization will shift as an atom enters the cavity and couples strongly to the light.

## 7.3 What Cavities Are Good for What?

I have attempted to collect in one place the information that must be considered when designing a new physics cavity (i.e., selecting mirror reflectivity, radius of curvature, cavity length, etc.). Much of this material is common knowledge, comes from simple geometry, or is written up elsewhere. Nevertheless, my hope is that by including the old with the new I can provide a single primary reference on this subject.

Several quite different physics considerations drive cavity design. In the experiments we have done for the past several years, atoms are dropped into the cavity from a MOT, so geometry determines the flux of atoms through the cavity mode and also their phase space distribution (particularly fall velocity and velocity along the cavity axis). Most likely, light besides the near-resonant probe is desired inside the cavity volume, so it is important to consider what longitudinal and transverse modes the cavity will support – as well as ease of coupling light in, detecting what comes out, or even focusing it through from the side. Finally, we come to the explicitly cavity-QED considerations; values of  $g_0$  and  $\kappa$  are certainly crucial, but for each experimental design the relevant figure of merit may be slightly different. I discuss important ratios and sensitivities for a couple of purposes to give a flavor.

I will devote separate subsections to “atom” factors, “light” factors, and “cavity QED” factors. First, however, I catalog basic relations of cavity geometry and mode structure that determine the quantities to be discussed throughout the later sections.

### 7.3.1 Basic Cavity Geometry and Mode Structure

We consider a Fabry-Perot cavity of length  $l$  made from spherical mirrors shown in Figure 7.5. Each mirror has radius of curvature  $R$ , diameter  $d$ , and transmission and losses ( $T, A$ ). If the two mirrors are different the subscripts (1, 2) are appended to each of these quantities. We treat lengths  $l \ll R$ .

The physical length of the cavity is  $l_{phys} = n\lambda/2$ . This is the separation between the two mirror surfaces at mode center. Measurements of cavity mode spacing and related quantities yield a somewhat different  $l_{eff}$  because of nonzero intensities in

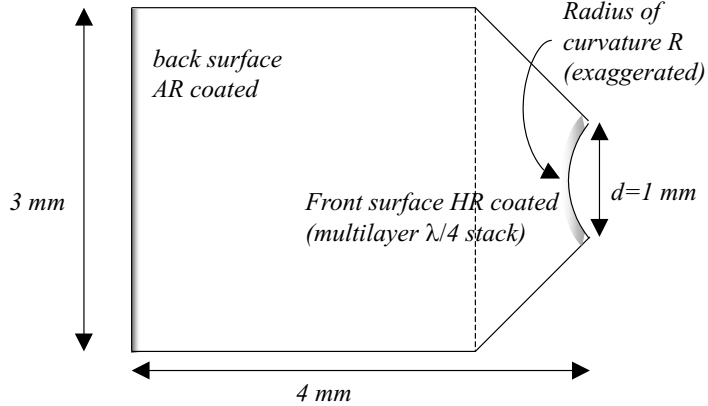


Figure 7.5: High reflectivity, low-loss mirrors for cavity QED; side view of cylinder-plus-cone substrate shape.

the first few layers of mirror coating. For mirrors in the T95 run, for example,  $l_{eff} = (n + 1.63)\lambda/2$ . More on this subject can be found in the next section and in [18].

Since the mirrors are spherical, there is an indentation from mirror edge to center, and thus the *gap* between mirror edges is less than  $l_{phys}$ . The indentation of each mirror is  $d^2/8R$ , giving

$$gap = l_{phys} - (d_1^2/8R_1 + d_2^2/8R_2). \quad (7.4)$$

The Gaussian waist of the cavity mode at wavelength  $\lambda$  is given by

$$w_0 = \left(\frac{l_{phys}}{2}(R - l_{phys}/2)(\lambda/\pi)^2\right)^{1/4} \approx \left(\frac{1}{2}\left(\frac{\lambda}{\pi}\right)^2 R l_{phys}\right)^{1/4}. \quad (7.5)$$

for a symmetric cavity. Note that the cavity mode volume therefore scales as  $w_0^2 l_{eff} \propto R^{1/2} l_{phys}^{1/2} l_{eff}$ . Generally  $l_{phys} \approx l_{eff} \approx l$ , so we may write this scaling as  $R^{1/2} l^{3/2}$ .

### 7.3.2 Atoms in the Cavity

Atoms are collected in a MOT as close as possible to the cavity, sub-Doppler cooled, and dropped onto the mirror gap. For fixed MOT properties and sub-Doppler temperature, cavity geometry will determine the flux of atoms through the cavity mode

volume and their position/velocity distribution. How does the flux of atoms through the mode depend on cavity geometry? We imagine the MOT dropping unobstructed to the top edge of the mirror surfaces, and begin our considerations then:

- 1) Initial  $x$  (axial position) must be within the gap, so atom flux  $\Phi$  scales as *gap*.
- 2) For each initial  $x$ , geometry allows

$$\frac{-l_{phys}/2 - x}{d/2} \leq v_x/v_z \leq \frac{l_{phys}/2 - x}{d/2} \quad (7.6)$$

in order for an atom to arrive at the cavity mode before hitting a mirror. The vertical velocity  $v_z$  is a fall velocity gained in the drop from MOT to cavity. For short cavities this restriction on  $v_x$  is much tighter than the thermal distribution from sub-Doppler cooling to a few  $\mu K$ . Thus the geometrical constraint chops out a flat piece of the thermal distribution, and  $\Phi$  scales as  $l_{phys}$  (or equivalently mode order  $n$ ) due to this effect.

- 3) The transverse extent of the target mode depends on the cavity waist. The vertical waist affects transit durations but is of little importance for atomic flux. This gives us a factor of  $w_0$  in  $\Phi$ .

These scalings can tell us how a proposed cavity compares with those already in action. Since the experiment of [51, 52] was the first in our group to incorporate a double-MOT design, we take it as a standard of achievable MOT-to-cavity transfer (with no cooling or catching in the cavity). From several sample data files, I counted a average number of 40 detectable transits per drop in that setup (referred to hereafter as “Lab 11” for the room in which it is located). The Lab 11 cavity has  $n = 103$ ,  $w_0 = 23.8 \mu m$ , and  $gap = 42.6 \mu m$ . In sum, therefore, we have

$$\Phi \simeq 40 \left( \frac{w_0}{23.8 \mu m} \right) \left( \frac{n}{103} \right) \left( \frac{gap}{42.6 \mu m} \right) \quad (7.7)$$

For example, I have calculated the ratio  $\Phi_{Lab11}/\Phi$  for several cavity designs we considered for the active-feedback experiment. Values in Table 7.1 are for mirrors of diameter  $d = 1$  mm and symmetric cavities (two identical mirrors). The current active-feedback cavity has length  $l_{phys} = 20(\lambda/2)$  and uses  $R = 10$  cm mirrors; more atoms in the initial cloud are therefore necessary to ensure  $\approx 1$  transit per drop.

<u>R=10 cm mirrors</u>	<u>R=5 cm mirrors</u>					
n (# $\lambda/2$ )	$w_0(\mu m)$	gap ( $\mu m$ )	$\Phi_{Lab11}/\Phi$	$w_0(\mu m)$	gap ( $\mu m$ )	$\Phi_{Lab11}/\Phi$
10	11.2	1.76	530	9.4	none	n/a
11	11.5	2.19	377	9.6	none	n/a
12	11.7	2.61	285	9.8	0.11	8073
13	11.9	3.04	222	10	0.54	1488
14	12.2	3.46	177	10.2	0.96	762
15	12.4	3.89	144	10.4	1.39	482
16	12.6	4.32	120	10.6	1.82	338
17	12.8	4.74	101	10.7	2.24	256
18	13.0	5.17	86	10.9	2.67	199
19	13.1	5.59	75	11.0	3.09	162
20	13.3	6.02	65	11.2	3.52	132
21	13.5	6.45	57	11.3	3.95	111
22	13.6	6.87	51	11.4	4.37	95
23	13.8	7.3	45	11.6	4.8	82
24	13.9	7.72	41	11.7	5.22	71
25	14.1	8.15	36	11.8	5.65	63

Table 7.1: Geometrical properties of cavities as length and mirror curvature are varied.

We keep in mind also that these gaps and fluxes are calculated based on perfect alignment of the cavity mirrors. In reality most cavities may be constructed with a slight relative tilt of the two mirrors, causing the gap to be even smaller at some places around the mirror circumference.

### 7.3.3 Light in the Cavity

Many aspects of light in a cavity were calculated in detail by Christina Hood and can be read about in her thesis [19]. As mentioned above, when the cavity supports a mode

at a given wavelength, some amount of light actually “lives” in the first few coating layers and this causes the cavity free spectral range to differ from naive expectations. The exact FSR is relevant when designing a cavity to support longitudinal modes at more than one specific wavelength. See the discussion of the active-feedback cavity length in Section 6.3.2 for some treatment of this issue.

For the active-feedback experiment we were constructing a cavity of length  $\approx 10 \mu\text{m}$ , and so chose  $l_{eff} = 9.2 \mu\text{m}$  to get a magic-wavelength FORT two FSR’s away. The two-FSR spacing is an attractive scenario because the FORT and probe standing waves overlap perfectly at cavity center, with overlap decreasing as we move away from the center and the standing waves get out of phase. The FORT and probe are completely out of phase halfway from the center and come back into phase at the mirrors (to achieve simultaneous resonance). Alternatively one could imagine the shortest possible cavity to support both cavity QED and the magic-wavelength FORT, with one FSR separating the two wavelengths. In this case the FORT and probe are non-overlapped at cavity center and come into register only at the ends of the cavity. For any future consideration of a cavity along these lines, I note here that the best length is  $l_{eff} = 4.5 \mu\text{m}$ , which allows a FORT at 936.6 nm one FSR away from 852.359 nm. For different mirror coatings these numbers will change, requiring a new coating model for accurate prediction.

For some purposes the transverse mode spacing of the cavity may also be relevant. Using light in a transverse mode is one way to break cylindrical symmetry of the atom-cavity coupling for purposes of tracking and/or cooling. Alternatively, measurement of transverse mode spacing is one proposed way of determining length for a very short cavity. Geometry (ignoring cavity birefringence but including the contribution of mirror dispersion effects) gives transverse mode spacing

$$\Delta\nu_t = \left(\frac{c}{2\pi l_{eff}}\right) * \cos^{-1}(1 - l_{eff}/R) \approx \frac{c}{\sqrt{2}\pi l_{eff}^{1/2} R^{1/2}} \quad (7.8)$$

for a symmetric cavity. Measurements I have done on test cavities indicate that this expression reflects reality very closely; cavity length measurement based on this

technique is discussed in the final section of this chapter.

One small but crucial matter is the coupling of light into and out of these cavity modes. A beam with  $\simeq 10 \mu m$  waist inside the cavity expands appreciably on its way through the mirror substrate. A minimal requirement for useful physics is that the beam must cleanly enter/exit the back surface of the substrate! In the “standard” cone mirror design, the back surface is 3 mm tall and 4 mm away from the cavity itself. Beam waist as a function of distance from focus is

$$w(r) = w_0 \sqrt{1 + \left(\frac{r\lambda}{\pi w_0^2}\right)^2} \quad (7.9)$$

and  $w_0$  is set by cavity length and mirror curvature as given above. Extra clearance should be given in case the cavity mode axis is not precisely aligned along the geometric axes of the substrate.

So far this has been a description of modes supported by the cavity, but I now digress to mention the possibility of focusing beams through the cavity from the side. This option can be useful for cooling beams (as in [51, 52]) or for the “classical” pulse in various logic proposals. However, it can become a difficult and even impossible feat as cavity length decreases towards the optical wavelength. Imagine a beam entering through the gap between 1mm diameter cavity mirrors, focused at the cavity axis, and exiting again at the other side. Referring to Equation 7.9, we see that for light of  $\lambda = 852 nm$ , the entering/exiting spot waist  $w(r = 0.5 mm)$  has a minimum value of  $16.5 \mu m$  achieved with focused waist  $w(0) = 12.0 \mu m$ . If we require that a “cleanly” passed beam must have  $w(0.5 mm) \leq gap$ , this gives a minimum cavity length of about  $33 \mu m$  if a side beam is to be used. At shorter cavity lengths light can be focused in and/or allowed to diffract through the cavity volume, but clean beams in and out are not a possibility. Smaller mirror diameter would relax this limit, but going below the current 1-mm diameter would require new efforts in mirror cleaning to obtain pristine central regions for the cavity mode with the rough and dirty edge region brought closer in.

### 7.3.4 Usefulness for Cavity QED

We can begin to assess a cavity's usefulness for cavity QED experiments by looking at relevant rates and at dimensionless parameters that tell us what atom-cavity physics looks like in a given cavity. The rate of coherent atom-cavity coupling is set by the parameter  $g_0$ , defined as half the single-photon Rabi frequency. The value of  $g_0$  is simply determined by the electric field strength associated with a single photon in the cavity mode, so  $g_0$  is inversely proportional to the square root of cavity mode volume. Expressing everything in mks units, we have (see, e.g., [27]):

$$\frac{g_0}{2\pi} = \left( \frac{3c\lambda^2\gamma_{||}}{2\pi^2 w_0^2 l_{eff}} \right)^{1/2} / 2\pi \quad (7.10)$$

where  $\gamma_{||} = 2\gamma_{\perp}$  as given in Chapter 3. This coherent exchange of excitation between atom and cavity must generally be compared with the cavity decay rate  $\kappa$  and the atomic decay rate  $\gamma_{\perp}$ . If an atom is moving within the cavity, these rates must also be compared with the rate for local coupling to change due to atomic motion; this is represented by  $1/\tau$  where  $\tau$  is a timescale for an atom to fall through the cavity mode or for a trapped atom to oscillate in the direction of interest.

Note that  $g_0$  depends on cavity geometry as

$$g_0 \propto w_0^{-1} l_{eff}^{-1/2} \propto R^{-1/4} l_{phys}^{-1/4} l_{eff}^{-1/2} \approx R^{-1/4} l^{-3/4} \quad (7.11)$$

where the last relation uses  $l_{eff} \approx l_{phys} \approx l$ . The cavity decay, on the other hand, scales as

$$\frac{\kappa}{2\pi} = \frac{1}{2} \frac{c/2l_{eff}}{Finesse} \propto l_{eff}^{-1}. \quad (7.12)$$

The timescale for atomic motion in general also depends on cavity geometry, but the specific dependence varies with the type of motion being considered.

A simplistic measure of cavity QED properties might be the number of coherent cycles per decay time, which would be estimated by the quantity  $g_0/\beta$  where  $\beta = \max[\kappa, \gamma, 1/\tau]$ . This quantity being much larger than unity is roughly speaking the criterion for strong coupling, the regime in which the atom-cavity physics has

signatures of quantum rather than semiclassical fields at work. However, within the realm of strong coupling there is room for a great deal of variation in what exact phenomena are present and which ones can be observed with good signal-to-noise.

Slightly more specific are the parameters known as the critical atom and photon numbers ( $N_0, m_0$ ). These parameters are discussed at length in Chapter 2. They represent the number of atoms necessary to significantly alter the cavity response and the number of photons necessary to significantly alter the atomic state. They scale as

$$N_0 = (2\kappa\gamma)/g_0^2 \propto R^{1/2}l^{1/2}, \quad m_0 = \gamma^2/2g_0^2 \propto R^{1/2}l^{3/2}. \quad (7.13)$$

Both critical parameters should be much less than unity for strong coupling.

Another parameter, the rate of optical information  $dI/dt$ , tries to address the question of detecting intracavity physics through measurements of cavity light output (cavity transmission). Roughly, the rate of optical information represents the rate at which transmitted light (or “missing” transmitted light) can give us information about the atom-cavity state. This quantity is also discussed in Chapter 2. The optical information rate scales as

$$dI/dt \sim g_0^2/\kappa \propto R^{-1/2}l^{-1/2}, \quad (7.14)$$

with optical information per atom or per motional cycle carrying an additional factor of the timescale  $\tau$ .

Whatever the physics or detection strategy, detection efficiency and signal-to-noise ratio will be determined by the ratio of mirror losses (absorption and scatter) to mirror transmission. Most parameters get more impressive as  $\kappa$  gets smaller, so since  $\kappa \sim (\text{losses} + \text{transmission})$  it is tempting to decrease transmission with ever-more-reflective mirror coatings. However, a given mirror fabrication process will have some minimum achievable loss per mirror (about 1ppm for current REO standards). Decreasing transmission to or below this mark will only result in slight  $\kappa$  decreases, and will greatly erode detection efficiencies as most of the escaping light will be scattered or absorbed rather than transmitted.

Another important consideration along these lines is the use of a two-sided (symmetric) or one-sided (one very good mirror, one more transmissive) cavity. A one-sided cavity offers the prospect of a truly unique, coherent output mode for the cavity. We envision a cavity with single-mirror transmissions ( $T_1, T_2$ ) and losses ( $A_1, A_2$ ). Cavities of the current generation have  $(T_1 = T_2) > (A_1 = A_2)$ , allowing cavity decay to send light out both cavity mirrors equally. A better situation for quantum communication and nonclassical light generation would instead be  $T_1 \gg (T_2, A_1, A_2)$ . To achieve this situation while remaining in the strong coupling regime, mirrors with very low transmission and losses are necessary, since one typically desires even  $T_1$  about 10 ppm or smaller. Alternatively, output from both sides of a two-sided cavity could be collected and, with some technical difficulty, coherently combined.

## 7.4 Signal-to-Noise for Atom Orbits

Clearly different figures of merit will apply to each experimental scheme, making different cavity designs suitable for different purposes. As one example, I present some calculations on the signal-to-noise ratio for observing trapped-atom orbits (as in the atom-cavity microscope) in different cavity geometries. As we will see, both intracavity dynamics and detection sensitivity are important factors, and the overall result is not necessarily an intuitively clear function of cavity parameters.

The goal of this set of calculations is to use one experimental paradigm as an example of position sensing considerations in different cavities. The cavities considered are actual cavities used in the group or, in the last two cases, slight variations on existing cavity designs. Cavity geometry and mirror properties set  $g_0$ ,  $\kappa$ , and  $w_0$ . To choose detunings, in each cavity we envision experimental conditions analogous to those in the single-photon triggered-trapping experiments we have already performed. Thus we measure  $|\langle a \rangle|^2$  for a probe beam detuned near the lower dressed state of a system where the cavity resonance is red of the atom resonance. The quantities we hold constant (using their values from the atom-cavity microscope) are (1) the cavity detuning from the atom as compared with the cavity width and (2) the probe

detuning *from the lower dressed state resonance* as compared with the cavity width, i.e.,

$$\Delta_{ca}/\kappa = -47/14.2 = -3.3 \quad (7.15)$$

$$\frac{\omega_p - \omega_{|-\rangle}}{\kappa} = \frac{\Delta_{pa} - (\frac{\Delta_{ca}}{2} - \sqrt{g_0^2 + \frac{\Delta_{ca}^2}{4}})}{\kappa} = \frac{-125 - (\frac{-47}{2} - \sqrt{110^2 + \frac{(-47)^2}{4}})}{14.2} = 0.77. \quad (7.16)$$

Then for each cavity I adjust the drive strength to maximize either: (1) the rate of “extra” photons to indicate the atom is present ( $\kappa(|\langle a \rangle|_{full}^2 - |\langle a \rangle|_{empty}^2)$ ) or (2) the detection bandwidth at which S/N=1 subject to shot noise,

$$B_{S/N=1} = \kappa \frac{(|\langle a \rangle|_{full}^2 - |\langle a \rangle|_{empty}^2)^2}{|\langle a \rangle|_{full}^2}, \quad (7.17)$$

or (3) the S/N over a radial oscillation period

$$(S/N)_{\tau_{osc}} = \sqrt{\kappa \tau_{osc}} \frac{|\langle a \rangle|_{full}^2 - |\langle a \rangle|_{empty}^2}{\sqrt{|\langle a \rangle|_{full}^2}}. \quad (7.18)$$

The results are shown in Table 7.2. In the table I also show the quantity  $g_0^2/\kappa$  for comparison; according to hand-waving arguments, the rate of extra photons should scale roughly with  $g_0^2/\kappa$ , as should the bandwidth for S/N=1. We can see only a rough correspondence, perhaps owing to the *ad hoc* nature of the detuning choices. Certainly as  $\kappa$  becomes roughly equal to the atomic decay  $\gamma_\perp/2\pi = 2.6$  MHz, our detuning choices related only to  $\kappa$  become somewhat inappropriate. More interesting is the ACM-like cavity in which  $\kappa$  stayed the same but  $g_0$  was increased by about 20%; sensing ability here clearly does not scale with  $g_0^2/\kappa$ . Evidently for the comparisons I have made here, not only  $g_0^2/\kappa$  but  $g_0$  itself (i.e., in relation to the constant  $\gamma_\perp$ ) is significant.

[In the calculations above I have assumed unit detection efficiency, since we are concerned here with signal-to-noise considerations driven by cavity properties and not by detection strategy. Furthermore, I have considered only the decay out one cavity mirror (by using rate  $\kappa$  rather than  $2\kappa$ ). Thus the relevant detection efficiency

cavity description	cavity ( $g_0/2\pi, \kappa/2\pi$ ), $w_0$	$(\Delta_{pa}/2\pi, \Delta_{ca}/2\pi)$
ACM	(110,14.2) MHz, 14.06 $\mu\text{m}$	(-125,-47) MHz
active-feedback	(130,17) MHz, 13.3 $\mu\text{m}$	(-148,-56) MHz
Lab 11 (FORT)	(32,4) MHz, 23.8 $\mu\text{m}$	(-37,-14) MHz
ACM but $l_{eff} = 5.8 \mu\text{m}$	(179,26.7) MHz, 11.7 $\mu\text{m}$	(-208,-88) MHz
ACM but $R = 5 \text{ cm}$ mirrors	(131,14.2) MHz, 11.8 $\mu\text{m}$	(-146,-47) MHz
$g_0^2/\kappa$	$\kappa( \langle a \rangle _{full}^2 -  \langle a \rangle _{empty}^2)$	$B_{S/N=1}$
$5.3 \cdot 10^9/\text{s}$	$2.7 \cdot 10^8/\text{s}$	15.36 MHz
$6.2 \cdot 10^9/\text{s}$	$3.3 \cdot 10^8/\text{s}$	18.7 MHz
$1.6 \cdot 10^9/\text{s}$	$0.60 \cdot 10^8/\text{s}$	3.10 MHz
$7.5 \cdot 10^9/\text{s}$	$5.7 \cdot 10^8/\text{s}$	32.3 MHz
$7.4 \cdot 10^9/\text{s}$	$2.7 \cdot 10^8/\text{s}$	14.5 MHz
		$S/N_{\tau_{osc}}$
		83
		86
		70
		97
		71

Table 7.2: Sensitivity for atomic motion in different cavities (detunings chosen for ACM-like trapping).

is the quantity  $\eta'$  of the discussion in Section 3.7. To include the effect of detection efficiency,  $B_{S/N=1}$  must be multiplied by  $\eta'$  and  $(S/N)_{\tau_{osc}}$  must be multiplied by  $\sqrt{\eta'}$ .]

One reason for the lack of  $g_0^2/\kappa$  scaling in Table 7.2 is an inappropriate choice of quantities held constant. The condition of constant  $\Delta_{ca}$  in Equation 7.15, in particular, helps in maintaining a deep trapping potential but has no particular relevance to sensing. For sensing, it is more reasonable to place the probe a fixed number of linewidths away from the empty cavity, so

$$\frac{\omega_c - \omega_p}{\kappa} = 78/14.2 = 5.5 \quad (7.19)$$

becomes the first condition to apply. To determine  $\omega_a$ , we can then require that the system's lower dressed state coincide with the probe frequency, giving

$$\omega_{|- \rangle} - \omega_p = \left( \frac{\omega_a + \omega_c}{2} - \sqrt{g_0^2 + \frac{\Delta_{ca}^2}{4}} \right) - \omega_p = 0. \quad (7.20)$$

Using these criteria we obtain detunings and sensitivities as shown in Table 7.3 for the same example cavities.

We now see a sensitivity for atom detection that tracks  $g_0^2/\kappa$  much more closely,

cavity description	cavity ( $g_0/2\pi, \kappa/2\pi$ ), $w_0$	$(\Delta_{pa}/2\pi, \Delta_{ca}/2\pi)$
ACM	(110,14.2) MHz, 14.06 $\mu\text{m}$	(-151,-71) MHz
active-feedback	(130,17) MHz, 13.3 $\mu\text{m}$	(-181,-87.6) MHz
Lab 11 (FORT)	(32,4) MHz, 23.8 $\mu\text{m}$	(-45.5,-23) MHz
ACM but $l_{eff} = 5.8 \mu\text{m}$	(179,26.7) MHz, 11.7 $\mu\text{m}$	(-218,-71) MHz
ACM but $R = 5 \text{ cm}$ mirrors	(131,14.2) MHz, 11.8 $\mu\text{m}$	(-221,-143) MHz
$g_0^2/\kappa$	$\kappa( \langle a \rangle _{full}^2 -  \langle a \rangle _{empty}^2)$	$B_{S/N=1}$
$5.3 \cdot 10^9/\text{s}$	$2.65 \cdot 10^8/\text{s}$	14.5 MHz
$6.2 \cdot 10^9/\text{s}$	$3.28 \cdot 10^8/\text{s}$	17.9 MHz
$1.6 \cdot 10^9/\text{s}$	$0.63 \cdot 10^8/\text{s}$	3.2 MHz
$7.5 \cdot 10^9/\text{s}$	$4.67 \cdot 10^8/\text{s}$	23.7 MHz
$7.4 \cdot 10^9/\text{s}$	$3.34 \cdot 10^8/\text{s}$	19.4 MHz
		$S/N_{\tau_{osc}}$
		82
		85
		73
		85
		83

Table 7.3: Sensitivity for atomic motion in different cavities (detunings compatible with trapping but chosen for sensing).

though certainly the simple scaling is not reflected perfectly (Figure 7.6). Signal-to-noise over a motional timescale, however, hardly varies at all for the cavities considered here; as the sensitivity for atomic motion improves, the motional timescale for atom-cavity orbits becomes shorter as well.

In general these extra photon rates and S/N ratios are optimized for much higher driving than the fractional photon in the cavity that we use in experiments. Instead, the largest sensitivities occur with one to a few photons in the cavity. A simple estimate shows we should expect this. As in the on-resonance case described in Chapter 2, we argue that the best effect should be seen when the field approximately saturates the atomic response. However, the field is now detuned from the atomic resonance by  $\Delta_{pa} \gg \gamma_\perp$ . Thus to saturate the atom the cavity must hold not  $m_0 = \gamma_\perp^2/2g_0^2$  photons but  $m_0(\Delta_{pa}^2/\gamma_\perp^2) = \Delta_{pa}^2/2g_0^2 \approx 1$  photons.

Why do we not go to ten times more driving in the experiment? The answer lies in the fact that Tables 7.2 and 7.3 contain no information about momentum diffusion rates for the atom. We have seen already in Chapter 4 that the semiclassical momentum diffusion is much larger than the fully-quantum calculation for the atom-cavity microscope. As we go to stronger drive strength the dynamics become more semiclassical with respect to the cavity field, and correspondingly the momentum

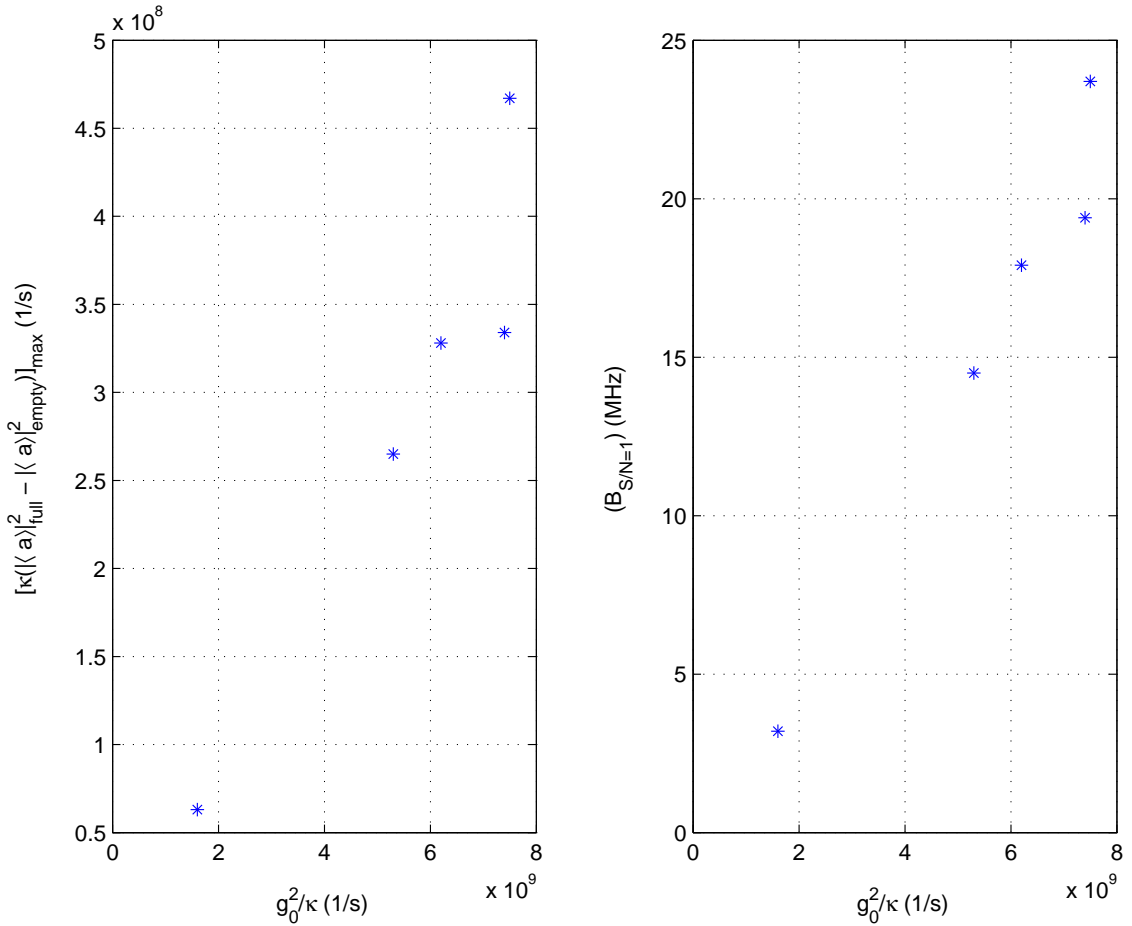


Figure 7.6: Sensitivity for an atom in the cavity as a function of optical information rate (detunings of Table 7.3).

diffusion over oscillation timescales – and over sensing timescales – becomes larger. Thus one has a better bandwidth for sensing atomic position, but the motion itself heats up much faster and there is no quasi-conservative motion to observe.

In an experiment where trapping is provided by some means other than the cavity field, motional timescales are decoupled from the choice of probe settings, in which case the relevant sensitivities are those which do not explicitly include  $\tau_{osc}$ .

#### 7.4.1 Connection to Position Sensitivity in the ACM

Before leaving the subject of signal-to-noise for detecting trapped atoms, I briefly connect the results of the preceding section with the discussion of position sensitivity

in Chapter 4. In Section 4.3 a hand-waving argument predicted a position sensitivity of  $1.0 \text{ nm}/\sqrt{\text{Hz}}$ , notably at odds with the observed sensitivity of  $20 \text{ nm}/\sqrt{\text{Hz}}$ . We are now in a position to revisit this estimate and resolve the discrepancy.

The predicted sensitivity arose from an estimate which essentially quoted a rate  $g_0^2/\kappa$  for information on an atom's presence in (or absence from) the cavity mode. This gave sensitivity  $S_\rho = \sqrt{\frac{1}{2\eta}} \frac{w_0}{\sqrt{g_0^2/\kappa}} \sqrt{B}$ . However, we now have an actual result, from solution of the master equation, for signal-to-noise via our detection method. Thus we may instead observe that, for the atom-cavity microscope, we cannot do better than  $S/N = 1$  for resolving an atom's presence in bandwidth  $B = 15.36 \text{ MHz}$ . Furthermore, the quantity  $dg/d\rho$  estimated as  $g_0/w_0$  in Section 4.3 can be more carefully evaluated, yielding its actual maximum value of  $\frac{g_0}{w_0} \sqrt{\frac{2}{e}}$ .

Thus we now expect  $S_\rho \geq \sqrt{\frac{1}{2\eta'}} \frac{w_0 \sqrt{e/2}}{\sqrt{15.36 \text{ MHz}}} = 5.9 \text{ nm}/\sqrt{\text{Hz}}$ . If we allow for a factor of  $\sqrt{2}$  degradation in sensitivity due to technical noise, this estimate becomes  $8.4 \text{ nm}/\sqrt{\text{Hz}}$ , approaching our measured sensitivity quite reasonably. The remaining discrepancy corresponds to the fact that our probe strength is below the optimal level for sensing, as discussed above.

## 7.5 Measuring Lengths of Very Short Cavities

In constructing very short cavities, down to the smallest possible Fabry-Perot of length  $\lambda/2$ , new methods of cavity length measurement will be necessary. We currently measure cavity lengths by tuning a Ti:Sapph laser through a full free spectral range of the cavity, thus finding  $\lambda_1$  and  $\lambda_2$  for which  $l_{eff} = n(\lambda_1/2) = (n+1)(\lambda_2/2)$ . Note  $n$  will not be an integer due to mirror dispersion as discussed above. For our current physics cavity of length  $l_{eff} = 9.2 \mu\text{m}$ , the free spectral range is already 40 nm, and one can see that for very short cavities the free spectral range no longer fits inside the  $\sim 150 \text{ nm}$  high-transmission region of the mirror coating curve. Alternative length measurements must be employed.

One possibility is to use the transverse mode spacing  $\Delta\nu_t$  as a measure of length

for a short cavity. From Equation 7.8 above, we obtain

$$l_{eff} = \frac{c^2}{2\pi^2 R(\Delta\nu_t)^2}. \quad (7.21)$$

A transverse mode spacing may be measured by scanning the cavity length while tuning the laser between *closely spaced* wavelengths  $\lambda_1$  and  $\lambda_2$ , so the transverse mode spacing on modes at  $\lambda_1$  can be calibrated against the spacing between the fundamental modes for  $\lambda_1$  and  $\lambda_2$ . A test cavity with mirror curvature  $R = 10\text{ cm}$  was measured via the usual technique to have  $l_{eff} = 11.16\text{ }\mu\text{m}$ , implying  $l_{phys} = 25\lambda/2 = 10.48\text{ }\mu\text{m}$  since the measurement wavelength was 838nm. For the same cavity a length measurement using the transverse mode technique gave  $l_{eff} = 11.06\text{ }\mu\text{m}$ , agreeing to better than a percent as long as  $\Delta\nu_t$  measures  $l_{eff}$ . More careful treatment of transverse mode spacing as affected by mirror coating dispersion is necessary if this measurement is to be adopted for very short cavity lengths.

A second candidate measurement technique does not rest on detailed mirror coating calculations but does require the ability to scan the cavity length over a free spectral range with excellent linearity. The simple idea is to calibrate the cavity length scan by observing the scan over a complete free spectral range of some single wavelength, i.e., over  $\Delta l = \lambda_1/2$ . Then by comparison it is possible to obtain the cavity length difference required between the *same* longitudinal modes for  $\lambda_1$  and a nearby  $\lambda_2$ . Here  $l_{eff,1} = n(\lambda_1/2)$ ,  $l_{eff,2} = n(\lambda_2/2)$ , and we measure  $l_{eff,1} - l_{eff,2}$  to allow determination of  $n$  and thus the overall cavity length. The scan linearity for our current cavity mounts and piezos does not permit a precise measurement via this technique, but it is in principle a promising alternative for the future.

## Chapter 8

# Outlook and Extensions for Feedback and Short Cavities

What is the next step for active feedback to the position of an atom in a cavity? A number of extensions and modifications suggest themselves for improvement of the present trapping/feedback scheme and thus realization of cooling and quantum effects discussed in previous chapters. In this chapter I conclude by briefly discussing several directions for active-feedback and short-cavity experiments – some more or less sensible, and some rather unrealistic but nevertheless quixotically appealing to me. Motivations, rough estimates, and limitations/challenges are discussed for each proposed direction of future work.

### 8.1 Cooling to the Axis by Breaking Cylindrical Symmetry

Feedback methods based solely on an atom interacting with the cavity  $TEM_{00}$  mode cannot in principle cool the atom to the cavity axis; because of the cylindrical symmetry of the mode, there is no mechanism for removing an atom's angular momentum. In order to remove angular momentum a symmetry-breaking force is required. Some direct measurement sensitivity to absolute angular position  $\theta$  is also helpful, but not strictly required. One can imagine a feedback scheme in which the angular momentum is estimated as in the atom-cavity microscope, the symmetry-breaking force is

applied to “kick” the atom, and the angular momentum is estimated again to determine if the kick was in the right direction. In this way an absolute knowledge of  $\theta(t)$  can be built up and the correct phase for application of the “side force” can be determined. Repeated “kicks” to reduce angular momentum, followed by cycles of re-circularizing via feedback to  $\dot{\rho}$ , could cool an atom to the cavity axis.

Simple candidates for a symmetry-breaking force include externally applied transverse electric or magnetic fields, light coupled into the cavity from the side, and light in transverse modes of the cavity itself. While gravity technically breaks the symmetry in the transverse plane, its effect on this problem is very weak. To see this, we compare the effective potential ( $\sim 2.5 \text{ mK}$  or  $2.6 \cdot 10^{-26} \text{ J}$ ) with the change in gravitational potential energy over the vertical extent of the interaction region. The latter quantity can be estimated as  $2w_0a_gm_{Cs} \approx 6 \cdot 10^{-29} \text{ J}$ . Thus gravity is negligible relative to the atom-field forces by more than a factor of 100 in our situation.

Light in transverse modes of the physics cavity is an appealing choice for its ability to be rapidly switched and the good prospects for incorporation into an existing experimental setup. Observation of atom transits through higher-order transverse modes has been proposed [107], though this work focused on mode symmetries technically unavailable due to birefringent splittings in actual high-finesse cavities. Here I present a few considerations for symmetry-breaking using light in the  $TEM_{01}$  mode of the physics cavity.

In considering the transverse mode as a symmetry breaker for force or for  $\theta$  sensing, important quantities are the potential and AC Stark shift due to this light. In a  $10.9 \mu\text{m}$  cavity with  $R=10 \text{ cm}$  mirror curvature, the transverse mode spacing is 65 GHz, so light in the transverse mode is quite far detuned from the cavity QED resonance. For one photon in the  $TEM_{01}$  mode (with the  $TEM_{00}$  tuned to the atomic resonance), the AC Stark shift is 47 kHz and the scattering rate is about four per second. To noticeably affect cavity QED dynamics, Stark shifts of at least several MHz are necessary. Clearly large photon numbers would have to be used, but these would still correspond to modest driving powers in absolute terms. The  $TEM_{01}$  transverse field profile is  $\frac{2\sqrt{2}}{w_0}ye^{-(y^2+z^2)/w_0^2}$ , so the field maximum is at  $y = w_0/\sqrt{2}$ .

This is definitely close enough to kick typical trapped atoms but clearly restricts how far an atom can be driven towards the axis before this particular side force becomes ineffective.

## 8.2 Axial Motion: Sensing and Cooling

Cooling of radial motion, even to the cavity axis, does little to directly address axial motion or absolute lifetime for trapped atoms in the cavity. Cooling axial motion, either via active feedback or otherwise, would lead to increased lifetimes for position servo schemes or broader quantum optics protocols. Observation of axial motion is furthermore of interest because the smaller length scale ( $\lambda/4$  vs.  $w_0$ ) and correspondingly higher vibrational frequency make motion in this dimension a good candidate for observing effects associated with the quantized center-of-mass motion of the atom [108, 109, 110, 111, 23, 112].

Cooling radial motion does little to affect axial heating processes, since the only process mixing the dimensions is atomic spontaneous emission, the rate of which is very small compared to axial dynamics. Certainly the depth of the axial potential and the momentum diffusion rates scale with the value of  $\rho$  since  $g(\vec{r}) = g(\rho, x)$ , but the problem is still separable and thus cooling in the radial direction has little opportunity to extract energy from the axial motion.

The present feedback algorithm as presented and simulated in Chapter 5 can certainly be altered in the experiment to prevent unnecessary *heating* of axial motion due to radial feedback. The feedback simulated in Chapter 5 involves instantaneous switching of the drive strength (cavity input intensity), which is timed correctly with respect to radial motion but occurs at generally arbitrary times with respect to axial oscillation. One might expect this arbitrary switching between potentials to in general accelerate an atom's escape from the trap in the axial direction. A simple alternative experimentally (though computationally intensive in simulations) is to ramp the cavity drive level continuously at a speed which is roughly instantaneous for the radial motion but adiabatic with respect to axial motion. The factor of  $\sim 10^2$  separation

between radial and axial timescales makes this a feasible strategy to pursue.

For observation of axial motion, one avenue for increased signal-to-noise is implementation of full measurement [47] of field amplitude and phase, as mentioned already in Chapter 4. This would provide greater sensitivity for atomic motion near the field antinode where axial motion typically occurs.

Simulations of feedback to axial motion [113] have indicated that cooling nearly to the vibrational ground state is possible in some parameter regimes using the same basic intensity-modulation method we employ in the radial direction. Theoretical treatments of this case have considered diverse aspects of quantized atomic motion and the transition from classical to quantum servo operation [114, 115, 116]. To probe these questions experimentally, one possibility is to deliberately excite axial motion with a rapid momentum kick and then to attempt cooling of this axial excitation. To displace a trapped atom’s motion from the field antinode, and to do so quickly relative to the MHz timescale of atomic motion, is not a technically trivial task, but possible avenues might include light forces from other longitudinal modes or (less likely) rapid cavity mirror displacement.

The simulations of [113] tend to operate in a regime where the cavity and probe are far detuned from atomic resonance, being as much as 4GHz to the red of the atomic transition. Moving to these far-detuned regimes involves decreased trap depth for an atom due to the cavity QED probe. Other non-active cooling mechanisms for axial motion have also been proposed [117, 118] but involve weak-driving conditions which also reduce overall trap depth. Pursuit of these conditions is limited by the need to efficiently trap atoms of our typical initial energies (dominated by fall velocity). Alternatively, the limitation arises because we rely on the same optical field – the cavity QED probe – for both sensing and trapping of the atomic motion. Getting away from these limitations is one motivation for adding a FORT to trap an atom independently of the cavity QED field. Long FORT lifetime with simultaneous high signal-to-noise cavity QED position sensing is a goal currently under pursuit in another experiment in our group [52, 76]. Introduction of the FORT also allows novel cooling schemes using the FORT and cavity QED beams simultaneously [96].

### 8.3 Far-Flung Applications of Very Short Cavities

The strong coupling enabled by very small mode volumes in optical cavity QED has numerous applications to protocols throughout the field of quantum information science; for a far from exhaustive set of examples and perspectives, see [119, 120, 121, 122, 59, 123, 124, 125, 60]. Proposals for observation of quantum-optical effects such as non-classical photon statistics in very short cavities are found in [19]. Here I mention instead some other potential applications of very short cavities.

Very high-finesse cavities provide sensitivity for detecting numerous intracavity processes, with detection enhanced over single-pass spectroscopy by roughly  $2F/\pi$ . One example is the high sensitivity for detecting birefringent phase shifts, either on the mirror surfaces or due to some more exotic physical effect (see, e.g., [105]). In this particular case the use of a very short cavity further serves to move the “signal” splitting into a frequency regime where laser locks and other resolution-broadening noise sources in the experiment do not obscure the effect. Another accidentally discovered application, as discussed by Joseph Buck in his thesis [76], is the detection (and possible deliberate excitation/cooling) of  $k_B T$  thermal vibrations of the glass mirror substrates themselves. These vibrations can be detected on the amplitude of light transmitted through a cavity; the sensitivity improves as a cavity becomes shorter and  $\kappa$  increases, since the vibrational mode frequencies for the small substrates begin around 1GHz.

Another intriguing application of a short cavity is to the study of atom interactions with a nearby solid or surface. We may imagine, for example, a cavity of length  $3\lambda/2$  in which the two field antinodes on the sides are differentiated from the central antinode by their proximity to the mirror surfaces. Atomic interactions with the mirror surfaces would produce different signals for atoms occupying the central or side antinodes. This scenario is not immediately realistic for the study of typical van der Waals forces, since an atom would naturally interact with a field antinode  $\sim 200$  nm from the mirror surface while van der Waals distance scales are much smaller, on the order of  $\sim 1$  nm or less. However, one might imagine a similar short cavity of just

a few antinodes distinguished from one another by proximity to an auxiliary solid or surface which is being studied.

A final pipe dream involves the realization of a quantum chaos experiment, in the spirit of the delta-kicked rotor, in the standing-wave dimension of a short cavity [126]. Motion in this dimension can, as we have seen, be brought to a significantly quantized regime. With good sensing of axial motion a kicked-rotor type experiment could be envisioned with the “kick” provided by rapid displacement of the mirror surfaces, as mentioned above. Such rapid displacement presents technical challenges, but a more basic limit on the speed of a “kick” is given by  $\kappa$  as it gives the rate for adjustment of the intracavity field. A very short cavity is thus suitable for this scenario as it provides large  $\kappa$  for a given finesse.

## 8.4 Comment on Quantum State Estimation and Control

The work presented here on detection and control of a single atom’s position in real time represents one aspect of an emerging experimental field of quantum state control. Both theoretical and experimental work in several different contexts are beginning to address the issue of practical, continuous control of a simple quantum state. These investigations aim variously towards continuous quantum error correction protocols [127], studies of quantum measurement and information-disturbance tradeoffs [98, 61, 62, 128], and realization of novel system evolutions and designer quantum states through the application of real-time feedback [63, 129].

Motivations for this line of inquiry are diverse, and range from curiosity about the quantum-classical transition to the lure of massively parallel quantum computation (“qubit-inside” technology development). I know that I, like (I believe) most other physicists in this field, am motivated primarily by the desire to get a better idea of the hazy quantum-classical transition region, obscured for much of the last century in both philosophy and computational rules of projective measurement. These questions

sit at the foundations of quantum mechanics, whether or not their answers result in eventual quantum PC's (or quantum subroutines). However, I conclude with an extremely technology-oriented motive for the study of state control at the frontier of the quantum regime, and one which I rarely hear mentioned at least in the last few years. This is the ongoing miniaturization of IC components for (classical) computation, with a feature size of  $\lesssim 0.1 \mu\text{m}$  today and a historical trend of an order of magnitude decrease in twenty years [130]. Looking at trends along these lines it is clear that a very finite time span will see us at the threshold of computing with – and therefore controlling – individual quantum systems, and deep in the hazy borderland of quantum measurement whether we will or no. Let us, then, at least begin to map out the territory ahead.

## Appendix A

# Computer-Experiment Interfacing in the Active Feedback Experiment

The active-feedback experiment incorporates several computers and auxiliary boards for timing control of the overall experiment, data acquisition, and feedback implementation. This Appendix describes the hardware and software used to accomplish these tasks as of the end of April, 2003. The summary presented here will be of interest chiefly to those involved in future versions of the same experiment. Computers in the lab are referred to by name. Several specific programs or software-setting files are also named; these are archived separately on hard drive and CD-ROM within our research group.

### A.1 Overall Experiment Timing

The timing of the overall experiment, including the MOT cycle and data acquisition trigger, is described in Section 6.1.4. This master timing is set by a Labview program outputting timing signals from a National Instruments AT-AO-10 analog output board. The board takes a 1-kHz external update trigger which defines its clock speed. Then it updates outputs on up to ten channels every clock cycle, as instructed by the Labview routine. The computer Qolinux1 (at least seven years old right now) is more or less dedicated to running this timing program. The current Labview routine is `Transits_Oct24_2002.vi`, which lives in the Qolinux folder `C:\User\Kevin\`.

The channel 0 output of this program controls the upper MOT gradient field. It

goes to the external voltage control of a Kepco ATE6-10M power supply which drives the upper MOT main coils.

The channel 1 output controls the trapping light intensity for both MOT's. It goes to the video input of an Isomet 233A acousto-optic modulator driver. Thus it controls the RF power going to the single-pass AOM in the trapping beam path.

The channel 2 output gives a trigger signal for a camera; this channel is irrelevant in the actual experiment and is only used for MOT and cooling diagnostics.

The channel 3 output gives a trigger signal for the framegrabber, a Data Translation board which acquires an image from a camera and transfers it to the computer Cqed. This channel is only used for MOT and cooling diagnostics.

The channel 4 output controls the lower MOT gradient field. It goes to an op-amp (OP27) configured for a gain of 2, and thence to the voltage control of a Kepco ATE15-50M power supply which drives the lower MOT main coils.

The channel 5 output controls the MOT trapping light detuning, allowing it to be changed during sub-Doppler cooling. This output goes to the tuning voltage ( $V_T$ ) input of an Isomet D323B acousto-optic deflector driver. Thus it controls the frequency of the RF signal going to the double-pass AOM in the trapping beam path.

The channel 6 output sends a trigger to the Gage board for data acquisition.

The channel 7 output is used only for locking the physics cavity to the probe beam itself. This channel goes to a Stanford (SR560) preamplifier blanking input, and can be used to blank the physics cavity lock during an atom transit.

### A.1.1 Framegrabber Operation

The framegrabber board mentioned above is a Data Translation DT3152 board run with modified Data Translation Open Layers software on the computer Cqed. The framegrabber board accepts an external trigger. The program we use to acquire images is acq11hst.exe, which allows acquisition of one frame with or without triggering, or of either 60 or 180 consecutive frames on triggers. The relevant software development package is a out-of-date version of DT Open Layers; the directory D:\Dtols\ on

Cqed contains the code for acq11hst and the auxiliary libraries it requires.

## A.2 Data Acquisition

The cavity transmission data is sent to the computer in the form of a video output signal from an Agilent spectrum analyzer, just as described in Chapter 3. This signal goes to a Gage data acquisition (a/d) board (CompuScope 1450) on the computer Bigg. Data is displayed on the screen and saved using the GageScope 3.0 software package. Data traces are saved as GageScope signal files (*.sig* file extension). The current program for acquiring this data is the software's default data acquisition program; it does *not* perform a conversion from spectrum analyzer output voltage to photon number. This conversion and calibration is summarized in MathCAD routines on the computer Cqed, in the directory C:\Winmcad\. The relevant routines are PhotDBM.mcd, Beat.mcd, and Beatlin.mcd.

A second quantity,  $\dot{\rho}_{est}$ , must be saved as well since it forms the basis for feedback figures of merit (Chapter 5). This signal is generated on the FPGA board, as described below.

## A.3 Triggering and Feedback

The triggering and feedback, unlike the master timing of the experiment, are controlled by the FPGA board (GVA-290a) which is programmed from the computer Bigg. The FPGA board itself has four analog input channels, so the spectrum analyzer video out signal (already with 100kHz bandwidth) is sent directly to the board. Four on-board output channels can be used. The relevant output for triggering and feedback is a control voltage sent to an AOM in the probe path for switching of the probe intensity. The feedback algorithm also generates  $\dot{\rho}_{est}(t)$  for each trapped atom; a record of this quantity must be saved as it is the basis for our feedback figure of merit as presented in Chapter 5. The FPGA program is largely the creation of Kevin Birnbaum, and is still very much an evolving entity. Here I give a high-level tour of

its functions.

The board digitizes the input transmission signal at a depth of 12 bits. The digitized signal is compared to a programmed reference level for initial triggering to trap an atom. The transmission signal, currently binned into only 256 discrete values, is sent to a lookup table which converts transmission to  $\rho_{est}$  for an atom trapped with given detunings and drive strength. The  $\rho_{est}$  record is used in the slope-estimation FIR filter of Chapter 5 to generate  $\dot{\rho}_{est}$ . This quantity goes to an output of the FPGA board so it can be sent to the Gage board and saved.

Switching conditions, i.e., limit-crossings of  $\dot{\rho}_{est}$ , are determined by comparing  $\dot{\rho}_{est}$  to programmed reference values. Times of these limit-crossings are noted and the delayed-feedback algorithm of Chapter 5 is implemented. Switching from one drive level to another involves: (1) switching the output control voltage going to the AOM and (2) switching lookup tables for the transmission to  $\rho_{est}$  conversion on the FPGA board itself.

## Bibliography

- [1] E. M. Purcell. Spontaneous emission probabilities at radio frequencies. *Phys. Rev.*, 69:681, 1946.
- [2] K. H. Drexhage. *Progress in Optics*, volume XII, pages 163–232. Elsevier, New York, 1974. Ed. E. Wolf.
- [3] H. B. G. Casimir and D. Polder. The influence of retardation on the London-van der Waals forces. *Phys. Rev.*, 73:360, 1948.
- [4] P. Goy, J. M. Raimond, M. Gross, and S. Haroche. Observation of cavity-enhanced single-atom spontaneous emission. *Phys. Rev. Lett.*, 50:1903, 1983.
- [5] L. S. Brown and G. Gabrielse. Geonium theory – physics of a single electron or ion in a Penning trap. *Rev. Mod. Phys.*, 58:233, 1986.
- [6] D. J. Heinzen and M. S. Feld. Vacuum radiative level shift and spontaneous-emission linewidth of an atom in an optical-resonator. *Phys. Rev. Lett.*, 59:2623, 1987.
- [7] Y. Zhu and A. Lezama, T. W. Mossberg, and M. Lewenstein. Vacuum-field dressed-state pumping. *Phys. Rev. Lett.*, 61:1946, 1988.
- [8] C. I. Sukenik, M. G. Boshier, D. Cho, V. Sandoghdar, and E. A. Hinds. Measurement of the Casimir-Polder force. *Phys. Rev. Lett.*, 70:560, 1995.
- [9] S. K. Lamoreaux. Demonstration of the Casimir force in the 0.6 to 6  $\mu\text{m}$  range. *Phys. Rev. Lett.*, 78:5, 1997.

- [10] U. Mohideen and A. Roy. Precision measurement of the Casimir force from 0.1 to 0.9  $\mu\text{m}$ . *Phys. Rev. Lett.*, 81:4549, 1998.
- [11] G. Gabrielse and H. Dehmelt. Observation of inhibited spontaneous emission. *Phys. Rev. Lett.*, 55:67, 1985.
- [12] R. Hulet, E. Hilfer, and D. Kleppner. Inhibited spontaneous emission by a Rydberg atom. *Phys. Rev. Lett.*, 55:2137, 1985.
- [13] F. De Martini, G. Innocenti, G. R. Jacobovitz, and P. Mataloni. Anomalous spontaneous emission time in a microscopic optical cavity. *Phys. Rev. Lett.*, 59:2955, 1987.
- [14] D. Kleppner and S. Haroche. Cavity quantum electrodynamics. *Physics Today*, 42:24, 1989.
- [15] D. Meschede. Radiating atoms in confined space – from spontaneous emission to micromasers. *Phys. Rep.*, 211:201, 1992.
- [16] S. Peil and G. Gabrielse. Observing the quantum limit of an electron cyclotron: QND measurements of quantum jumps between Fock states. *Phys. Rev. Lett.*, 83:1287, 1999.
- [17] E. A. Hinds. Cavity quantum electrodynamics. *Adv. Atom. Mol. Opt.*, 28:237, 1990.
- [18] C. J. Hood, H. J. Kimble, and J. Ye. Characterization of high-finesse mirrors: Loss, phase shifts, and mode structure in an optical cavity. *Phys. Rev. A*, 64:033804, 2001. Available as quant-ph/0101103.
- [19] C. J. Hood. *Real-Time Measurement and Trapping of Single Atoms by Single Photons*. PhD thesis, California Institute of Technology, 2000.
- [20] C. J. Hood, M. S. Chapman, T. W. Lynn, and H. J. Kimble. Real-time cavity QED with single atoms. *Phys. Rev. Lett.*, 80:4157, 1998.

- [21] S. Haroche, M. Brune, and J. M. Raimond. Trapping atoms by the vacuum field in a cavity. *Europhys. Lett.*, 14:19, 1991.
- [22] B. Englert, J. Schwinger, A. O. Barut, and M. O. Scully. Reflecting slow atoms from a micromaser field. *Europhys. Lett.*, 14:25, 1991.
- [23] M. O. Scully, G. M. Meyer, and H. Walther. Induced emission due to the quantized motion of ultracold atoms passing through a micromaser cavity. *Phys. Rev. Lett.*, 76:4144, 1996.
- [24] A. C. Doherty, A. S. Parkins, S. M. Tan, and D. F. Walls. Motion of a two-level atom in an optical cavity. *Phys. Rev. A*, 56:833, 1997.
- [25] C. J. Hood, T. W. Lynn, A. Doherty, A. S. Parkins, and H. J. Kimble. The atom-cavity microscope: single atoms bound in orbit by single photons. *Science*, 287:1447, 2000.
- [26] A. C. Doherty, T. W. Lynn, C. J. Hood, and H. J. Kimble. Trapping of single atoms with single photons in cavity QED. *Phys. Rev. A*, 63:013401, 2001. Available as quant-ph/0006015.
- [27] Q. A. Turchette. *Quantum optics with single atoms and single photons*. PhD thesis, California Institute of Technology, 1997.
- [28] E. T. Jaynes and F. W. Cummings. Comparison of quantum and semiclassical radiation theories with application to beam maser. *P. IEEE*, 51:89, 1963.
- [29] S. Haroche. *in Fundamental Systems in Quantum Optics, Les Houches Session LIII, 1990*. Elsevier, Amsterdam, 1992. Eds. J. Dalibard, J.-M. Raimond, and J. Zinn-Justin. For a textbook development of cavity QED basics.
- [30] H. J. Kimble. *in Cavity Quantum Electrodynamics*. Academic Press, San Diego, 1994. Ed. P. Berman.
- [31] H. J. Kimble. Strong interactions of single atoms and photons in cavity QED. *Phys. Scripta*, T76:127, 1998.

- [32] C. Cohen-Tannoudji, J. Dupont-Roc, and G. Grynberg. *Atom-Photon Interactions*. Wiley, New York, 1992.
- [33] H. J. Carmichael. *Statistical Methods in Quantum Optics 1*. Texts and Monographs in Physics. Springer-Verlag, Heidelberg, 1st edition, 1999.
- [34] S. M. Tan. A computational toolbox for quantum and atom optics. *J. Opt. B: Quant. Semiclass. Opt.*, 1:424, 1999.
- [35] L. A. Lugiato. Theory of optical bistability. *Progress in Optics*, 21:69, 1984. A review of the field.
- [36] D. E. Grant and H. J. Kimble. Optical bistability for 2-level atoms in a standing-wave cavity. *Opt. Lett.*, 7:353, 1982.
- [37] K. G. Weyer, H. Wiedenmann, M. Rateike, W. R. M. Gillivray, P. Meystre, and H. Walther. Observation of absorptive optical bistability in a Fabry-Perot cavity containing multiple atomic-beams. *Opt. Commun.*, 37:426, 1981.
- [38] G. Rempe, R. J. Thompson, R. J. Brecha, W. D. Lee, and H. J. Kimble. Optical bistability and photon statistics in cavity quantum electrodynamics. *Phys. Rev. Lett.*, 67:1727, 1991.
- [39] S. L. Mielke, G. T. Foster, and L. A. Orozco. Nonclassical intensity correlations in cavity QED. *Phys. Rev. Lett.*, 80:3948, 1998.
- [40] G. T. Foster, S. L. Mielke, and L. A. Orozco. Intensity correlations in cavity QED. *Phys. Rev. A*, 61:053821, 2000.
- [41] G. T. Foster, L. A. Orozco, H. M. Castro-Beltran, and H. J. Carmichael. Quantum state reduction and conditional time evolution of wave-particle correlations in cavity QED. *Phys. Rev. Lett.*, 85:3149, 2000.
- [42] Q. A. Turchette, C. J. Hood, W. Lange, H. Mabuchi, and H. J. Kimble. Measurement of conditional phase shifts for quantum logic. *Phys. Rev. Lett.*, 75:4710, 1995.

- [43] Q. A. Turchette, N. P. Georgiades, C. J. Hood, H. J. Kimble, and A. S. Parkins. Squeezed excitation in cavity QED: Experiment and theory. *Phys. Rev. A*, 58:4056, 1998.
- [44] J. J. Sanchez-Mondragon, N. B. Narozhny, and J. H. Eberly. Spontaneous vacuum line splitting in a cavity. *J. Opt. Soc. Am. B*, 1:518, 1984.
- [45] R. J. Thompson, G. Rempe, and H. J. Kimble. Observation of normal-mode splitting for an atom in an optical cavity. *Phys. Rev. Lett.*, 68:1132, 1992.
- [46] H. Mabuchi, Q. A. Turchette, M. S. Chapman, and H. J. Kimble. Real-time detection of individual atoms falling through a high-finesse optical cavity. *Opt. Lett.*, 21:1393, 1996.
- [47] H. Mabuchi, J. Ye, and H. J. Kimble. Full observation of single-atom dynamics in cavity QED. *Applied Phys. B*, 68:1095, 1999.
- [48] P. Munstermann, T. Fischer, P. Maunz, P. W. H. Pinkse, and G. Rempe. Dynamics of single-atom motion observed in a high-finesse cavity. *Phys. Rev. Lett.*, 82:3791, 1999.
- [49] Y. Shimizu, N. Shiokawa, N. Yamamoto, M. Kozuma, and T. Kuga. Control of light pulse propagation with only a few cold atoms in a high-finesse microcavity. *Phys. Rev. Lett.*, 89:233001, 2002.
- [50] P. W. H. Pinkse, T. Fischer, P. Maunz, and G. Rempe. Trapping an atom with single photons. *Nature*, 404:365, 2000.
- [51] J. Ye, D. W. Vernooy, and H. J. Kimble. Trapping of single atoms in cavity QED. *Phys. Rev. Lett.*, 83:4987, 1999.
- [52] J. McKeever, J. R. Buck, A. D. Boozer, A. Kuzmich, H.-C. Naegerl, D. M. Stamper-Kurn, and H. J. Kimble. State-insensitive cooling and trapping of single atoms in an optical cavity. *Phys. Rev. Lett.*, to appear in 2003. Available as quant-ph/0211013.

- [53] H. Mabuchi, M. Armen, B. Lev, M. Loncar, J. Vuckovic, H. J. Kimble, J. Preskill, M. Roukes, and A. Scherer. Quantum networks based on cavity QED. *Q. Inf. and Comp.*, 1(Special Issue on Implementation of Quantum Computation):7, 2001.
- [54] W. Lange and H. Walther. private communication, 2003.
- [55] A. B. Mundt, A. Kreuter, C. Becher, D. Leibfried, J. Eschner, F. Schmidt-Kaler, and R. Blatt. Coupling a single atomic quantum bit to a high finesse optical cavity. *Phys. Rev. Lett.*, 89:103001, 2002.
- [56] M. S. Chapman et al. private communication, 2003.
- [57] S. Kuhr, W. Alt, D. Schrader, M. Muller, V. Gomer, D. Meschede, et al. Deterministic delivery of a single atom. *Science*, 293:278, 2001.
- [58] A. Soklakov and R. Schack. Information dynamics in cavity QED. quant-ph/0210024, 2002.
- [59] M. S. Feld and K. W. An. The single-atom laser. *Sci. Am.*, 279:56, 1998.
- [60] L.-M. Duan and H. J. Kimble. Efficient engineering of multi-atom entanglement through single-photon detections. quant-ph/0301164, 2003.
- [61] H. Mabuchi and H. M. Wiseman. Retroactive quantum jumps in a strongly coupled atom-field system. *Phys. Rev. Lett.*, 81:4620, 1998.
- [62] P. Warszawski, H. M. Wiseman, and H. Mabuchi. Quantum trajectories for realistic detection. *Phys. Rev. A*, 65:023802, 2002.
- [63] W. P. Smith, J. E. Reiner, L. A. Orozco, S. Kuhr, and H. M. Wiseman. Capture and release of a conditional state of a cavity QED system by quantum feedback. *Phys. Rev. Lett.*, 89:133601, 2002.
- [64] E. L. Raab, M. Prentiss, A. Cable, S. Chu, and D. E. Pritchard. Trapping of neutral Na atoms with radiation pressure. *Phys. Rev. Lett.*, 59:2631, 1987.

- [65] D. E. Pritchard, E. L. Raab, V. Bagnato, C. E. Wieman, and R. N. Watts. Light traps using spontaneous forces. *Phys. Rev. Lett.*, 57:310, 1986.
- [66] P. D. Lett, R. N. Watts, C. I. Westbrook, W. D. Phillips, P. L. Gould, and H. J. Metcalf. Observation of atoms laser cooled below the Doppler limit. *Phys. Rev. Lett.*, 61:169, 1988.
- [67] J. Dalibard and C. Cohen-Tannoudji. Laser cooling below the doppler limit by polarization gradients: simple theoretical models. *J. Opt. Soc. Am. B*, 6:2023, 1989.
- [68] P. Ungar, D. Weiss, E. Riis, and S. Chu. Optical molasses and multilevel atoms: theory. *J. Opt. Soc. Am. B*, 6:2058, 1989.
- [69] A. M. Steane, M. Chowdhury, and C. J. Foot. Radiation force in a magneto-optical trap. *J. Opt. Soc. Am. B*, 9:2142, 1992.
- [70] D. Sesko, T. Walker, and C. Wieman. Behavior of neutral atoms in a spontaneous force trap. *J. Opt. Soc. Am. B*, 8:946, 1991.
- [71] Y. Castin, H. Wallis, and J. Dalibard. Limit of Doppler cooling. *J. Opt. Soc. Am. B*, 6:2046, 1989.
- [72] X. Y. Xu, T. H. Loftus, M. J. Smith, J. L. Hall, A. Gallagher, and J. Ye. Dynamics in a two-level atom magneto-optical trap. *Phys. Rev. A*, 66:011401, 2002.
- [73] C. E. Tanner, A. E. Livingston, R. J. Rafac, K. W. Kukla, H. G. Berry, and C. A. Kurtz. Precision lifetime measurements using laser excitation of a fast atomic-beam. *Nucl. Instrum. Meth. B*, 99:117, 1995.
- [74] D. A. Steck. Cesium D line data. Available at <http://steck.us/alkalidata/>, 2002.
- [75] W. Demtroder. *Laser Spectroscopy*. Springer-Verlag, New York, 2nd edition edition, 1996.

- [76] J. R. Buck. *Cavity-QED in Microsphere and Fabry-Perot Cavities*. PhD thesis, California Institute of Technology, 2003.
- [77] G. Bjorklund. Frequency-modulated spectroscopy – new method for measuring weak absorptions and dispersions. *Opt. Lett.*, 5:15, 1980.
- [78] J. L. Hall, L. Hollberg, T. Baer, and H. G. Robinson. Optical heterodyne saturation spectroscopy. *Appl. Phys. Lett.*, 39:680, 1981.
- [79] L. Wu, M. Xiao, and H. J. Kimble. Squeezed states of light from an OPO. *J. Opt. Soc. Am. B*, 4:1465, 1987.
- [80] Blake Peterson. Spectrum analysis. Application Note 150, Hewlett-Packard Company, 1212 Valley House Dr., Rohnert Park, CA, USA, November 1989.
- [81] The Mathworks Inc. Matlab Signal Processing Toolbox User’s Guide, December 1996. Version 4 (for Matlab 5).
- [82] H. Mabuchi. Standard quantum limits for broadband position measurement. *Phys. Rev. A*, 58:123, 1998.
- [83] A. C. Doherty. *Motion, Measurement and Control in an Open Quantum System*. PhD thesis, The University of Auckland, 1999.
- [84] C. Cohen-Tannoudji. in *Fundamental Systems in Quantum Optics, Les Houches Session LIII, 1990*. Elsevier, Amsterdam, 1992. Eds. J. Dalibard, J.-M. Raymond, and J. Zinn-Justin.
- [85] P. Horak, G. Hechenblaikner, K. M. Gheri, H. Stecher, and H. Ritsch. Cavity-induced cooling in the strong coupling regime. *Phys. Rev. Lett.*, 79:4974, 1997.
- [86] V. Vuletic and S. Chu. Laser cooling of atoms, ions, or molecules by coherent scattering. *Phys. Rev. Lett.*, 84:3787, 2000.
- [87] T. Fischer, P. Maunz, P. W. H. Pinkse, T. Puppe, and G. Rempe. Feedback on the motion of a single atom in an optical cavity. *Phys. Rev. Lett.*, 88:163002, 2002.

- [88] A. J. Scott and G. J. Milburn. Quantum nonlinear dynamics of continuously measured systems. *Phys. Rev. A*, 63:042101, 2001.
- [89] G. J. Milburn. Classical and quantum conditional statistical dynamics. *Quant. Semiclass. Opt.*, 8:269, 1996.
- [90] A. C. Doherty, S. M. Tan, A. S. Parkins, and D. F. Walls. State determination in continuous measurement. *Phys. Rev. A*, 60:2380, 1999.
- [91] R. E. Kalman. A new approach to linear filtering and prediction problems. *Transactions of the ASME-Journal of Basic Engineering*, 82(Series D):35, 1960.
- [92] R. Legere. Unpublished models of tracking single-atom motion in cavity QED with Kalman filters., 2000.
- [93] G. Welch and G. Bishop. The Kalman filter. Available at <http://www.cs.unc.edu/~welch/kalman/>, 2003. A site containing tutorials, advanced material, and additional references on Kalman filters.
- [94] Lee Barford, Eric Mandres, Gautam Biswas, Pieter Mosterman, Vishnu Ram, and Joel Barnett. Derivative estimation for diagnosis. Technical Report HPL-1999-18, Integrated Solutions Laboratory, HP Laboratories, Palo Alto, CA, February 1999. Available at [www.hpl.hp.com/techreports/1999/HPL-1999-18.html](http://www.hpl.hp.com/techreports/1999/HPL-1999-18.html).
- [95] O. Vainio, M. Renfors, and T. Saramaki. Recursive implementation of FIR differentiators with optimum noise attenuation. *IEEE Trans. inst. Meas.*, 46:5, 1997.
- [96] S. J. van Enk, J. McKeever, H. J. Kimble, and J. Ye. Cooling of a single atom in an optical trap inside a resonator. *Phys. Rev. A*, 64:013407, 2001. Available and quant-ph/0005133.
- [97] J. Stockton, M. Armen, and H. Mabuchi. Programmable logic devices in experimental quantum optics. *J. Opt. Soc. Am. B*, 19:3019, 2002.

- [98] J. Gambetta and H. M. Wiseman. State and dynamical parameter estimation for open quantum systems. *Phys. Rev. A*, 64:042105, 2001.
- [99] H. J. Kimble, C. J. Hood, T. W. Lynn, H. Mabuchi, D. W. Vernooy, and J. Ye. *in Laser Spectroscopy: XIV International Conference*. World Scientific, Singapore, 1999. Eds. Rainer Blatt et al.
- [100] D. W. Vernooy. *Cold Atoms in Cavity QED for Quantum Information Processing*. PhD thesis, California Institute of Technology, 2000.
- [101] T. Bergeman, G. Erez, and H. J. Metcalf. Magnetostatic trapping fields for neutral atoms. *Phys. Rev. A*, 35:1535, 1987. A good tutorial reference on magnetic field configurations.
- [102] R. W. P. Drever, J. L. Hall, F. V. Kowalski, J. Hough, G. M. Ford, A. J. Munley, and H. Ward. Laser phase and frequency stabilization using an optical-resonator. *Appl. Phys. B*, 31:145, 1983.
- [103] G. C. Bjorklund, M. D. Levenson, W. Lenth, and C. Ortiz. Frequency-modulation (FM) spectroscopy – theory of lineshapes and signal-to-noise analysis. *Appl. Phys. B*, 32:145, 1983.
- [104] R. Panaguia (Caltech physics machine shop). private communication, 2002.
- [105] J. Ye and T. W. Lynn. Applications of optical cavities in modern atomic, molecular, and optical physics. *Adv. Atom. Mol. Opt. Phys.*, to appear in 2003.
- [106] A. E. Siegman. *Lasers*. University Science Books, Mill Valley, CA, 1986.
- [107] P. Horak, H. Ritsch, T. Fischer, P. Maunz, T. Puppe, P. W. H. Pinkse, and G. Rempe. Optical kaleidoscope using a single atom. *Phys. Rev. Lett.*, 88:043601, 2002.
- [108] P. Meystre, E. Schumacher, and S. Stenholm. Atomic-beam deflection in a quantum-field. *Opt. Comm.*, 73:443, 1989.

- [109] W. Ren and H. J. Carmichael. Spontaneous emission in a standing-wave cavity: quantum-mechanical center-of-mass motion. *Phys. Rev. A*, 51:752, 1995.
- [110] A. M. Herkommer, H. J. Carmichael, and W. P. Schleich. Localization of an atom by homodyne measurement. *Quant. Semiclass. Opt.*, 8:189, 1996.
- [111] A. C. Doherty, A. S. Parkins, S. M. Tan, and D. F. Walls. Motional states of atoms in cavity QED. *Phys. Rev. A*, 57:4804, 1998.
- [112] D. W. Vernooy and H. J. Kimble. Well-dressed states for wave-packet dynamics in cavity QED. *Phys. Rev. A*, 56:4287, 1997.
- [113] D. Steck and S. Habib. private communication, 2003.
- [114] T. Bhattacharya, S. Habib, and K. Jacobs. Continuous quantum measurement and the emergence of classical chaos. *Phys. Rev. Lett.*, 85:4852, 2000.
- [115] T. Bhattacharya, S. Habib, and K. Jacobs. Continuous quantum measurement and the quantum to classical transition. quant-ph/0211036, 2002.
- [116] A. C. Doherty, S. Habib, K. Jacobs, H. Mabuchi, and S. M. Tan. Quantum feedback control and classical control theory. *Phys. Rev. A*, 62:012105, 2000.
- [117] P. Domokos, P. Horak, and H. Ritsch. Semiclassical theory of cavity-assisted atom cooling. *J. Phys. B – At. Mol. Opt. Phys.*, 34:187, 2001.
- [118] M. Gangl and H. Ritsch. Cavity-mediated dark-state cooling without spontaneous emission. *Phys. Rev. A*, 64:063414, 2001.
- [119] H. J. Briegel, J. I. Cirac, W. Dur, S. J. van Enk, H. J. Kimble, H. Mabuchi, and P. Zoller. Physical implementations for quantum communication in quantum networks. *Quant. Comp. and Quant. Comm. (Lecture Notes in Computer Science)*, 1509:373, 1999.
- [120] T. Pellizzari, S. Gardiner, I. Cirac, and P. Zoller. Decoherence, continuous observation, and quantum computing: a cavity QED model. *Phys. Rev. Lett.*, 75:3788, 1995.

- [121] J. I. Cirac, P. Zoller, H. J. Kimble, and H. Mabuchi. Quantum state transfer and entanglement distribution among distant nodes in a quantum network. *Phys. Rev. Lett.*, 78:3221, 1997.
- [122] S. J. van Enk, J. I. Cirac, and P. Zoller. Photonic channels for quantum communication. *Science*, 279:205, 1998.
- [123] H. Mabuchi and A. C. Doherty. Cavity quantum electrodynamics: coherence in context. *Science*, 298:1372, 2002.
- [124] A. S. Parkins and H. J. Kimble. Quantum state transfer between motion and light. *J. Opt. B – Quant. Semiclass. Opt.*, 1:496, 1999.
- [125] S. Rebic, A. S. Parkins, and S. M. Tan. Photon statistics of a single-atom intracavity system involving electromagnetically induced transparency. *Phys. Rev. A*, 65:063804, 2002.
- [126] T. Bhattacharya, S. Habib, K. Jacobs, and K. Shizume. The delta-function-kicked rotor: momentum diffusion and the quantum-classical boundary. *Phys. Rev. A*, 65(032115), 2002.
- [127] C. Ahn, A. C. Doherty, and A. J. Landahl. Continuous quantum error correction via quantum feedback control. *Phys. Rev. A*, 65:042301, 2002.
- [128] C. A. Fuchs. Information gain vs. state disturbance in quantum theory. *PhysComp96*, 1996. Available as quant-ph/9611010.
- [129] J. Stockton, J. M. Geremia, and H. Mabuchi. private communication, 2002.
- [130] Gordon Moore. No exponential is forever... but we can delay forever. [ftp://download.intel.com/research/silicon/Gordon\\_Moore\\_ISSCC\\_021003.pdf](ftp://download.intel.com/research/silicon/Gordon_Moore_ISSCC_021003.pdf), February 2003. A presentation given at the International Solid State Circuits Conference (ISSCC).